Development of Cold Spray Technology for Copper Coating of Carbon Steel Used Fuel Container Prototypes for CANDU Fuel

NWMO TR-2015-29 **November 2015**

Phuong Vo[1], Dominique Poirier[1], Jean-Gabriel Legoux[1], Peter G. Keech[2], David Doyle[2], Pellumb Jakupi[3] and Eric Irissou[1]

[1]National Research Council Canada
[2]NWMO
[3]Western University

nwmo
NUCLEAR WASTE MANAGEMENT ORGANIZATION
SOCIÉTÉ DE GESTION DES DÉCHETS NUCLÉAIRES

Nuclear Waste Management Organization
22 St. Clair Avenue East, 6th Floor
Toronto, Ontario
M4T 2S3
Canada

Tel: 416-934-9814
Web: www.nwmo.ca

Development of Cold Spray Technology for Copper Coating of Carbon Steel Used Fuel Container Prototypes for CANDU Fuel

NWMO TR-2015-29

November 2015

Phuong Vo[1], Dominique Poirier[1], Jean-Gabriel Legoux[1], Peter G. Keech[2], David Doyle[2], Pellumb Jakupi[3] and Eric Irissou[1]
[1]National Research Council Canada
[2]NWMO
[3]Western University

This report has been prepared under contract to NWMO. The report has been reviewed by NWMO, but the views and conclusions are those of the authors and do not necessarily represent those of the NWMO.

Document History

Title:	Development of Cold Spray Technology for Copper Coating of Carbon Steel Used Fuel Container Prototypes for CANDU Fuel		
Report Number:	NWMO TR-2015-29		
Revision:	R000	Date:	November 2015
National Research Council Canada / Western University			
Authored by:	Phuong Vo, Dominique Poirier, Pellumb Jakupi		
Verified by:	Jean-Gabriel Legoux		
Approved by:	Eric Irissou		
Nuclear Waste Management Organization			
Reviewed by:	Peter G. Keech		
Reviewed by:	David Doyle		
Reviewed by:	Jose Freire-Canosa		
Accepted by:	Christopher Hatton		

ABSTRACT

Title: **Development of Cold Spray Technology for Copper Coating of Carbon Steel Used Fuel Container Prototypes for CANDU Fuel**
Report No.: **NWMO TR-2015-29**
Author(s): Phuong Vo, Dominique Poirier, Jean-Gabriel Legoux, Peter G. Keech, David Doyle, Pellumb Jakupi, and Eric Irissou
Company: National Research Council Canada, Western University, NWMO
Date: November 2015

Abstract

The NWMO, in collaboration with the National Research Council (NRC), is investigating the use of cold spray technology to copper coat the NWMO proposed carbon steel Used Fuel Container (UFC) dedicated to the storage of used CANDU fuel in a Deep Geological repository (DGR). Copper coating is applied to the external surfaces of UFCs for corrosion protection.

In this report, a summary of the preliminary research and development program activities to assess the viability of using the cold spray technology is presented. Results from the tests are documented and applied to demonstrate and optimize the application of copper coating on a full-scale UFC prototype.

Research to date has included the different tasks required to successfully apply copper coatings of various thicknesses on steel substrates of varied dimensions: from small coupons for corrosion studies to larger pieces for mechanical tests, key geometric parts of the UFCs such as the hemispherical heads, and a full-scale UFC prototype, including its weld closure. Activities involved: (i) powder selection, (ii) general coating development, (iii) UFC coating optimization, and (iv) prototyping. Reference spraying and annealing conditions were established and coating quality and properties were validated on different substrate geometries and compositions. Results also indicated that powder manufacturing and robust handling procedures are key considerations for reliability and consistency of coating properties. A clear path to manufacturing copper coatings on UFCs via cold spray deposition was developed, including details on (i) process parameter scale-up adjustment, (ii) spray set up and pattern development, (iii) coating joining procedure, and (iv) coating machining.

The program was successful in demonstrating the potential use of cold spray technology for the protection of UFCs by achieving the manufacture of a full-scale prototype to NWMO specifications. However, further extensive validation work will be required prior to the implementation of cold spray coatings for UFC manufacture.

TABLE OF CONTENTS

Page

ABSTRACT iii

LIST OF FIGURES vii

1. INTRODUCTION 1

2. PRELIMINARY DEVELOPMENT AND TESTING PROGRAM 2

3. POWDER SELECTION 4

3.1 INITIAL SCREENING BASED ON POWDER PROPERTIES 4
3.2 POWDER SELECTION BASED ON COATING PROPERTIES 7

4. GENERAL COATING DEVELOPMENT 10

4.1 GENERAL SELECTION OF COATING PARAMETERS 10
4.2 GENERAL REPAIR OF DAMAGED COATINGS 14
4.3 GENERAL SELECTION OF ANNEALING CONDITIONS 15
4.4 GENERAL MICROSTRUCTURAL CHARACTERIZATION BY EBSD 20

5. USED FUEL CONTAINER COATING OPTIMIZATION 25

5.1 VALIDATION OF REFERENCE COATING ON PLANAR SUBSTRATES 25
5.2 APPLICATION OF REFERENCE COATING TO WELD SAMPLES 29
5.3 APPLICATION OF REFERENCE COATING TO CAST IRON SUBSTRATES 30
5.4 OPTIMIZATION OF ANNEALING CONDITIONS 31

6. PROTOTYPING 36

6.1 PROCESS ADJUSTMENTS 36
6.2 CYLINDRICAL BODY 37
6.3 HEMISPHERICAL HEAD 38
6.4 MOCK-UP AND LOWER ASSEMBLY 39
6.5 CLOSURE WELD 39

7. CONCLUSIONS 40

ACKNOWLEDGEMENTS 40

REFERENCES 41

APPENDIX A: PROCEDURES AND ADDITIONAL DATA 43

A.1 SUMMARY OF SPRAY CONDITIONS AND CHARACTERIZATION DATA 44

A.2 EXPERIMENTAL PROCEDURES 51

A.3 GENERAL SELECTION OF ANNEALING CONDITIONS – ADDITIONAL EXPERIMENTS 57

A.4 SAMPLE PRODUCTION FOR CORROSION TESTING 62

LIST OF TABLES

Page

Table 1: Spray conditions employed in various development stages. 3
Table 2: Selected characterization data for feedstock powders. 5
Table 3: Selected characterization results for N_2-sprayed coatings annealed for 1 h at 300 °C and 600 °C. 15
Table 4: Spray conditions employed for EBSD samples. 20
Table 5: Selected characterization results for N_2-sprayed coatings annealed for 1 h at 350 °C, 400 °C, and 600 °C. 31
Table 6: Spray conditions and coating characterization results for powder selection (section 3). 44
Table 7: Spray conditions and coating characterization results for selection of coating parameters (section 4.1). 45
Table 8: Spray conditions and coating characterization results for general selection of annealing conditions (section 4.3). 45
Table 9: Spray conditions for production of corrosion test coatings used in EBSD analysis (section 4.4). 46
Table 10: Spray conditions and coating characterization results for validation of reference coatings (section 5.1). 47
Table 11: Spray conditions and coating characterization results for reference coatings on weld substrates (section 5.2). 47
Table 12: Spray conditions and coating characterization results for reference coatings on cast iron substrates (section 5.3). 48
Table 13: Spray conditions and coating characterization results for optimization of annealing conditions (section 5.4). 48
Table 14: Spray conditions for prototyping (section 6). 49
Table 15: NRC ID numbers for each coating label. 50
Table 16: Substrate materials used by task. 51
Table 17: Nominal compositions and yield strengths of A36, A516 grade 70, and A106 grade B steels. 52
Table 18: Tensile test (sub-size) specimen dimensions. 55
Table 19: Selected characterization results for N_2- and He-sprayed coatings annealed for 1 h at 300 °C and 600 °C. 57

LIST OF FIGURES

Page

Figure 1: Deep geological repository concept. 1
Figure 2: Coating setups for (a,b) general coating development, (c,d) UFC coating optimization, and (e-h) prototyping. 3
Figure 3: Feedstock powder morphologies: (a) supplier 1, d_{50} = 20 µm; (b) supplier 1, d_{50} = 42 µm; (c) supplier 2, d_{50} = 23 µm; (d) supplier 2, d_{50} = 29 µm; (e) supplier 3, d_{50} = 26 µm; (f) supplier 3, d_{50} = 49 µm; (g) supplier 4, d_{50} = n/a; and (h) supplier 5, d_{50} = 30 µm. 6
Figure 4: Feedstock powder (etched) microstructures: (a) supplier 1, d_{50} = 20 µm; (b) supplier 1, d_{50} = 42 µm; (c) supplier 2, d_{50} = 23 µm; (d) supplier 2, d_{50} = 29 µm; (e) supplier 3, d_{50} = 26 µm; (f) supplier 3, d_{50} = 49 µm; (g) supplier 4, d_{50} = n/a; and (h) supplier 5, d_{50} = 30 µm. 6
Figure 5: Particle velocity versus d_{50} values of powders at various N_2 gas temperatures and pressures. 7
Figure 6: Surface roughness (arithmetic average roughness, R_a), microhardness (Vickers, $HV_{0.01}$), bond strength, and porosity versus particle velocity for N_2 sprayed coatings produced with different feedstock powders. 8
Figure 7: As-polished cross-sections of coatings produced at Tg = 800 °C and Pg = 4 MPa with different feedstock powders: (a) supplier 1, d_{50} = 20 µm; (b) supplier 1, d_{50} = 42 µm; (c) supplier 2, d_{50} = 23 µm; (d) supplier 2, d_{50} = 29 µm; (e) supplier 3, d_{50} = 26 µm; and (f) supplier 3, d_{50} = 49 µm. 9
Figure 8: Particle velocity for d_{50} = 42 µm powder versus gas temperature at various gas pressures and standoff distances (N_2 process gas). 11
Figure 9: Surface roughness (arithmetic average roughness, R_a), microhardness (Vickers, $HV_{0.01}$), bond strength, and porosity versus particle velocity for coatings produced with different spray conditions (d_{50} = 42 µm powder, N_2 process gas only). 12
Figure 10: (a) Top view and (b) cross-section of He-sprayed coating and (c) top view and (d) cross-section of N_2-sprayed coating. 13
Figure 11: (a) As-polished and (b) etched cross-sections of coating repair of a 600 µm deep V-notch scratch (identical spray conditions for repair and base coatings). 14
Figure 12: Microhardness as a function of anneal temperature for N_2-sprayed coatings (d_{50} = 23 µm powder). 16
Figure 13: Selected results for N_2-sprayed coatings (d_{50} = 23 µm powder) after annealing at various temperatures (polished cross-sections obtained): (a) as-sprayed, (b) after 300 °C/1 h anneal, and (c) after 600 °C/1 h anneal (etched microstructures obtained) (d) as-sprayed, (e) after 300 °C/1 h anneal, and (f) after 600 °C/1 h anneal; and fracture surfaces of tensile specimens (g) as-sprayed, (h) after 300 °C/1 h anneal, and (i) after 600 °C/1 h anneal. 17
Figure 14: Representative stress-strain curves for N_2-sprayed coatings after annealing (d_{50} = 23 µm powder). 18
Figure 15: Photos of bend test specimens for N_2-sprayed coatings (d_{50} = 23 µm powder) after annealing (a) As-sprayed coating (b) coating after heat treatment 1h@300°C, coating after heat treatment 1h@600°C. 18
Figure 16: Euler contrast EBSD map of d_{50} = 12.5 µm powder. Source: (Jakupi et al. 2015). 21
Figure 17: Feedstock powder morphologies: (a) supplier 6, d_{50} = 12.5 µm; (b) supplier 1, d_{50} = 42 µm. 21
Figure 18: Electron micrographs and corresponding EBSD IPF maps recorded at the Cu-coating/steel interface: (a) and (b) cold sprayed at 300°C (3 MPa): (c) and (d) cold sprayed at 600°C (5 MPa): (e) and (f) cold sprayed at 800°C (5 MPa). The indexing rates were 68%, 84% and 86% for (b), (d) and (f), respectively. Source: (Jakupi et al. 2015). 22

Figure 19: EBSD IPF maps and corresponding strain maps produced for regions where the cold spray carrier gas was switched from He to N_2 for spray conditions of (a, b) 600°C (5 MPa) and (c,d) 800°C (5 MPa): the indexing rates were 85 % and 83 %, respectively. Source: (Jakupi et al. 2015).....23
Figure 20: EBSD IPF maps and corresponding SE micrographs of post-annealed (4 h, 400°C) Cu coatings formed with cold spray conditions (a, b) 300°C (3 MPa), (c, d) 600°C (5 MPa) and (e, f) 800°C (5 MPa); the indexing rates were 83 %, 87 %, and 89 %, respectively. Source: (Jakupi et al. 2015). 24
Figure 21: As-polished coatings (d_{50} = 42 µm powder on A36 substrate) produced during UFC process optimization using: (a) initial reference parameters with T_g = 800 °C; (b) parameters similar to those in (a) but without He bond coat, with doubled gun traverse speed, and with doubled substrate rotation speed; and (c) optimized reference parameters with T_g = 600 °C. 26
Figure 22: Photos of coatings prepared at various thicknesses (d_{50} = 42 µm powder) produced during UFC process optimization: As-sprayed coating top views for (a) 3.7 mm (b) 6.1 mm (c) 9.6 mm; As-sprayed coating side views for (d) 3.7 mm (e) 6.1 mm and (f) 9.6 mm; (g) As-machined coating top view for 2.7 mm (white streaks are artefacts due to reflections..27
Figure 23: As-polished coatings (d_{50} = 42 µm powder) produced during UFC process optimization using optimized reference parameters with T_g = 600 °C on different substrates: (a, e) A36 substrate, (b, f) A516 grade 70 substrate, (c, g) welded A516 grade 70 substrate, and (d, h) cast iron substrate.....28
Figure 24: Test jig used by Exova with a representative test specimen inserted. The white dots on the test specimen are reference marks for elongation measurement. 29
Figure 25: As-received welded A516 grade 70 steel substrate: (a) photo of cross-section showing approximate locations of optical micrographs; and optical micrographs of (b) base metal and (c) centre of the weld. 30
Figure 26: Reference coatings (d_{50} = 42 µm powder): as-polished microstructures for (a) as-sprayed, (b) after 350 °C/1 h anneal, and (c) after 400 °C/1 h anneal; and etched microstructures for (d) as-sprayed, (e) after 350 °C/1 h anneal, and (f) after 400 °C/1 h anneal. 32
Figure 27: Representative stress-strain curves for reference coating coatings (d_{50} = 42 µm powder) as-sprayed and after anneal for 1 h at 350 °C, 400 °C, and 600 °C. 33
Figure 28: Representative stress-strain curves for A516 grade 70 as-received and after annealing for 1 h at 350 °C and 600 °C. 34
Figure 29: Representative photos after bend testing of reference coatings (d_{50} = 42 µm powder): (a) as-sprayed, (b) after 350 °C/1 h anneal, and (c) after 600 °C/1 h anneal. 34
Figure 30: Representative micrographs of low-strength, cohesive failure after 600 °C anneal: cross-section at low magnification of (a) one side of failure and (b) opposite side; fracture surface at low magnification of (c) one side and (d) second region of same side; cross-section at high magnification of (e) one side of failure and (f) opposite side; fracture surface at high magnification of (g) one side and (h) second region of same side. 36
Figure 31: Photos of coating (d_{50} = 42 µm powder) produced on A106 grade C steel: (a) top view as-sprayed, (b) side view as-sprayed, (c) side view after machining. 38
Figure 32: Photos showing coating development for hemispherical head: (a) coated dishes (with geometry matching that of the apex) used in the optimization of a curved spray pattern, (b) apex coated using an XY pattern with masking, (c) coated hemisphere sectioned for characterization, and (d) CNC machining of a coated hemisphere. 38
Figure 33: Full-sized lower assembly (a) after coating of two sections, (b) after coating of entire lower assembly, and (c) after partial machining of lower assembly. 39

Figure 34: Full-sized leading assembly: (a) close-up of closure weld area after welding and machining, (b) installed with collars on roller frame prior to coating of the closure weld, and (c) after coating and machining of the closure weld. 40
Figure 35: Alumina grit characteristics: (a) particle size distribution and (b) alumina particle morphology. 52
Figure 36: Tensile test specimen schematic (ASTM International 2009b) 55
Figure 37: Microhardness as a function of anneal temperature for He-sprayed coatings (d_{50} = 23 µm powder for N_2-spray and d_{50} = 42 µm powder for He-spray). 58
Figure 38: Representative stress-strain curves for He-sprayed and N_2-sprayed coatings (d_{50} = 23 µm powder for N_2-spray and d_{50} = 42 µm powder for He-spray). 59
Figure 39: Representative fracture surfaces of tensile specimens for coatings: (a, e) N_2-sprayed, as-sprayed; (b, f) N_2-sprayed and annealed for 1 h at 600 °C; (c, g) He-sprayed, as-sprayed; (d, h) He-sprayed and annealed for 1 h at 600 °C;. 60
Figure 40: Representative stress-strain curves for N_2-sprayed coatings using d_{50} = 23 µm and d_{50} = 42 µm powders. 61
Figure 41: (a) Photograph of ADCS copper coating on mild steel plate for corrosion scoping testing and (b) scratch and sample pattern for testing. 63
Figure 42: Photos of corrosion sample (exposure testing) production: (a) setup for OD coating, (b) OD coating pieces machined to 9.5 mm Ø x 38.1 mm length, (c) grit blasted pieces fixed into substrate holder, (d) top coating spray with rotating substrate holder and horizontally moving PCS-800 unit, (e) pieces after top coating applied, (f) top coating pieces with 6.4 mm thick substrate, (g) pieces in substrate holder with back face coatings applied, and (h) side view of corrosion sample. 64

1. INTRODUCTION

The Nuclear Waste Management Organization (NWMO) was established in 2002 under the Nuclear Fuel Waste Act (NFWA) to investigate approaches for managing Canada's used nuclear fuel. The current approach is to store the used fuel in specially designed containers of carbon steel coated with copper to protect the container from corrosion when emplaced in a Deep Geological Repository (DGR) (Figure 1).

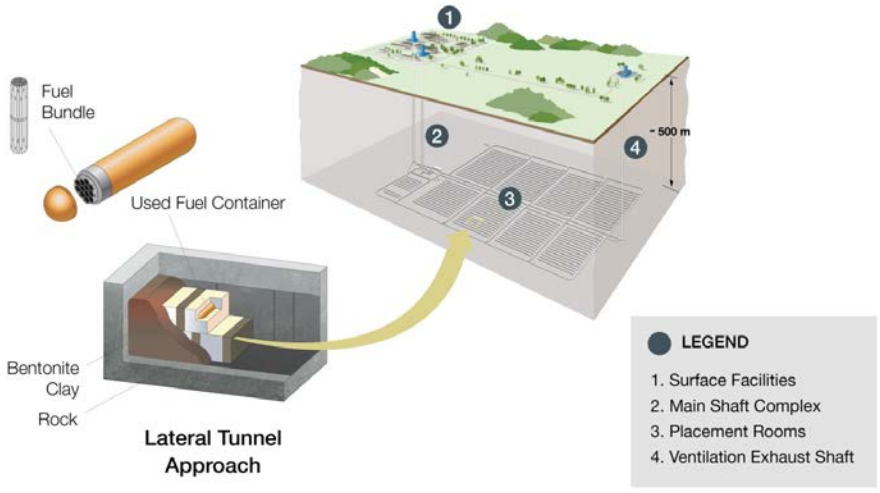


Figure 1: Deep geological repository concept.

For corrosion purposes, only a very thin layer of copper is required. Resistance to corrosion by groundwater for a 100 000 year period can be achieved with less than 0.4 mm of copper, while copper losses via corrosion can be expected to be below 1.27 mm over 1 000 000 years (Kwong 2011). Copper cold spray technology offers to provide the required corrosion protection to the steel container in an effective, simple way, eliminating the need to independently manufacture an outer shell of copper to protect the inner carbon steel container. In addition to handling and assembly issues associated to the use of an outer copper shell, such a component is susceptible to creep during emplacement (Sandström and Wu 2013), while a coated part does not undergo this process.

Copper is one of the most common cold sprayed materials, and an extensive knowledge base on copper cold spray technology is available in the literature. Indeed, early developmental work into cold spray technology by a number of researchers was performed using copper (Dykhuizen et al. 1999; Gilmore et al. 1999; Van-Steenkiste et al. 1999; Alkhimov, Klinkov and Kosarev 2000; McCune et al. 2000; Papyrin 2001). The effects of various spray parameters were recently reviewed (Assadi et al. 2011) for the development of parameter selection maps for cold spraying. The review highlighted the relative influence of gas temperature and pressure parameters for copper cold spray. The characterization of microstructures and mechanical properties for copper coatings has shown that bulk-equivalent material can be obtained, provided appropriate spray conditions and post-spray heat treatments are employed (Calla, McCartney and Shipway 2006; Gartner et al. 2006; Stoltenhoff et al. 2006). Initial feasibility work for the specific application of cold spray copper on used fuel canisters has also been performed on small-dimension samples by researchers at the Korea Atomic Energy Research

Institute (Choi, Lee and Lee 2010; Kim et al. 2009; Lee et al. 2011). Work in copper coating using cold spray technology has been under development for the NWMO since 2011, and the cumulative results of the test program to date are being reported.

2. PRELIMINARY DEVELOPMENT AND TESTING PROGRAM

The preliminary development and testing program consisted of four general stages: (i) powder selection, (ii) general coating development, (iii) used fuel container coating process optimization for a full-scale used fuel container, and (iv) various prototyping activities, including copper coating of a full-scale UFC prototype. Future activities will include an extensive validation study of the resultant methodology within a series of settings, including the R&D environment, a pilot scale plant, and eventually a manufacturing plant, prior to the final selection of cold spray process inputs.

During powder selection, a range of commercial powders was screened, based on the powders' physical properties and the properties of their resulting as-sprayed coatings. The collected data were used to identify two suitable powder candidates for cold spray coating of steel substrates. The two most promising powders were then employed for general coating development to obtain an initial reference set of spray parameters and annealing conditions. In the third stage, reference parameters were optimized for UFC-specific materials and geometry. The prototyping stage involved final process adjustments and the production of mock-up assemblies in the R&D setting.

Several types of spray setups, with fixtures for smaller flat test substrates and larger spherical/cylindrical mock-up assemblies, used in the various development stages, are illustrated in Figure 2. The cold spray systems employed at various stages in the development process included the Kinetiks 4000 (Oerlikon Metco, Westbury, NY) and the PCS-800 and PCS-1000 (Plasma Giken Co., Ltd., Toshima-ku, Tokyo) using helium and/or nitrogen as the accelerating gas. The general spray conditions are documented in Table 1, and specific spray conditions for each development stage in Appendix A.1. Heat treatments were performed using a tube furnace with an argon atmosphere. A wide range of characterization methods was used during the program, such as: powder size by laser diffraction; powder flowability by MPIF standard_03 (Metal Powder Industries Federation 1985); chemical analysis by inert gas fusion; particle velocity by time-of-flight optical particle diagnostics (cold spray meter); Vickers microhardness by ASTM 384 (ASTM International 2010); surface roughness by stylus profilometer; surface topography by confocal microscopy; porosity measurement by image analysis; bond strength by ASTM C 633 (ASTM International 2001) and/or modified ASTM E 8 (ASTM International 2011); tensile testing by ASTM E 8 (ASTM International 2009b); bend testing by ASTM E 290 (ASTM International 2009a); and microstructural analysis by scanning electron microscopy (SEM) and/or optical microscopy. The experimental procedures are detailed in Appendix A.2.

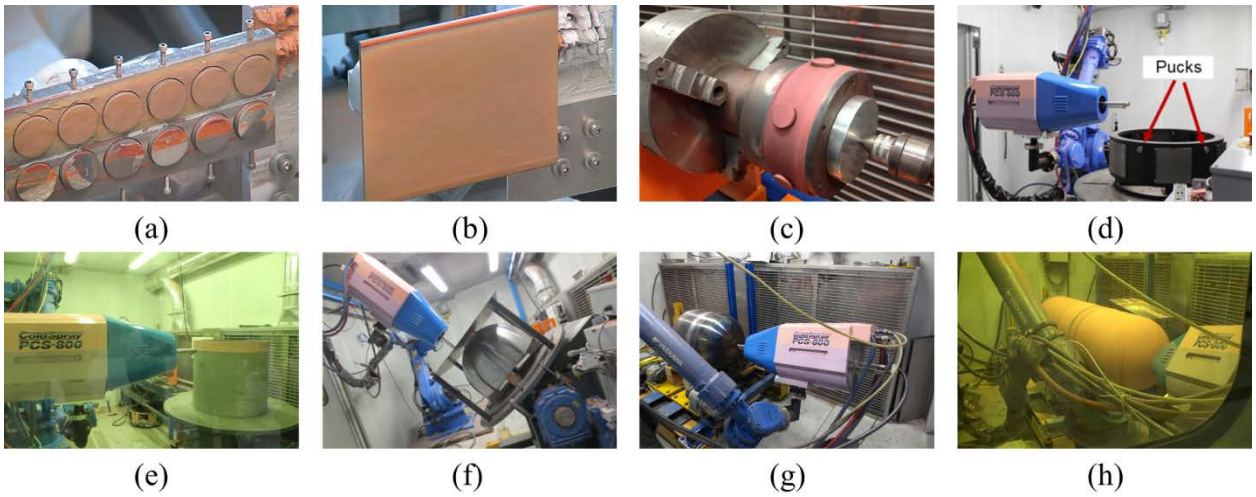


Figure 2: Coating setups for (a,b) general coating development, (c,d) UFC coating optimization, and (e-h) prototyping.

Table 1: Spray conditions employed in various development stages.

Conditions*	Powder Selection	General Coating Development		UFC Optimization and Prototyping
	N_2-spray	N_2-spray	He-spray	N_2- and He-spray
System	PCS-1000	PCS-1000	Kinetiks 4000	PCS-800, PCS-1000
Powder, d_{50} (µm)	20, 23, 26, 29, 42, 49	23, 42	42	42
Gas temp., T_g (°C)	400, 600, 800	400, 500, 600, 700, 800	350	600, 800
Gas pressure, P_g (MPa)	2, 3, 4	3, 5	3.5	4.5-5
Traverse speed (mm/s)	300	60, 100, 1000	100	0.6-300†
Step size (mm)	1	1	1.25	1
Substrate rotation (rpm)	n/a	n/a	n/a	23.5-238†
Standoff distance (mm)	25	25, 100, 200	40	30

* Specific spray conditions for each stage are detailed in Appendix A.1.
† Large range due to different diameters of substrate holders and mock-up assemblies.

3. POWDER SELECTION

3.1 INITIAL SCREENING BASED ON POWDER PROPERTIES

For initial screening, eight commercially available copper powders were selected and acquired from five different suppliers. Powders will be referred to hereafter by powder size (d_{50} value) and/or supplier (suppliers 1-5), where appropriate. Initial screening of the powders was performed through a characterization of the powder composition as well as the powder size, morphology, and flowability. In general, the ideal copper powder size distribution (PSD) features average, maximum and minimum powder particle sizes as small as reasonably possible because small particles can be accelerated to higher velocities by the cold spray gas jet. However, the minimum powder size must be greater than 8 µm, which is the critical particle diameter required for adiabatic shear instability with copper powder particles (Schmidt et al. 2006). Unimodal particle size distributions are also favored as they tend to produce more homogeneous coatings. The flowability, which can be affected by powder size and morphology, is a practical consideration in powder feeding. Table 2 compares the chemical composition of the various feedstock powders with UNS C10100 oxygen free copper's acceptable levels of impurities. The C10100 benchmark was initially established by NWMO as it is one material that is extensively used in corrosion testing due to its high copper purity (> 99.99 %). A second reference copper within NWMO and other nuclear waste organizational work is oxygen-free phosphorus-doped copper (CuOFP), a form of copper with similar corrosion properties in deep geological repositories, but with improved creep ductility properties owing to the 30-100 ppm phosphorus doping (Sandström and Andersson 2008). Most powders exceeded C10100 limits for Sn, Fe, and Zn, while excess Ag, Bi, Mn, Ni, Pb, Sb and Se were found in some; this may indicate a need to evaluate the feasibility of manufacturing powders with tighter composition control in future NWMO programs, should highly pure coatings be desirable. Overall, powders from supplier 1 displayed the highest purity, and the analyses suggest that C10100 specifications could be met, if required, with the proper manufacturing method and raw material composition.

Among the examined powders, spherical powders were produced using gas or plasma atomization, while the irregular powder was produced using water atomization. Powders from suppliers 4 and 5 displayed relatively high oxygen content, with values of 1.130 % and 0.211 %, respectively. The latter value was somewhat surprisingly high as the plasma atomization manufacturing process was performed in vacuum; although it might be that the powder was obtained from an old powder lot. The oxygen content varied from 0.022 % to 0.113 % for other powders, with higher values for the smaller powders, due to their higher specific surface area. Feedstock powders were kept in a glove box under an inert, nitrogen atmosphere between cold spraying sessions to prevent oxidation. If it is determined that the final application requires ultralow oxygen level coatings, then emphasis must be placed on the proper handling of the feedstock powders to limit their uptake of oxygen during storage and handling, which can be higher than that from the cold spraying process itself.

Table 2: Selected characterization data for feedstock powders.

Supplier, d_{50}	Chemical Analysis							PSD			Flowability
	Cu	O	Ag	S	Fe	Ni	Other[b]	d_{10}	d_{50}	d_{90}	
µm	Wt. %	Wt. %	Wt. ppm	Wt. ppm	Wt. ppm	Wt. ppm	Wt. ppm	µm	µm	µm	s/50 g
1, 20	99.89	0.080	18	12	28	5	5P, 5Sn, 29Zn	9	20	34	5.2 [c]
1, 42	99.92	0.054	27	11	3	7	4P, 2.2Sn	17	42	62	10.7
2, 23	99.85	0.107	21	11	3	2	212P	14	23	35	22.4
2, 29	99.83	0.113	11	12	71	11	198P, 92Sn, 12Zn, 20Bi, 4Mn	12	29	52	5.4 [c]
3, 26	99.84	0.106	54	11	25	93	51Pb, 7Sb, 29P, 198Sn, 20Zn, 4Se	12	26	36	33.2
3, 49	99.86	0.022	54	11	22	46	49Pb, 11Sb, 26P, 8Se, 810Sn, 12Zn, 1.6Bi,	37	49	70	12.2
4, (n/a)	n/a	1.130	(dropped from study)					n/a	n/a	n/a	Failed
5, 31	n/a	0.211	(dropped from study)					14	31	43	11.9
C10100[a]	99.99	0.005	25	15	10	10	4Pb, 4Sb, 3P, 3Se, 1Sn, 1Zn, 1Bi, 0.5Mn	n/a	n/a	n/a	n/a

[a] ASTM B152-09 (ASTM International 2006): min limit for Cu; max limit for all other elements.
[b] Only non-conforming values to C10100 listed for powders; max values for C10100.
[c] No flow through MPIF 3 standard funnel with 50 g of powder (i.e., method used for other measurements). Value obtained from flow of 100 g of powder through a 5 mm diameter funnel.

A summary of powder size and flowability is also shown in Table 2. Powder d_{50} values ranged from 20 µm to 49 µm, with suppliers 1, 2, and 3 each providing two size distributions. Larger average particle size powders from the same supplier displayed better flowability values than their smaller counterparts. The surface appearance and morphology of powder particles from suppliers 1, 2, and 3, shown in Figure 3, can also be broadly described, respectively, as follows: spherical and satellite-free (a-b); irregular and satellite free (c-d); and spherical with fine satellites (e-f). The difference in sphericity measured between spherical and irregular powders was: ~ 0.03 - 0.14 (sphericity values of 0.81 ± 0.17, 0.88 ± 0.15, 0.78 ± 0.16, 0.76 ± 0.13, 0.90 ± 0.12, and 0.82 ± 0.18 for powders shown in Figure 3a-f, respectively). Microstructures of the feedstock powders, shown in Figure 4, revealed qualitatively that the spherical powders (a,b and e,f) displayed generally coarser grains compared to the irregular powders (c and d).

Initial screening based on the powder properties eliminated powders from suppliers 4 and 5 due to their very high oxygen contents (> 0.2 %) and/or poor flowability (e.g., leading to a failed test for supplier 4 powder). However, irrespective of deviations from the C10100 specification, the remaining six candidates were deemed acceptable in composition, size, and flowability. Consequently, powder selection between these six powders was done by assessing their coating properties.

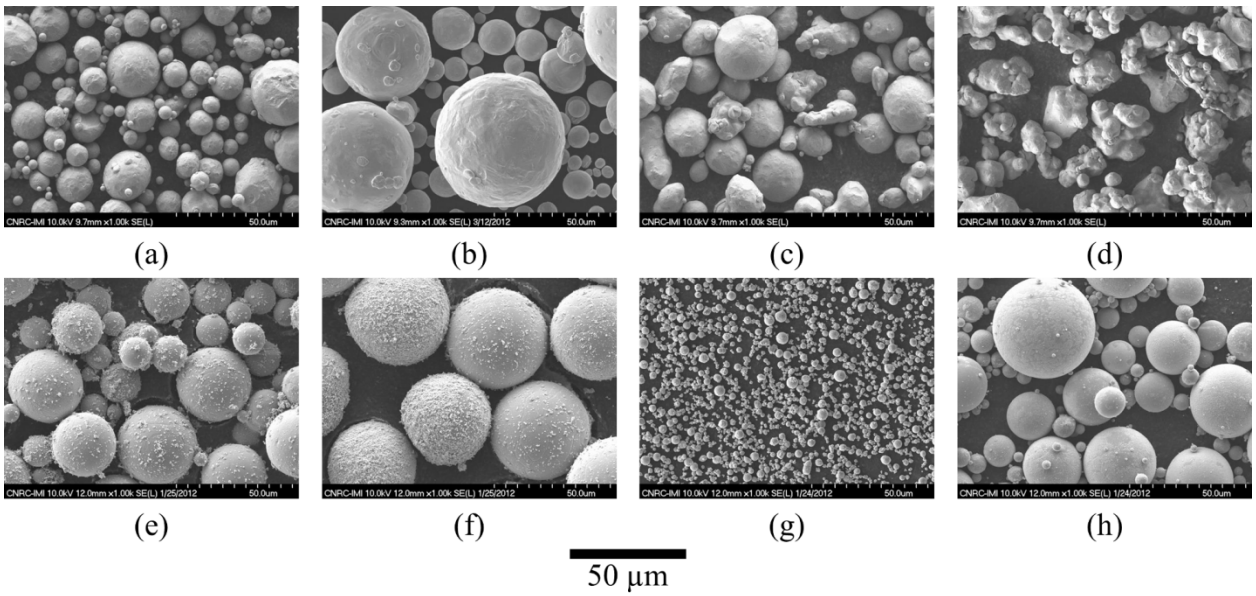


Figure 3: Feedstock powder morphologies: (a) supplier 1, d_{50} = 20 µm; (b) supplier 1, d_{50} = 42 µm; (c) supplier 2, d_{50} = 23 µm; (d) supplier 2, d_{50} = 29 µm; (e) supplier 3, d_{50} = 26 µm; (f) supplier 3, d_{50} = 49 µm; (g) supplier 4, d_{50} = n/a; and (h) supplier 5, d_{50} = 30 µm.

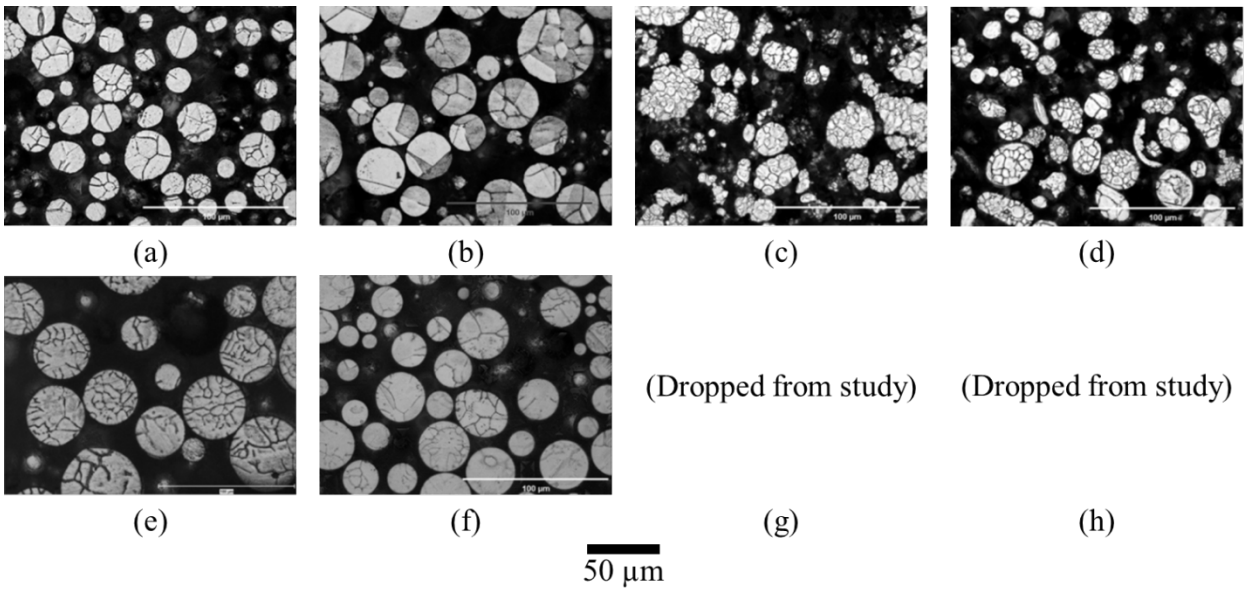


Figure 4: Feedstock powder (etched) microstructures: (a) supplier 1, d_{50} = 20 µm; (b) supplier 1, d_{50} = 42 µm; (c) supplier 2, d_{50} = 23 µm; (d) supplier 2, d_{50} = 29 µm; (e) supplier 3, d_{50} = 26 µm; (f) supplier 3, d_{50} = 49 µm; (g) supplier 4, d_{50} = n/a; and (h) supplier 5, d_{50} = 30 µm.

3.2 POWDER SELECTION BASED ON COATING PROPERTIES

The six candidate powders from suppliers 1-3 were N_2-sprayed using three gas temperature/pressure combinations (400 °C/2 MPa, 600 °C/3 MPa, and 800 °C/4 MPa). The spray conditions and selected coating characterization data are summarized in Appendix A.1. Coatings of 0.3-1.0 mm thickness were produced on 3.2 mm thick plates and > 50 mm thick cylinders of low carbon steel, with the latter used for bond strength testing. The powder particle velocities were measured and coatings screened by bond strength, porosity, and microstructure. Surface roughness and microhardness were also measured; however, these results did not influence the selection process.

The highest particle velocities were obtained with the irregular powder from supplier 2, due to the higher drag force in that case, as the particle velocity is a function of the drag force (F_d) on the particle, where ($F_d = m_p a_p = \frac{1}{2} C_d A_p \rho_g \left(v_g - v_p\right)^2$ where m_p is the particle mass, a_p is the particle acceleration, C_d is the drag coefficient, A_p is the particle cross-sectional area, ρ_g is the gas density, v_g is the gas velocity, and v_p is the particle velocity (Dykhuizen and Smith 1998). The particle velocities of all powders measured at the conditions chosen, which represent typical ranges of values used for the cold spray of copper, ranged from ~ 480 m/s to 820 m/s. These velocities appeared to be within the deposition window between critical and erosion velocities needed to provide high-quality coatings with good deposition efficiencies (~ 400-1100 m/s) (Schmidt et al. 2009), as shown in Figure 5. Here, the critical and erosion velocity lines correspond to the simulated values available in literature for 25 µm particles at room temperature (Schmidt et al. 2009) while the measurements correspond to powders with a range of particle sizes. Both velocities depend on the particle size, temperature, oxygen content, and substrate surface temperature.

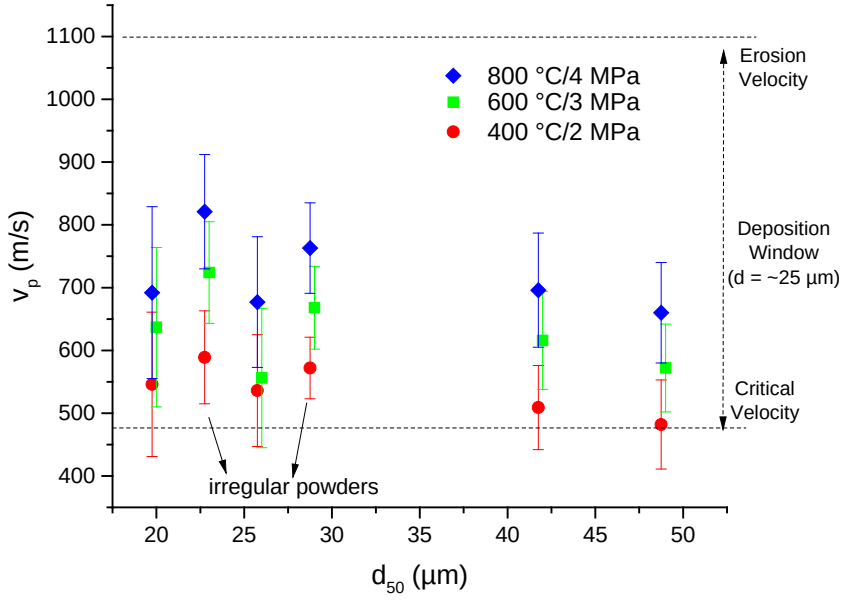


Figure 5: Particle velocity versus d_{50} values of powders at various N_2 gas temperatures and pressures.

The ASTM C 633 (ASTM International 2001) bond strength values were as high as 41 ± 5 MPa for 350 µm to 630 µm thick coatings. While higher particle velocity somewhat favored coating adhesion, the relationship between specific powders, spray conditions, and bond strength was

inconclusive, as shown in Figure 6. All powders allowed for the production of relatively dense coatings at the highest gas conditions (800 °C/4 MPa), as shown in Figure 7 for powders from suppliers 1-3. Some porosity was observed at lower (temperature and pressure) gas conditions and porosity measurements of coatings produced at 600 °C/3 MPa indicated that particle velocities above ~ 600-650 m/s resulted in less than ~ 0.5 % porosity. Smaller powders (and associated higher velocity) typically yielded lower porosity coatings than larger powders, although both d_{50} = 26 µm and d_{50} = 49 µm powders from supplier 3 displayed relatively high porosity coatings. This was assumed to be due to low associated particle velocities, although the fine surface satellites may also play a role.

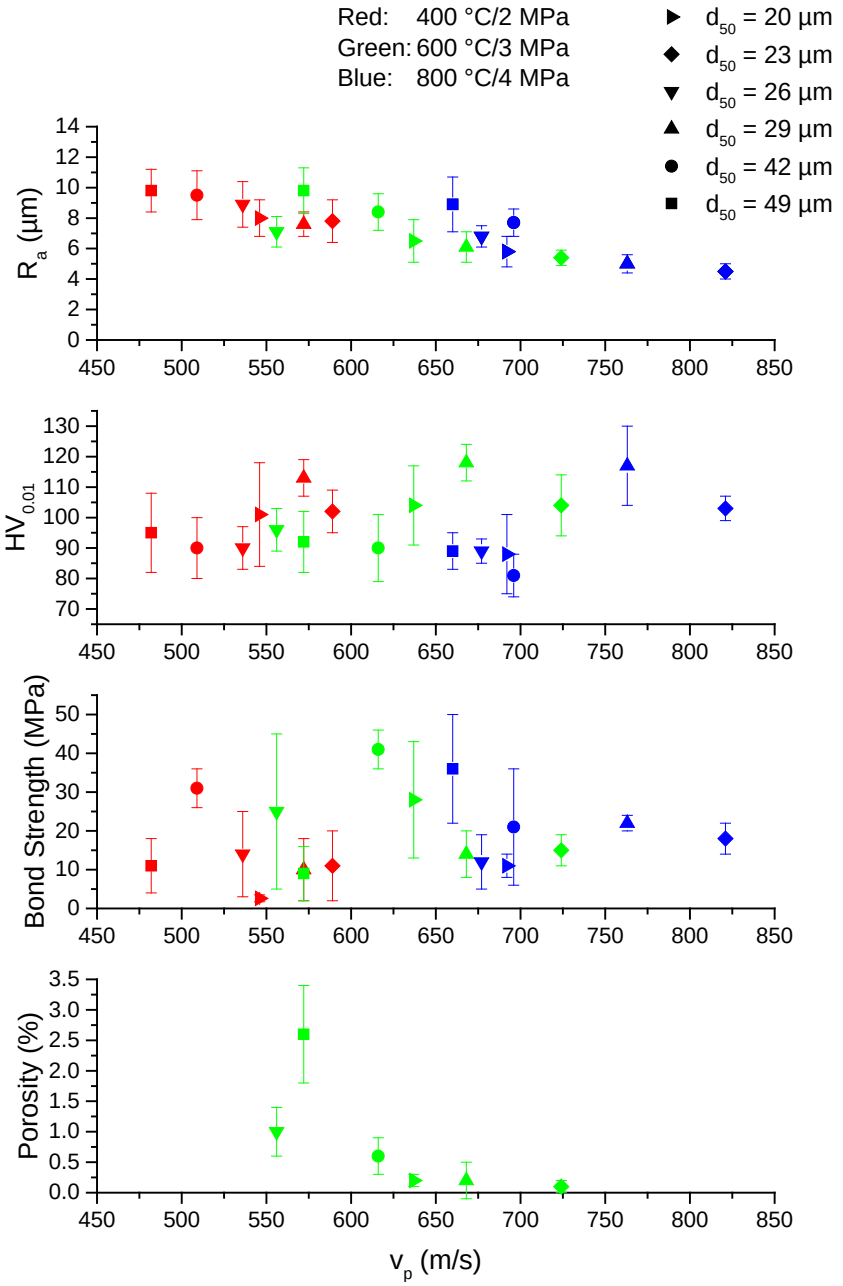


Figure 6: Surface roughness (arithmetic average roughness, R_a), microhardness (Vickers, $HV_{0.01}$), bond strength, and porosity versus particle velocity for N_2 sprayed coatings produced with different feedstock powders.

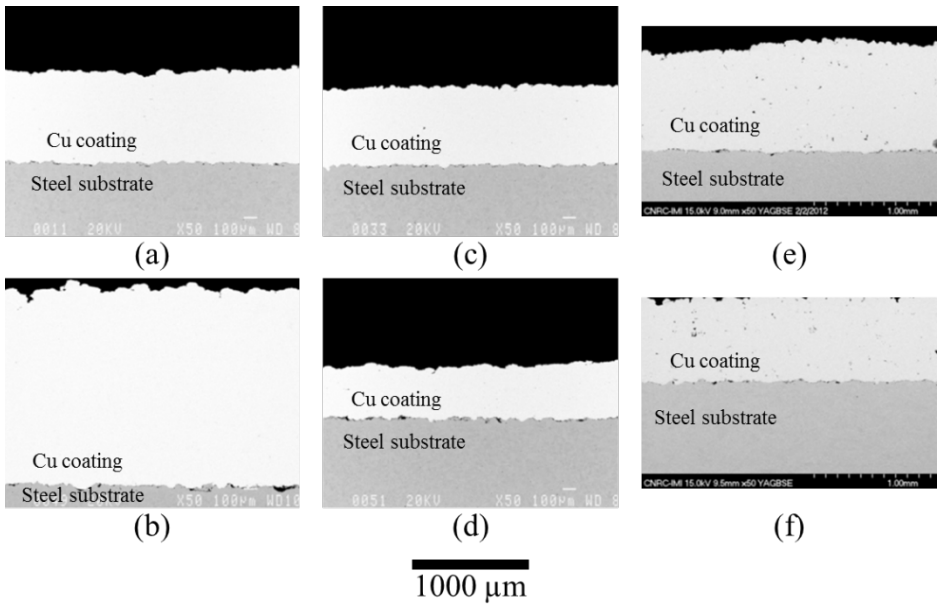


Figure 7: As-polished cross-sections of coatings produced at Tg = 800 °C and Pg = 4 MPa with different feedstock powders: (a) supplier 1, d_{50} = 20 µm; (b) supplier 1, d_{50} = 42 µm; (c) supplier 2, d_{50} = 23 µm; (d) supplier 2, d_{50} = 29 µm; (e) supplier 3, d_{50} = 26 µm; and (f) supplier 3, d_{50} = 49 µm.

The surface roughness, ranging from 4.5 ± 0.5 µm to 9.8 ± 1.5 µm, varied with feedstock powder size, as the larger powders from each supplier exhibited higher R_a values than their smaller counterparts at respective spray conditions. As shown in Figure 6, surface roughness decreased with higher particle velocity, which is dependent on particle size and morphology as well as higher gas temperature and pressure, due to the higher level of deformation of the impinging particles. A higher level of "waviness" (i.e., roughness on a macro scale), which was not reflected by a higher R_a value, was also observed for coatings produced with powders from supplier 2. As expected for coldspray coatings (Stoltenhoff et al. 2006), the microhardness values of as-deposited coatings, ranging from ~ 80-120 $HV_{0.01}$, were significantly higher than as-received values of 46 ± 3 $HV_{0.01}$ for bulk C10100 and 30-42 $HV_{0.01}$ (Appendix A.1). Vickers microhardness measurements could not be obtained for smaller powders (d_{50} < 30 µm). The hardness values of coatings produced using the irregular powder (supplier 2) were, in general, higher than those of coatings produced from spherical powders (suppliers 1 and 3) at respective conditions, which was attributed to higher particle velocities achieved with powders with irregular morphologies. Different spray conditions within the range tested did not significantly affect coating hardness for individual powders.

Based on the above coating characterization, no single powder proved to be significantly better than other powders. However, additional testing with the d_{50} = 26 µm powder from supplier 3 resulted in clogging of the powder injector and as a result, supplier 3 powders were eliminated from the study. As is very often the case, no specific powder characteristics were identified as the cause of clogging of this powder when compared to other powders. Clogging is a general issue that limits the number of powders available for practical use in cold spray. The powder-nozzle material couple, as well as nozzle and powder injector design, are important aspects to consider for nozzle clogging. Spraying parameters, such as a high process gas temperature,

can also trigger nozzle or injector clogging, although this was minimized with the use of the PCS-1000 gun that integrates nozzle cooling. It is also worth noting that clogging will be increased at higher feed rates, such as the very high rates that will probably be established for production, because the high ratio powder flow/gas flow will change the structure of the gas flow. In general, powders in the coarser range are recommended, as they offer better flowability, which is an important aspect in cold spraying. However, dense coatings were produced from most powders studied, regardless of their different attributes, which suggests powder availability from multiple sources, resulting in easy powder supply.

4. GENERAL COATING DEVELOPMENT

A comprehensive program was undertaken to investigate the effects of spray conditions and post-spray heat treatment conditions on copper coatings produced using a typical cold spray setup (i.e., an XY spray pattern on a generic substrate). The deposition of repair coatings into small V-notch scratches machined into previously coated plates was also performed on a limited scale to initially evaluate the feasibility of damage repair. The objective of this program was to develop a set of reference process parameters that would be optimized in subsequent UFC coating development and prototyping stages (described later). For the sake of brevity, only selected results will be discussed in this section with remaining results included in the Appendix. Extensive literature is also available concerning the general and fundamental aspects of cold spraying copper coatings (Dykhuizen et al. 1999; Gilmore et al. 1999; Van-Steenkiste et al. 1999; Alkhimov et al. 2000; McCune et al. 2000; Papyrin 2001; Assadi et al. 2011; Calla et al. 2006; Gartner et al. 2006; Stoltenhoff et al. 2006).

4.1 GENERAL SELECTION OF COATING PARAMETERS

For the selection of the general copper coating spray parameters, an 18 run Design of Experiments (DOE) was performed, varying powder properties, gas type, gas temperature, gas pressure, gun traverse speed, step size, and/or standoff distance. The spray conditions and selected coating characterization data are summarized in Appendix A.1. The d_{50} = 42 µm and d_{50} = 23 µm powders from suppliers 1 and 2, respectively, (c.f., Figure 3b and c, respectively) were tested. Powder from supplier 1 displayed relatively low oxygen content, high flowability, and high coating bond strength, while the powder from supplier 2 had an alternative (irregular) morphology and smaller particle size distribution. Coatings were produced on low carbon steel disk substrates (25.4 mm Ø × 6.35 mm thick), shown in Figure 2a, that were grit blasted with grit 24 (~ 975 µm) alumina.

A chemical analysis of selected coatings showed that oxidation caused by the cold spray process was limited. Coatings sprayed at 800 °C with N_2 gas using d_{50} = 42 µm powder displayed 0.066 % [O] compared to 0.054 % in the as-received powder. A surprising higher O content measured for the as-received d_{50} = 23 µm powder (0.107 %) compared to the coating (0.023 %) was possibly due to oxidation during powder handling. The similarity of oxygen contents in powders and coatings was also observed during testing for the powder selection (not shown). Switching to He gas spray at 350 °C in an enclosed He atmosphere for a full thickness He coating did not significantly change the oxygen pickup, with 0.018 % measured for a coating with d_{50} = 42 µm powder.

The combined effects of gas temperature, gas pressure, and standoff distance on average particle velocity were measured for N_2-sprayed d_{50} = 42 µm powder, as shown in Figure 8. The particle velocity for the He-sprayed condition was not measured and is not shown. The particle velocity progressively increased with gas temperature from 400 °C to 700 °C (~ 571 m/s to 691 m/s, respectively, at 5 MPa gas pressure and 25 mm standoff) and then plateaued between 700 °C and 800 °C (693 m/s). Optimization of the standoff distance at 100 mm produced an increase of ~ 50 m/s (at 600 °C to 800 °C), which was similar to the change in particle velocity caused by an increase in gas pressure from 3 MPa to 5 MPa (at 600 °C).

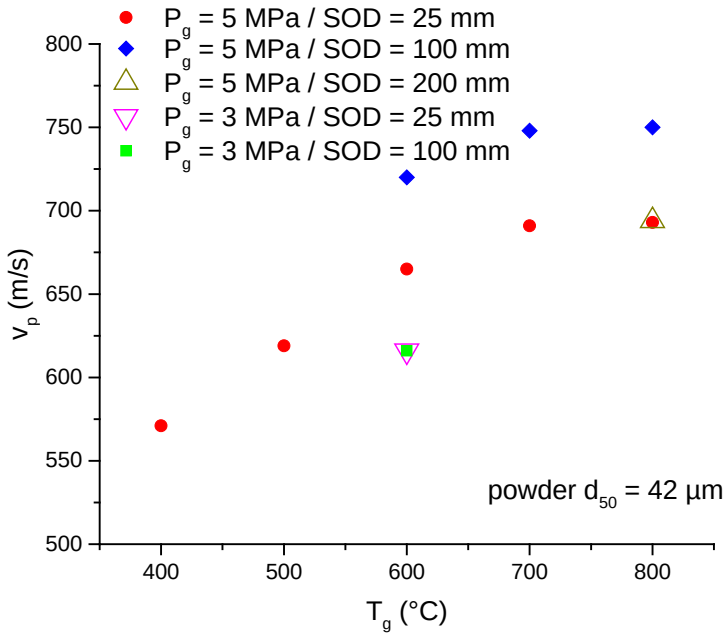


Figure 8: Particle velocity for d_{50} = 42 µm powder versus gas temperature at various gas pressures and standoff distances (N_2 process gas).

The effect of changing particle velocity by varying the spray parameters on coatings produced using the d_{50} = 42 µm powder and N_2 gas is shown in Figure 9. The data in these graphs were obtained from coatings produced using spray gun traverse speeds of 60 or 1000 mm/s. Bond strength results clearly show that particle velocity was not the only key parameter contributing to coating adhesion (e.g., refer to 2 data points at ~700 m/s obtained with different gun traverse speeds). The ASTM C 633 (ASTM International 2001) bond strength of coatings sprayed onto the 6.35 mm thick steel disks ranged up to 29.4 ± 9.9 MPa, although the majority of coatings displayed bond strength values below 10 MPa. Bond strengths greater than or equal to ~ 20 MPa were only obtained using gas temperatures of 800 °C when using N_2 as the process gas. Extra trials were performed with He as the process gas with the following rational; He can be accelerated to higher speed than N_2 thanks to its lower density. The higher speed of the process gas will in turn accelerate the powder particles to higher speeds, potentially resulting in higher quality coatings. It was indeed found that a bond strength of 26.8 ± 4.0 MPa could be achieved with a He process gas temperature of 350°C and 3.5 MPa only (not shown in Figure 8 or Figure 9). Note that some spray parameters with He gas (Table 7 G1: GTS = 100 mm/s, SOD = 40 mm, Step = 2 mm) are different than those used with N_2 gas.

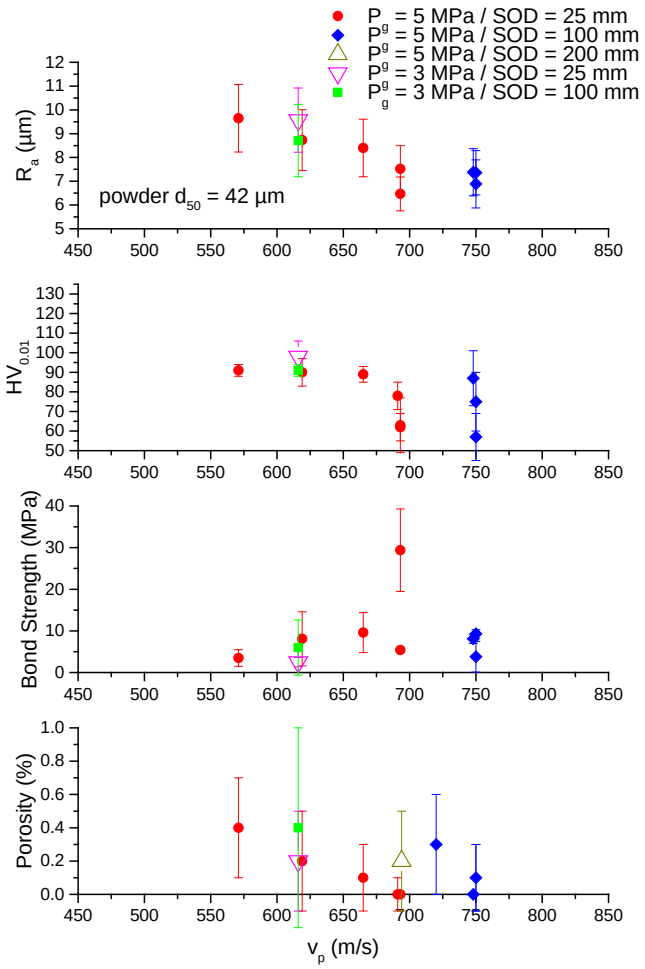


Figure 9: Surface roughness (arithmetic average roughness, R_a), microhardness (Vickers, $HV_{0.01}$), bond strength, and porosity versus particle velocity for coatings produced with different spray conditions (d_{50} = 42 µm powder, N_2 process gas only).

The variation in bond strength obtained for coatings produced during the DOE runs, as well as in the previous powder selection tests, illustrates the difficulty in developing optimal spray parameters for coating adhesion. This is a fundamentally important design parameter in the manufacture of UFCs. Bond strength may be influenced by a number of factors, such as specimen preparation, coating parameters, substrate condition, residual stresses, etc. Measurements are impacted by such things as rounding of the edges of thick coatings on disks, as this could generate a "notch-effect". The effect of electrical discharge machining (EDM) of ASTM C 633 (ASTM International 2001) samples (in subsequent testing for annealing practice) from coated plates could also affect the testing, although this latter effect was assumed to be minimal here due to the lack of observed change in the microstructure near the EDM machined edge. In addition, for this program, the effect of cold spraying onto substrates of different sizes was difficult to quantify. The differences in the size of substrates as well as the substrate fixtures (i.e., plate attached to magnets versus thin or thick disks affixed to steel fixtures attached to magnets) certainly produced different surface temperatures and a corresponding difference in the degree of surface oxidation, along with residual stresses; however, these parameters were not studied systematically. Instead, a greater emphasis was placed on

selection of reproducible substrate effects in latter phases, whereby a consistent thickness of steel and a reproducible surface preparation were defined. Details of these parameters are presented in section 5.

Fully dense coatings were obtained at a range of conditions, since the measured porosity was less than or equal to 0.4 ± 0.6 % for all coatings. Representative cross-sections of the d_{50} = 42 µm powder as-polished coatings cold sprayed with He and N_2 gas displayed fully dense coatings (Figure 10). The top views revealed that significant material jetting was obtained with spray using either gas, although He-sprayed particles appeared to be more highly deformed. While porosity was low for the entire range, the surface roughness increased and hardness decreased with increasing particle velocity. For the d_{50} = 42 µm powder coatings, surface roughness measurements ranged from 6.5 ± 0.7 µm to 9.7 ± 1.4 µm R_a while microhardness values ranged from 57 ± 12 $HV_{0.01}$ to 107 ± 9 $HV_{0.01}$. In comparison, the d_{50} = 23 µm powder coatings displayed lower surface roughness and higher microhardness at respective spray conditions, which was probably due to higher particle velocity during spraying. Lower hardness coatings were also obtained with slower gun traverse speed, as a result of higher substrate temperatures and greater subsequent transfer of this heat into the coating.

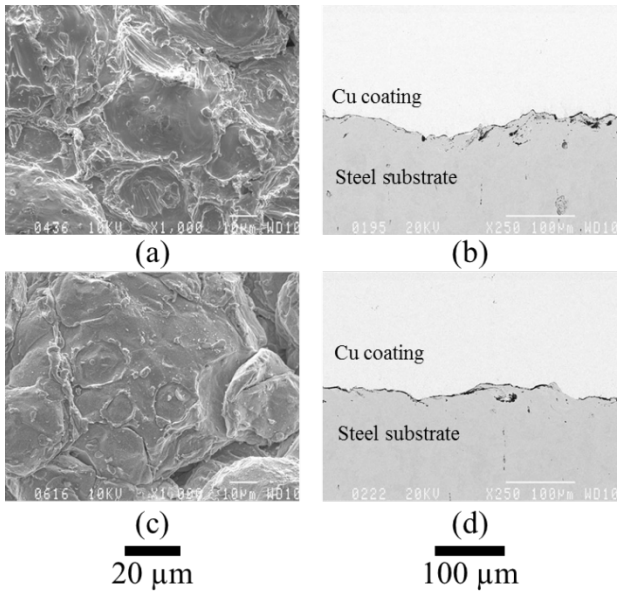


Figure 10: (a) Top view and (b) cross-section of He-sprayed coating and (c) top view and (d) cross-section of N_2-sprayed coating.

Surface topography maps (not shown) over a 10.4 mm × 0.458 mm area obtained for selected coatings using confocal microscopy at 200 × magnification showed profile changes not captured by the surface roughness measurements. The coating made with the spherical, d_{50} = 42 µm powder featured a uniform appearance with well-defined repeating peaks, 150-200 µm high and spaced 1-1.2 mm apart, running parallel to the gun travel direction; this macroscopic surface topography measurement should not be confused with the surface roughness (R_a), which was consistent with previous results (Figure 6 and Figure 9). In comparison, the irregular, d_{50} = 23 µm powder produced a more irregular coating surface with profile changes up to 500 µm. In principle, both surface roughness and waviness may be improved by spray pattern optimization

for a specific set of spray conditions, including powder characteristics. For this application, however, the decision was made to machine the coating surface to eliminate surface irregularities because future UFCs will require suitably smooth surfaces to allow for non-destructive examination.

Overall, the capability of cold spray to produce fully dense copper coatings using a wide range of spray parameters was demonstrated by the DOE runs (measured porosity was less than or equal to 0.4 ± 0.6 % for all coatings). For a relatively low strength, ductile metal such as copper, the window of deposition of ~ 400-1100 m/s (Schmidt et al. 2009) is well within the capability of cold spray equipment. The average particle velocity measured for 13 different spraying conditions (powder with d_{50} = 42 µm) ranged from 570 m/s to 750 m/s, as shown in Figure 8, with optimized conditions at the upper end of the measured range. In comparison, average particle velocities measured for the various powders during the powder selection stage ranged from 480 m/s to 820 m/s. The effects of the spray parameters are typically linked to particle impact velocity, particle temperature, and substrate temperature due to their influence on particle deformation. Coatings with greater degrees of particle deformation are typically associated with minimal porosity, high amounts of bonded area, and relatively high values of cohesive strength (Assadi et al. 2011).

4.2 GENERAL REPAIR OF DAMAGED COATINGS

In a preliminary attempt to evaluate the feasibility of damage repair, the deposition of repair coatings into small V-notch scratches machined into previously coated plates was also investigated. The as-polished repair interface for a N_2-sprayed, d_{50} = 23 µm-powder coating, shown in Figure 11 with a 600 µm scratch, was at times difficult to distinguish outside of the scratched areas. The volume was filled at the bottom of the scratch; however, vertically elongated porosity was obtained near the upper edges of the original scratch. Although no delamination was observed between the repair and coating within most scratches, entrapped alumina particles (identified via EDX) from the grit blasting blocked the repair at the bottom of the scratch volume for one specimen. Etched cross-sections revealed that the microstructure of the repair coating was similar to that of the original coating, and microhardness measurements obtained within the coating and repair regions were generally similar. In order to avoid porosity formation near scratch edges, blending of the scratched and undamaged areas (i.e., grinding/machining a smooth surface and eliminating sharp edges in the geometry), which is a common practice in other thermal spray methods, may be employed. Blending may also reduce or prevent the entrapment of alumina after grit blasting.

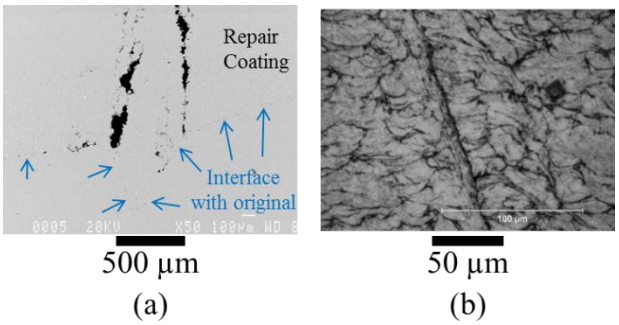


Figure 11: (a) As-polished and (b) etched cross-sections of coating repair of a 600 µm deep V-notch scratch (identical spray conditions for repair and base coatings).

4.3 GENERAL SELECTION OF ANNEALING CONDITIONS

For initial investigation of post-spray annealing, 3 mm thick coatings were produced on low carbon steel plate substrates (165 mm × 140 mm × 3 mm), shown in Figure 2b, using He-spray or N_2-spray (i.e., each coating produced entirely using one gas only). The spray conditions and selected as-sprayed coating characterization data are summarized in Table 8 (G19-21) of Appendix A.1. The higher bond strengths achieved with these samples compared to the previous section is attributed to different substrate dimensions. For brevity, only results with N_2-sprayed, d_{50} = 23 µm powder coatings will be presented in this section. Results for other coatings sprayed entirely with either He or N_2 process gas and using d_{50} = 42 µm powder (i.e., powder used in section 4.1) can be found in Appendix A.3.[1] A range of annealing conditions based on the temperatures of stress relieving and annealing of pure wrought copper was screened through microhardness and microstructural characterization. Annealing temperatures of 200 °C, 300 °C, 400 °C, 500 °C, and 600 °C for 1 h and 10 h were investigated, as well as one long-term, low temperature anneal at 200 °C for 100 h. Two optimized conditions were then selected for subsequent characterization by ASTM E 8 (ASTM International 2009b) tensile testing, ASTM C 633 (ASTM International 2001) bond testing, and ASTM E 290 (ASTM International 2009a) bend testing. Coatings were machined to eliminate surface irregularities for bend and bond testing (0.8-1.1 mm removed) and to produce 1 mm thick coating-only specimens for tensile testing. Selected characterization data for annealed coatings are summarized in Table 3.

Table 3: Selected characterization results for N_2-sprayed coatings annealed for 1 h at 300 °C and 600 °C.

Label	T_{anneal}	t_{anneal}	$HV_{0.01}$	Bond Strength	Tensile Strength	Failure Strain	Bend Angle
	°C	h		MPa	MPa	%	
G19-21	As-Spray		81 ± 5	67 ± 7*	370 ± 33	0.5 ± 0.2	5 ± 1
G19-21	300	1	52 ± 4	66 ± 6*	245 ± 4	16.3 ± 3.2	52 ± 14
G19-21	600	1	36 ± 3	64 ± 5*	180 ± 2	34.5 ± 2.7	No crack

Label = coating, T_{anneal} = anneal temperature, t_{anneal} = anneal time, Bend Angle = angle at first observed crack

* Epoxy failure (not interface failure)

[1] Appendix A.3 presents test results to investigate differences in annealing behaviour between coatings presented in this section (4.3), i.e., N_2-spray using d_{50} = 23 µm, with (i) He-spray using d_{50} = 42 µm powder (Appendix A.3.1) and (ii) N_2-spray using d_{50} = 42 µm (Appendix A.3.2). Overall, the comparison of N_2-sprayed and He-sprayed coatings produced in the general coating development (section 4) revealed that better mechanical properties coatings can be obtained when using higher gas temperature and pressure with N_2-spray (T_g = 800 °C and P_g = 5 MPa) compared to lower conditions with He-spray (T_g = 350 °C and P_g = 3.5 MPa). This does not account for the effect of any differences in particle velocity, which was not measured for He-spray. The comparison of the two powders indicated that coatings with relatively similar mechanical properties can be produced with the two different powders, which was consistent with results from the powder selection testing phase (section 3.2)

Based on the hardness measurements and microstructure analysis of the micrograph coupons in screening tests, the following two optimized annealing conditions were identified: 1 h at 300 °C and 1 h at 600 °C. The first condition featured a relatively low temperature that produced a significant decrease in hardness from the as-sprayed condition, as well as no apparent increase in porosity, as shown in Figure 12 and Figure 13e, respectively. The second condition employed a relatively high temperature that produced microstructural restoration (i.e., recrystallization) in the annealed coating (Figure 13f). The 1 h anneal time was selected due to the minimal hardness difference obtained between 1 and 10 h (Figure 12).

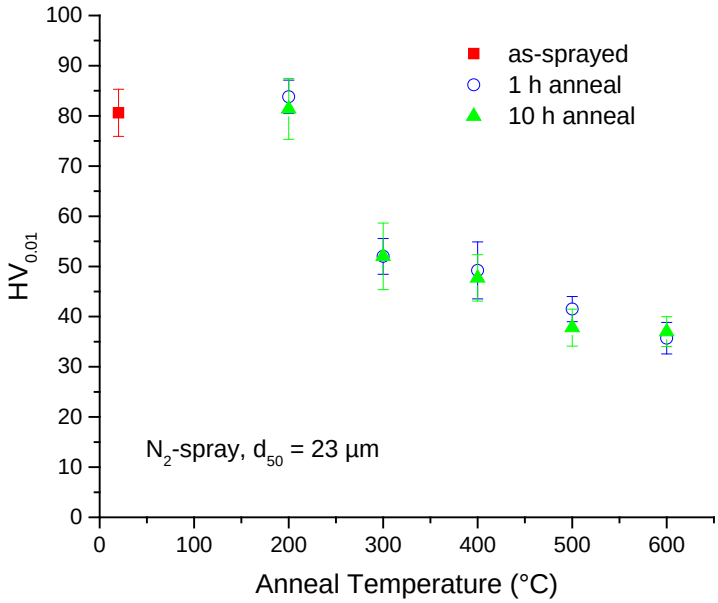


Figure 12: Microhardness as a function of anneal temperature for N_2-sprayed coatings (d_{50} = 23 µm powder).

Bond strength was high for coatings in both as-sprayed and annealed conditions. Samples generally failed in the epoxy (used to attach the pull test studs in ASTM C 633 (ASTM International 2001), which indicated bond strength was, at minimum, equal to the epoxy strength of 60-70 MPa. Representative stress-strain curves for coatings in the as-sprayed and annealed conditions, shown in Figure 14, revealed that annealing decreased coating strength and increased ductility, with a greater effect obtained at higher temperature. Tensile strength and strain at failure values of 370 ± 33 MPa and 0.5 ± 0.2 %, 245 ± 4 MPa and 16 ± 3 %, and 180 ± 2 MPa and 34 ± 3 % were obtained for as-sprayed, 300 °C annealed, and 600 °C annealed conditions, respectively. These results are consistent with reported values in the literature for cold spray copper coatings (Calla et al. 2006; Gartner et al. 2006). For comparison, the ASTM B 152 (ASTM International 2006) minimum tensile strength is 205 MPa for hot-rolled tempers and 220-360 MPa for cold-rolled tempers, with a minimum 40% elongation for C11000 and C12200 plate with hot-rolled tempers; it is worth noting that such high value is unlikely to be utilized as a minimum requirement for UFCs. Typical bend test specimens, shown in Figure 15, produced a crack through the entire coating within a 5 ± 1° bend for the as-sprayed condition; a first edge crack after a 52 ± 14° bend, and 90° bend without a crack propagating through the

entire coating thickness after heat treatment at 300 °C; and no visible cracks after a full bend (146°) in samples annealed at 600 °C.

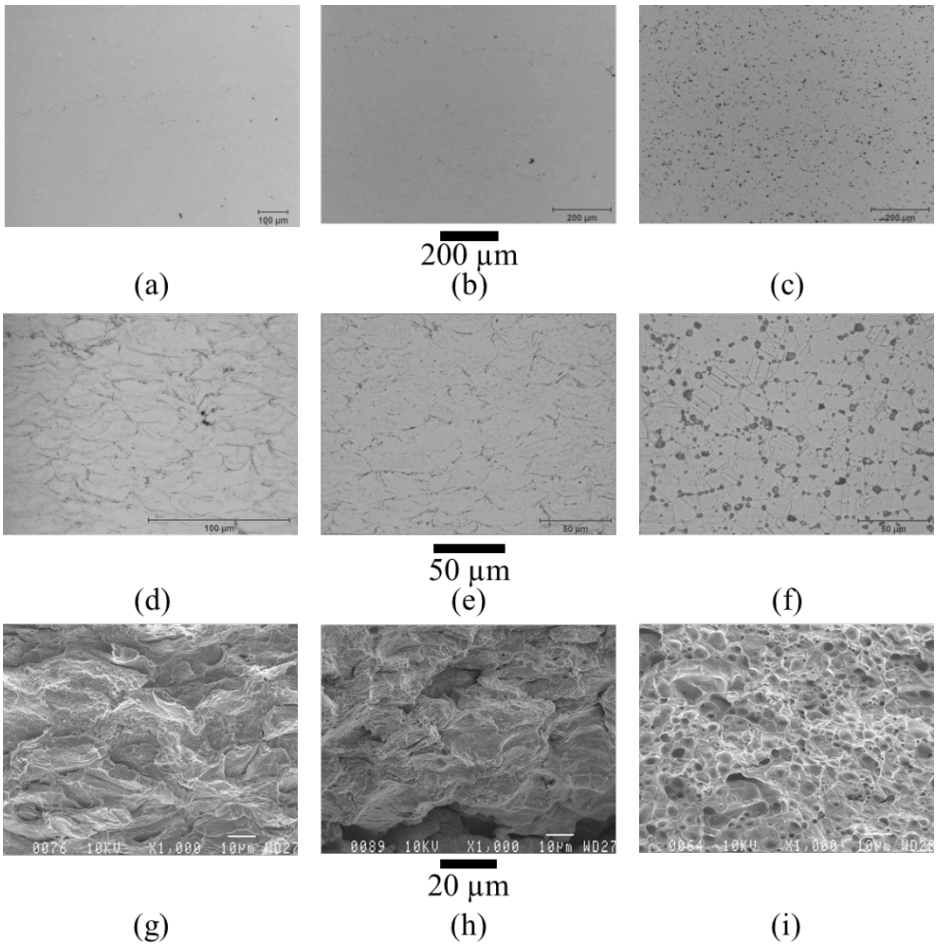


Figure 13: Selected results for N_2-sprayed coatings (d_{50} = 23 µm powder) after annealing at various temperatures (polished cross-sections obtained): (a) as-sprayed, (b) after 300 °C/1 h anneal, and (c) after 600 °C/1 h anneal (etched microstructures obtained) (d) as-sprayed, (e) after 300 °C/1 h anneal, and (f) after 600 °C/1 h anneal; and fracture surfaces of tensile specimens (g) as-sprayed, (h) after 300 °C/1 h anneal, and (i) after 600 °C/1 h anneal.

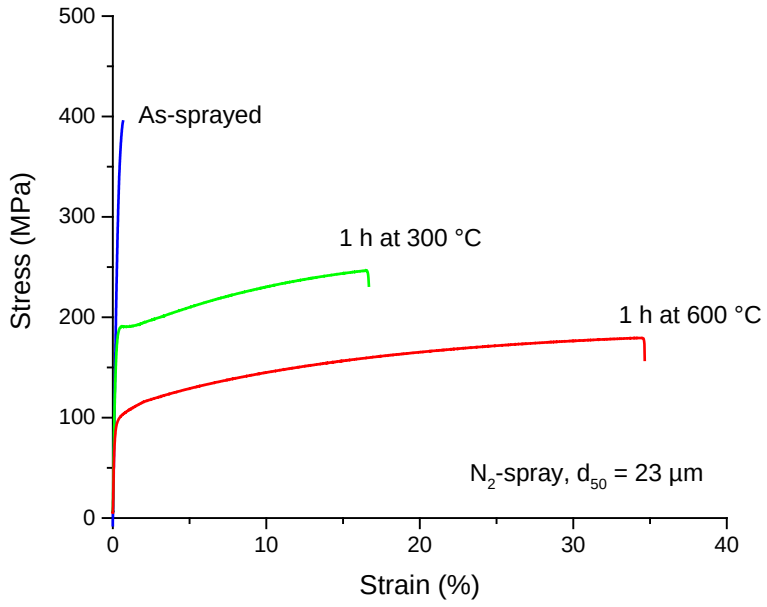


Figure 14: Representative stress-strain curves for N_2-sprayed coatings after annealing (d_{50} = 23 µm powder).

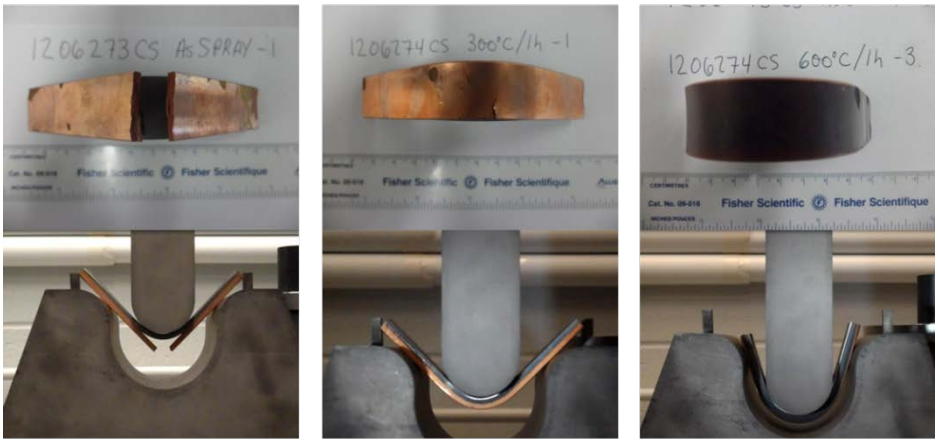


Figure 15: Photos of bend test specimens for N_2-sprayed coatings (d_{50} = 23 µm powder) after annealing (a) As-sprayed coating (b) coating after heat treatment 1h@300°C, coating after heat treatment 1h@600°C.

The coatings in as-sprayed condition displayed a relatively smooth fracture surface and clearly delineated particle boundaries (Figure 13d). In contrast, a dimpled fracture surface without discernable particle boundaries was observed in coatings annealed at 600 °C (Figure 13f). From these results, it may be interpreted that fracture was associated with particle de-bonding (e.g., the as-sprayed condition) and the improvement in ductility after annealing was potentially due to better inter-particle bonding (e.g., the 600 °C heat treatment) (Calla et al. 2006; Gartner et al. 2006). Heat treatment at 300 °C represented a transition between these conditions (Figure 13e), so only moderate ductility improvements were observed. The increase in the number and size of metallurgically bonded inter-particle interfaces is diffusion related (Gartner et al. 2006). Diffusivity was increased with an increase in annealing temperature, due to the temperature-dependence of the copper self-diffusion coefficient values, which are on the order of 10^{-18} and 10^{-13} cm^2/s at 300 °C and 600 °C, respectively (Maier 1977). These temperatures represent ~ 45% and 64% of the melting point (absolute values), respectively. The reduction in non-metallurgical bonding reduces the potential number of sites for crack initiation, as these inter-particle interfaces may represent crack centres larger than critical size (Gartner et al. 2006). Another factor that may have affected the strength and ductility after annealing is the degree of recovery, recrystallization, and grain growth. Although particle boundaries were clearly observed in the micrographs, grain boundaries could only be discerned in specimens annealed at 600°C. After annealing 600°C for 1 h, grain boundaries and inter-particle boundaries appeared similar in the N_2-sprayed, d_{50} = 23 µm-powder specimens, and the microstructure appeared to be fully recrystallized. Recrystallization was not observed at 300°C, although the microstructure was likely to be partially recrystallized at 300°C, as Stoltenhoff et al. reported the appearance of recrystallized grains after annealing cold sprayed copper coatings at 200°C for 1 h (Stoltenhoff et al. 2006).

In this work, the effect of the increase in porosity observed in coatings annealed at 600°C (c.f., Figure 13c) was not evaluated. Calla et al. (Calla et al. 2006) also obtained an increase in apparent porosity located at inter-particle boundaries in cold sprayed coatings annealed at 600°C for 1 h. This increase was cited as a potential source of the lower ductility obtained for annealed coatings relative to annealed bulk sheet, and attributed to a possible relaxation of compressive residual stresses or the expansion and spheroidization of driving gas entrapped within the cold spray structure. Stoltenhoff et al. (Stoltenhoff et al. 2006) observed the development of spheroidized oxides in coatings annealed at 600°C for 1 h, which were located at former inter-particle boundaries in N_2-sprayed coatings and randomly distributed in He-sprayed coatings. Another potential cause of the increase in observed porosity is the spheroidization of pores through a mechanism analogous to sintering, which has been reported for other cold sprayed material (Wong et al. 2013). In that case, the increase in apparent porosity would result from a reorganisation of the initial planar defects (inter-particle boundaries) into spherical and thus more visible pores, and not from an actual increase in porosity. In general, the effects of porosity are dependent on the number, size, and morphology of the pores. Pores can act as defects which raise stress concentrations and, although no porosity – strength relationships are available for cold sprayed copper, Hyun et al. (Hyun, Murakami and Nakajima 2001) showed tensile strengths of ~ 150 MPa can still be obtained with as much as 2-3 % porosity for copper castings. To date, no specification on allowable porosity has been defined for the UFC application.

4.4 GENERAL MICROSTRUCTURAL CHARACTERIZATION BY EBSD

The characterization of coating microstructures using electron backscatter diffraction (EBSD) was performed by Western University, Dept. of Chemistry (London, ON). This section includes selected EBSD results reported elsewhere (Jakupi et al. 2015). Three samples produced by NRC for the corrosion testing program (described in Appendix A.4), referred to as EBSD300, EBSD600, and EBSD800 hereafter (number representing the cold spray gas temperature), were analyzed using EBSD. The EBSD300 sample was produced in the preliminary stages of the program (before testing described previously in section 3, while the EBSD600 and EBSD800 samples were produced during UFC optimization (parallel to testing described subsequently in section 5). The processing of these coatings differs significantly in terms of cold spray system, powder, and spray conditions, as shown in Table 4. Consequently, caution is advised when directly comparing EBSD results between the coatings.

Table 4: Spray conditions employed for EBSD samples.

Conditions*	**EBSD300**	**EBSD600**	**EBSD800**
	He-spray	**He- and N_2-spray**	**He- and N_2-spray**
System	Kinetiks 4000	PCS-800	PCS-1000
Powder, d_{50} (µm)	12.5	42	42
Substrate	Mild steel plate 12.7 x 15.256 x 0.64 cm	A36 steel rod 9.5 mm Ø	A36 steel rod 9.5 mm Ø
Gas temp., T_g (°C)	300	600	800
Gas pressure, P_g (MPa)	4	5	5
Traverse speed (mm/s)	300	3.7†	1†
Step size (mm)	1.25	-†	-†
Substrate rotation (rpm)	n/a	223†	60†
Standoff distance (mm)	80	30	30

* Specific spray conditions for each stage are shown in Appendix A.1. Corrosion sample production is described in Appendix A.4

† EBSD600 and EBSD800 were produced on a rotating substrate holder (15.25cm Ø). The equivalent traverse speed and step size for spray on a stationary flat are 2000 mm/s traverse speed and 1 mm step for EBSD600 and 500 mm/s traverse speed and 1 mm step for EBSD800.

An EBSD map of a particle of the d_{50} = 12.5 µm powder, shown in Figure 16, reveals an equiaxed microstructure. The d_{50} = 42 µm powder was not analyzed by EBSD, although etched samples obtained during powder selection testing (section 0) revealed an equiaxed microstructure with substantially larger grains (cf. Figure 4b). The d_{50} = 12.5 µm powder was not part of powder selection testing. SEM images of both powders, shown in Figure 17, demonstrate the size difference of the particles.

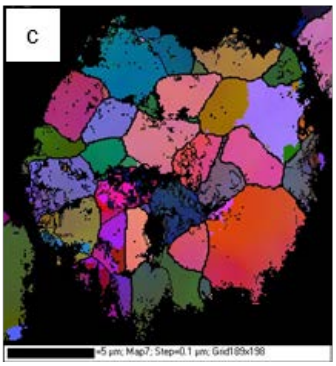


Figure 16: Euler contrast EBSD map of d_{50} = 12.5 µm powder. Source: (Jakupi et al. 2015).

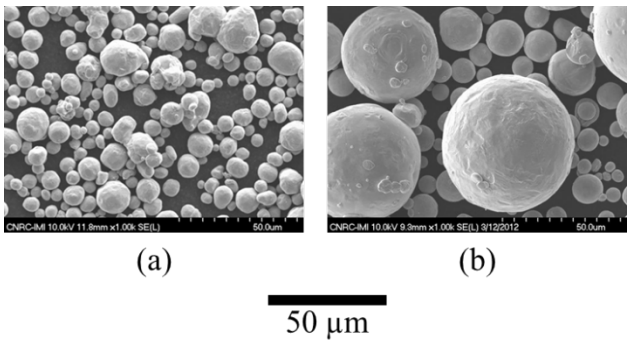


Figure 17: Feedstock powder morphologies: (a) supplier 6, d_{50} = 12.5 µm; (b) supplier 1, d_{50} = 42 µm.

SEM micrographs and corresponding EBSD maps for as-sprayed coatings near the coating-substrate interface (i.e., in the He-sprayed bond coat) are shown in Figure 18. The microstructure of the EBSD300 coating (a, b) clearly displays a highly deformed structure (note that the magnification is lower than that used in Figure 16). The EBSD600 coating (c, d) has an inhomogeneous microstructure with various morphologies observed: very fine and equiaxed; fine and pancaked; and fine and equiaxed. The EBSD800 coating (e, f) displays a relatively equiaxed, bimodal microstructure with a fine structure at the particle interfaces and a coarser particle interior. An analysis of microstructure development during cold spray through EBSD results is reported elsewhere (Jakupi et al. 2015).

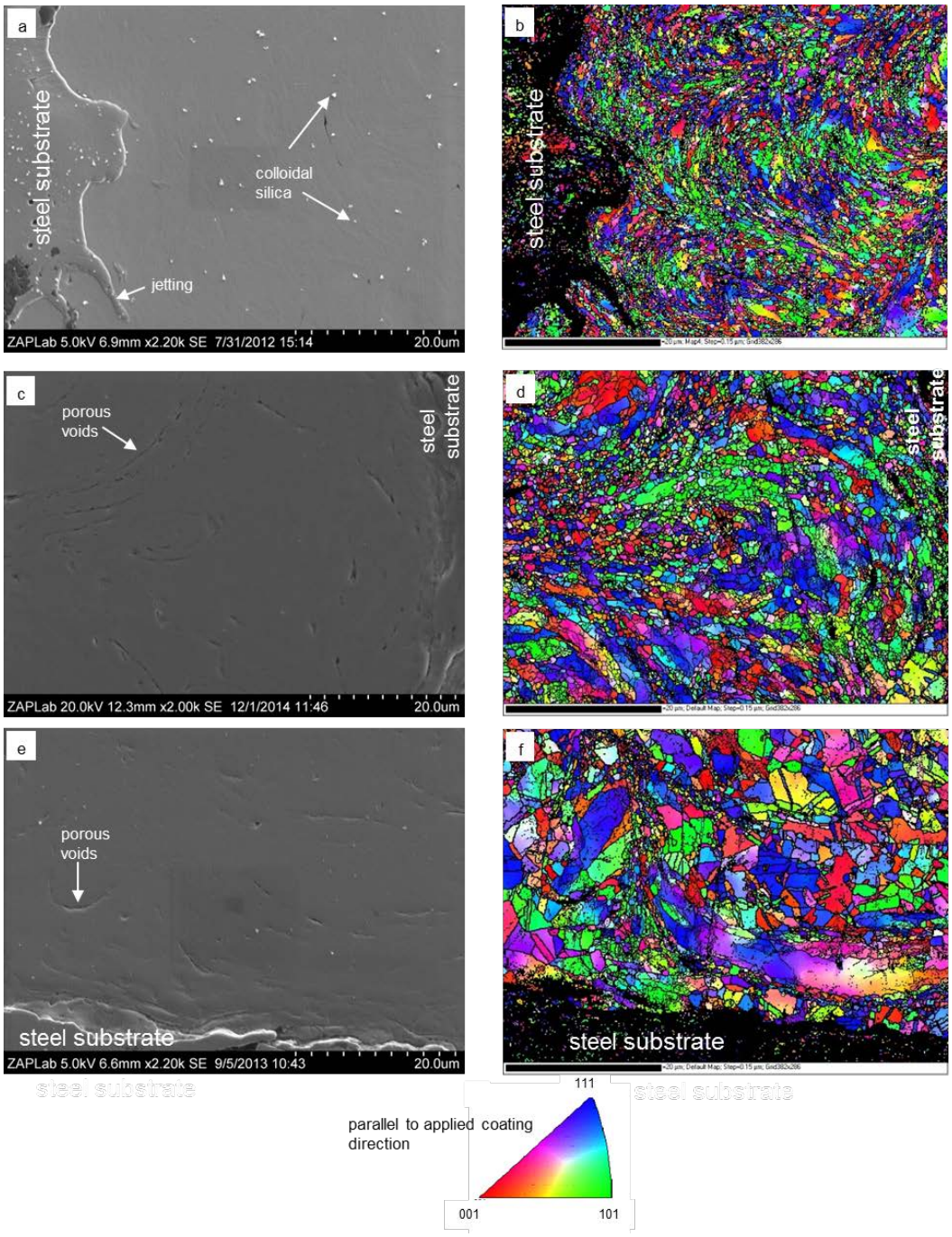


Figure 18: Electron micrographs and corresponding EBSD IPF maps recorded at the Cu-coating/steel interface: (a) and (b) cold sprayed at 300°C (3 MPa): (c) and (d) cold sprayed at 600°C (5 MPa): (e) and (f) cold sprayed at 800°C (5 MPa). The indexing rates were 68%, 84% and 86% for (b), (d) and (f), respectively. Source: (Jakupi et al. 2015).

EBSD maps for as-sprayed EBSD600 and EBSD800 coatings at the interface between the He-sprayed bond coat and N_2-sprayed top coat are shown in Figure 19. The investigators (Jakupi et al. 2015) reported no significant differences in grain size, or bonding quality for the bulk

coating layers compared to the copper/steel interfaces. However, there do appear to be some differences in crystallite size observed in (a) between the left and right sides and in (c) between the top and bottom. EBSD results of EBSD600 and EBSD800 coatings heat treated at 400 °C for 4 h, shown Figure 20, revealed the formation of relatively homogeneous, equiaxed microstructures.

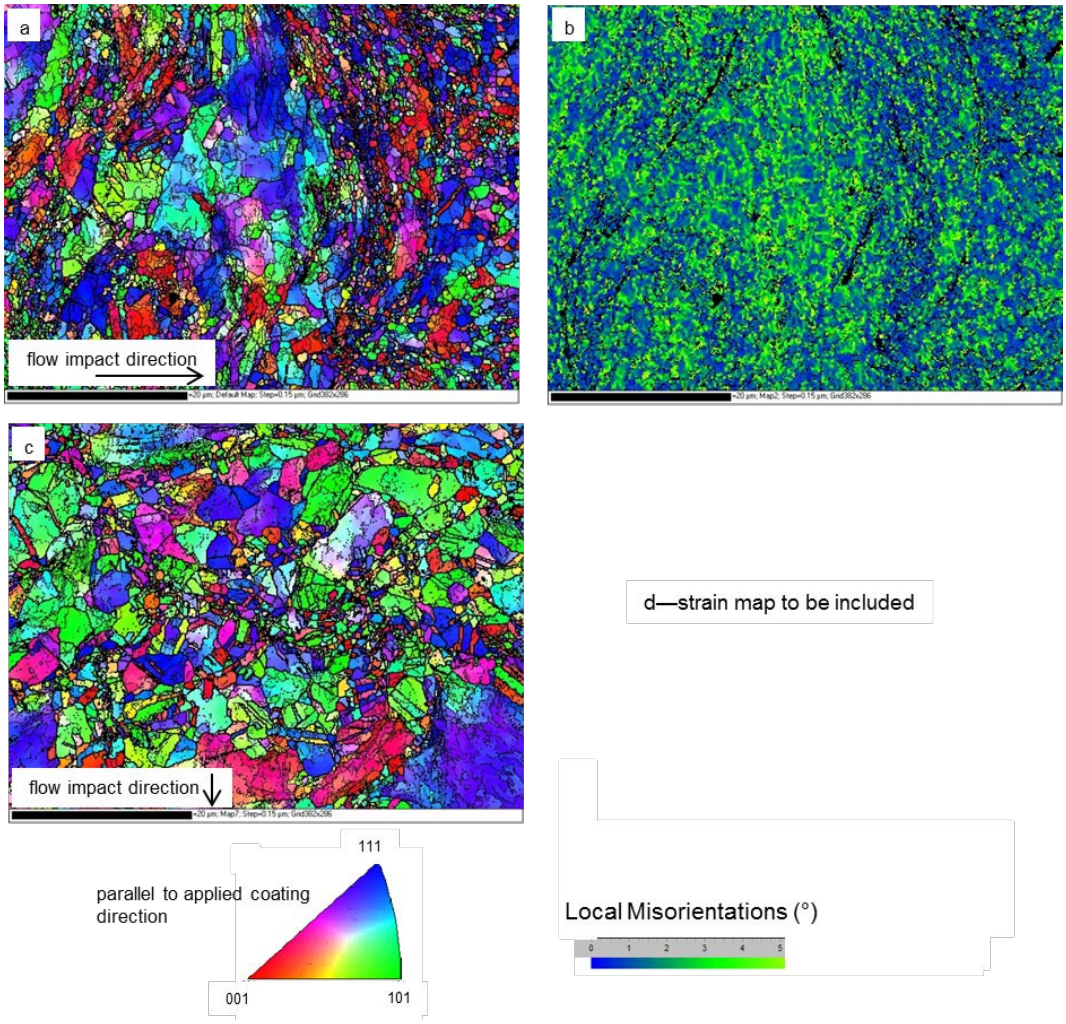


Figure 19: EBSD IPF maps and corresponding strain maps produced for regions where the cold spray carrier gas was switched from He to N_2 for spray conditions of (a, b) 600°C (5 MPa) and (c,d) 800°C (5 MPa): the indexing rates were 85 % and 83 %, respectively. Source: (Jakupi et al. 2015).

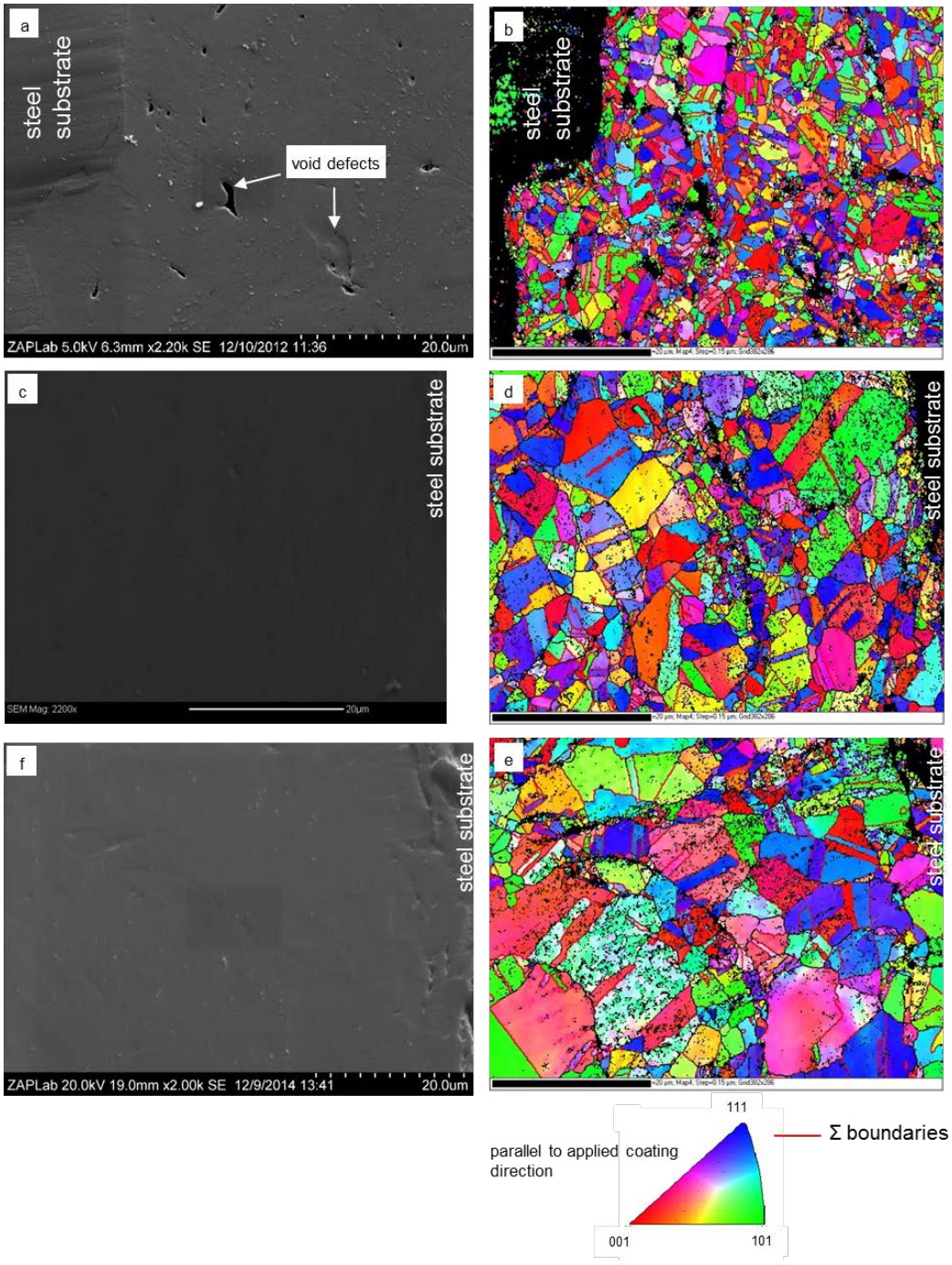


Figure 20: EBSD IPF maps and corresponding SE micrographs of post-annealed (4 h, 400°C) Cu coatings formed with cold spray conditions (a, b) 300°C (3 MPa), (c, d) 600°C (5 MPa) and (e, f) 800°C (5 MPa); the indexing rates were 83 %, 87 %, and 89 %, respectively. Source: (Jakupi et al. 2015).

5. USED FUEL CONTAINER COATING OPTIMIZATION

Based on the general coating development presented in the previous sections, parallel coating feasibility studies (not included in this report), and UFC container requirements, an initial reference cold spray coating system was developed. In order to maximize coating adhesion, a bond coat sprayed with He was selected, followed by a N_2-sprayed top coat to build the required thickness. However, such a process was not sufficiently validated to implement on mock-up containers, since post-deposition heat treatment was only roughly defined at this point in the study. Results from parallel modeling of in-repository container loading conditions, along with results from concurrent cold spray feasibility studies, were used to refine copper coating ductility requirements. Finally, only planar coupons of various steel grades were cold spray coated within the feasibility studies indicated above. Substrate and coating thicknesses were not uniformly defined.

To be considered for UFCs, it was necessary to demonstrate that cold spray coatings can be achieved on materials such as the steel grade of the UFC body, welded steel substrates, larger dimension steel coupons prior to implementing a program dedicated to UFC fabrication. It was also necessary to demonstrate that coatings could be repeatedly produced to a suitable thickness to withstand corrosion processes with a sufficient safety margin; thus a minimum thickness of 3 mm was defined for subsequent work. While 3 mm was defined as the reference coating thickness, coatings of thicknesses up to a nominal 10 mm were also explored, to further verify the flexibility of the cold spray method. In addition, the application of cold spray coatings to cast iron substrates was investigated to assess the technology application other international disposal canister designs (SKB/Posiva)

5.1 VALIDATION OF REFERENCE COATING ON PLANAR SUBSTRATES

The initial reference cold spray coating system was defined with the following parameters:

- 10-70 µm spherical low oxygen copper powder;
- 25.4 mm min. thick A516 grade 70 steel, grit blasted with 24 grit to remove mill scale;
- ~100 µm bond coat, applied with He-spray at 5 MPa and 800 °C; and
- 3 mm min. thick top coat, applied with N_2-spray at 5 MPa and 800 °C.

Based on powder availability and reference powder criteria, the d_{50} = 42 µm powder from supplier 1 used previously for general coating development was selected for validation testing, and two new powder lots were obtained. To maintain continuity and avoid confusion, the powder will be generically referred to as d_{50} = 42 µm powder (with lots A, B, or C, when applicable). The original lot (A) and two new lots (B and C) were similar in size distribution (d_{50} = 42 µm, 48 µm, and 43 µm, respectively) and all three lots displayed a dense, spherical morphology with particle surfaces free of satellites.

Initial validation trials were performed using the Plasma Giken PCS-1000 unit and powder lot B, and involved coatings produced on the flat surfaces of cylinders (25.4 mm Ø × 38.1 mm) held in a rotating substrate holder (15 cm Ø), shown in Figure 2c. The spray conditions and coating characterization data are summarized in Appendix A.1. The A36 steel substrates, which are compositionally similar to the reference A516 grade 70, did not significantly affect the coating density or bond strength (detailed later). The first spray trial using initial reference parameters produced a visually uniform coating surface, and ASTM C 633 (ASTM International 2001) bond

strength testing resulted in epoxy failure (i.e., min. 60-70 MPa). The coating microstructure, shown in Figure 21a, consisted of a dense ~ 340 µm thick bond coat produced by He-spray and an additional ~ 3 mm subsequently deposited by N_2-spray with coating porosity measured at 0.1 ± 0.1%.

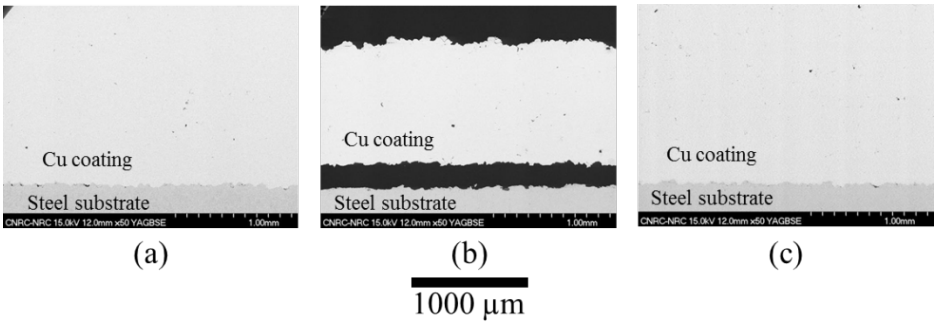


Figure 21: As-polished coatings (d_{50} = 42 µm powder on A36 substrate) produced during UFC process optimization using: (a) initial reference parameters with T_g = 800 °C; (b) parameters similar to those in (a) but without He bond coat, with doubled gun traverse speed, and with doubled substrate rotation speed; and (c) optimized reference parameters with T_g = 600 °C.

Subsequent trials were performed to briefly investigate: (i) coating-substrate adhesion without a He-sprayed bond coat and (ii) the sensitivity of coating porosity to changes in spray conditions. The gun traverse speed and substrate rotation speed were investigated due to their influence on the substrate surface temperature and deposition profile. The powder feed rate was considered for its potential effect on particle loading and deposition profile. These three spray parameters were also investigated to accommodate the practical aspects of spraying the large diameter UFC that will be detailed later in Section 6 under prototyping. For comparable coatings produced without a He-sprayed bond coat, debonding occurred before a full 3 mm thickness was deposited. However, qualitative observations using optical microscopy revealed coating microstructures to be similar, and porosity measurement of a representative coating showed no increase due to the changes in spray conditions. A representative debonded coating, which was produced without a He-sprayed bond coat, with substrate rotation doubled, and with gun traverse speed doubled, (0.1 ± 0.2 % in ~ 3 mm top coat) is shown in Figure 21b.

An attempt to spray with powder lot C using initial reference conditions resulted in clogging issues, which were not obtained with powder lots A or B. A difference in oxygen content for lot C and/or a higher amount of fines may have been significant. A change in gas temperature (from 800 °C to 600 °C) and spray unit (from PCS-1000 to PCS-800) from the initial reference was employed to resolve the clogging. Coatings produced using the lower gas temperature (A8 coating in Appendix A.1), shown in Figure 21c, were dense and achieved comparable bond strength minima to the previous materials. As the lower temperature parameters were necessary to avoid clogging with one of the two powder lots used, the reference coating condition was modified to allow for a gas temperature of 600 °C for this lot.

A secondary validation through four production runs using larger scale substrates was performed using the Plasma Giken PCS-800 unit and powder lot C (R1-R4 coatings in Appendix A.1). Each production run involved depositing 3 mm thick coatings on plate substrates (A516 grade 70, 150 mm x 150 mm x 38 mm) fixed into a rotating 560 mm Ø sample holder which also

allowed disk substrates (25.4 mm Ø x 38.1 mm) to be simultaneously coated, as shown in Figure 2d. For the 3.7 mm thick coating, shown in Figure 22a, surface machining removed ~ 1 mm, and the machined coating was 2.69 ± 0.01 mm thick, as shown in Figure 22g. The requirements for machining, if any, have not been strictly designated within the NWMO coating program; this parameter will have input from multiple fronts, which are being researched concurrently.

In addition to nominally 3 mm thick coatings, nominally 5 mm thick (6.12 ± 0.13 mm, as-sprayed) and 10 mm (9.58 ± 0.14 mm, as-sprayed) coatings were also produced, as per Figure 22b/e, and c/f, top and side views, respectively. For these thicker coatings, the surface of coatings deposited during a previous day was grit blasted (24 grit alumina using 0.14 MPa) immediately prior to the next spraying run. This minor experimental alteration allowed for multiple thicknesses of coatings to be produced over a series of runs, as some plates were removed after each 3 mm coating step for adhesion, annealing, etc. The macro appearance of coatings on larger scale plates was similar to that of the 3 mm thick coatings.

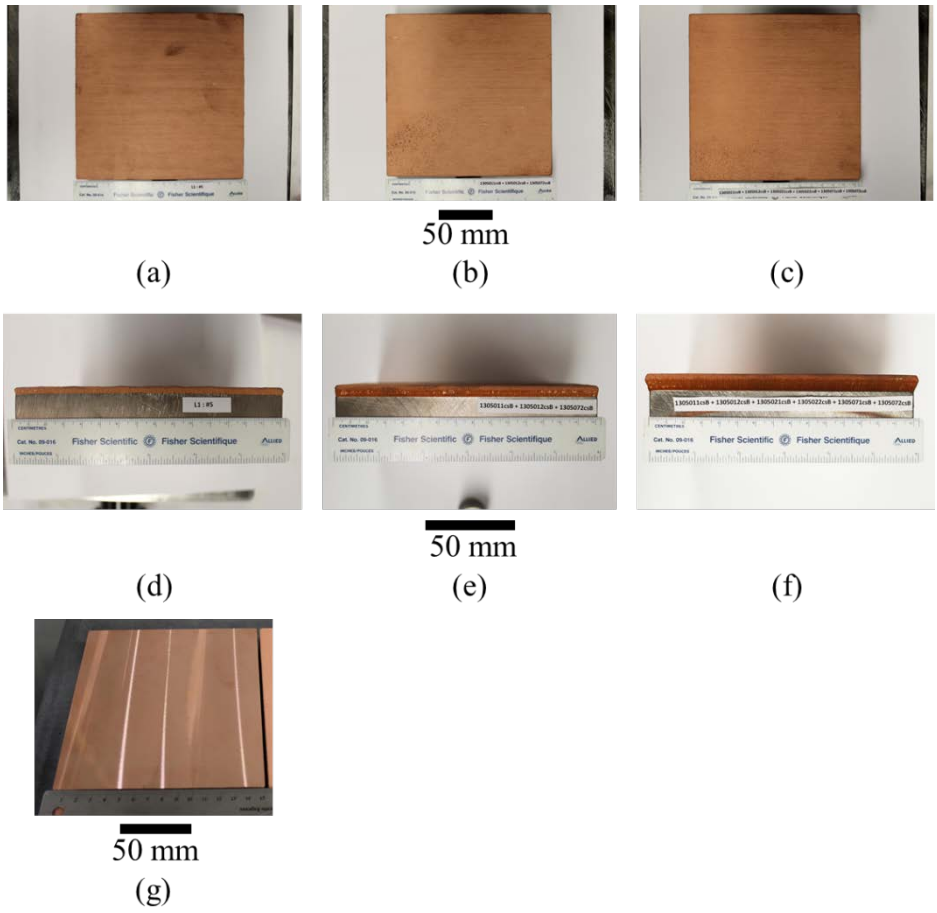


Figure 22: Photos of coatings prepared at various thicknesses (d_{50} = 42 µm powder) produced during UFC process optimization: As-sprayed coating top views for (a) 3.7 mm (b) 6.1 mm (c) 9.6 mm; As-sprayed coating side views for (d) 3.7 mm (e) 6.1 mm and (f) 9.6 mm; (g) As-machined coating top view for 2.7 mm (white streaks are artefacts due to reflections.

Two plates with 3 mm thick coatings were arbitrarily selected as representative coatings for characterization. During one production run, A36 disks were simultaneously coated to produce specimens for immediate analysis (i.e., to avoid machining delay) and confirm that spraying on A36 or A516 grade 70, which have similar compositions, would not change coating properties. This latter equivalency demonstration is particularly important in that the nearest composition to A516 grade 70 plate in a rod form is A36. Coating porosity was measured at 0.5 ± 0.4 % and 0.3 ± 0.2 % for the plate and disk samples, respectively, from the same run, as shown in Figure 23a and Figure 23b, respectively. The other coated plate specimen (not shown) appeared completely dense, with porosity measured at 0.0 ± 0.1 %. The coating/substrate interfaces were also similar and all bond strength tests resulted in epoxy failure (i.e., min. 60-70 MPa) instead of failure at the coating/substrate interface. Due to the similarity in coating density, coating interface, and bond strength results, the effect of different substrates (A516 and A36) was considered minimal.

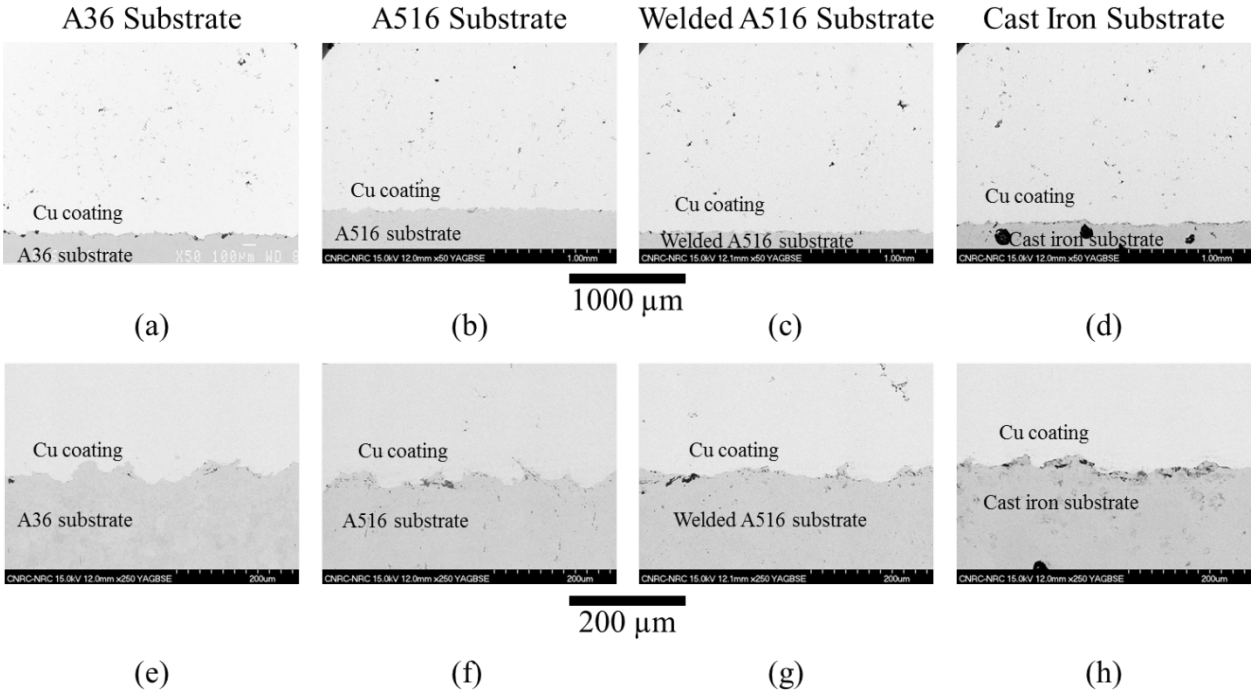


Figure 23: As-polished coatings (d_{50} = 42 µm powder) produced during UFC process optimization using optimized reference parameters with T_g = 600 °C on different substrates: (a, e) A36 substrate, (b, f) A516 grade 70 substrate, (c, g) welded A516 grade 70 substrate, and (d, h) cast iron substrate.

Bond strength measurement using a ASTM E 8 (ASTM International 2011) tensile test with deviation of geometry on small scale specimens (5.90 mm gage length × 20 mm^2 area cross-section) was performed by an external contractor (Exova, Cambridge, ON) on the 10 mm thick cold spray coating on A516 plate (Figure 24). All failures were reported to occur at the coating-substrate interface, with no measurable elongation and with a bond strength of 83 ± 15 MPa. The bond strength was consistent with the ASTM C 633 (ASTM International 2001) results,

which showed epoxy failures at > 60 MPa for 3 mm thick coatings on A516 plate. Although coating thickness can impact bond strength (e.g., via coating residual stress), the effect of coating thickness on bond strength was not investigated in this work. Reported results for cold spray of copper (≤1900 µm thick) onto steel Almen strips showed an increase in measured distortion (due to residual stresses) with increasing coating thickness (Arabgol et al. 2014). However, modelling also showed that beyond a maximum thickness value, residual stress decreased with decreasing coating thickness (e.g., residual stress within a 10 mm thick coating was predicted to be ~1/3 that of a 3 mm thick coating) (Arabgol et al. 2014). This trend is consistent with reported results for bond strength testing of a cold sprayed aluminum alloy on aluminum alloy substrate, which showed decreasing tensile bond strength with increasing coating thickness up to 2.9 mm thick followed by a higher bond strength at 3.7 mm thick (Xiong, Zhuang and Zhang 2015).



Figure 24: Test jig used by Exova with a representative test specimen inserted. The white dots on the test specimen are reference marks for elongation measurement.

5.2 APPLICATION OF REFERENCE COATING TO WELD SAMPLES

The application of reference coatings on the weld area of A516 grade 70 substrates involved the same setup as the validation using A36 cylinders (cf., Figure 2c, d). The spray conditions and coating characterization data are summarized in Appendix A.1. A cross-section of the as-received welded steel substrate, shown in Figure 25, confirmed that the weld surface was much larger (~ 35 mm wide) than the 25.4 mm diameter rod specimens machined from the weld area. Overall, the coatings produced on weld substrates under the conditions investigated were comparable in bond strength and coating density to the coatings produced during the reference parameter validation (e.g., epoxy failure in ASTM C 633 (ASTM International 2001) bond strength test and < 0.3 % porosity at T_g = 600 °C, shown in Figure 23c, using a He-sprayed bond coat with N_2-sprayed top coat).

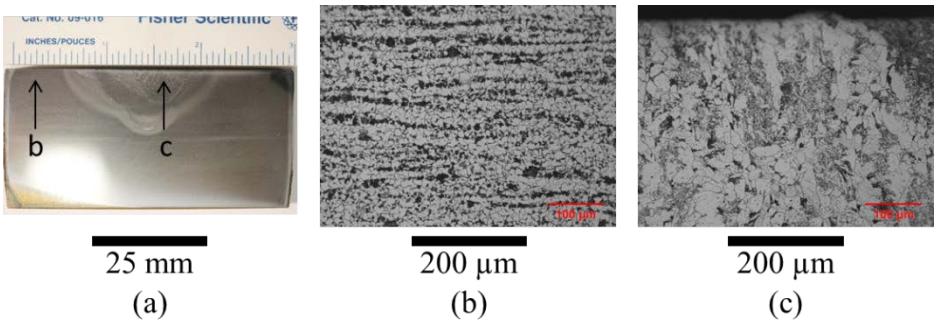


Figure 25: As-received welded A516 grade 70 steel substrate: (a) photo of cross-section showing approximate locations of optical micrographs; and optical micrographs of (b) base metal and (c) centre of the weld.

5.3 APPLICATION OF REFERENCE COATING TO CAST IRON SUBSTRATES

The application of reference coatings on cast iron substrates was produced with the same procedure as used for the weld substrate samples. The spray conditions and coating characterization data are summarized in Appendix A.1. In general, coatings on cast iron displayed low porosity (0.4 ± 0.5%), shown in Figure 23d, which was similar to the reference A516 grade 70 (or A36) steel. However, bond testing produced adhesive failure at the coating-substrate interface with a measured strength of 37 ± 12 MPa, which was significantly below the epoxy failures at ~ 60-70 MPa for A516 (or A36) reference substrates. The relatively large standard deviation was due to one outlier at 14 MPa (i.e., 41 ± 3 MPa for the other 4 replicates).

The root cause of the lower bond strength on the cast iron substrate was not clear, although differences were observed with coatings on reference substrates. The higher magnification SEM micrographs in Figure 23 reveal that the coating-substrate interface was generally more uniform (i.e., flat) on the cast iron substrate (Figure 23d) compared to the A36 (Figure 23a) and A516 (Figure 23b) substrates. The coating on the cast iron substrate appears more similar to the welded A516 substrate (Figure 23c). A quantitative analysis of the interfaces is necessary to verify these comparisons. However, coatings on the A36 substrate qualitatively displayed more closely spaced peaks along the interface and a higher peak-to-trough distance, which suggest that deformation of the particle and/or substrate was higher than for the coating on cast iron. A lower degree of deformation may result in lower bond strength (e.g., due to a decrease in mechanical interlocking and/or adiabatic shear instability). An investigation of substrate properties (e.g., thermal and mechanical) and associated effects was not within the scope of the study. Indirect testing of relative substrate strengths at room temperature on a limited basis showed fairly similar results, as surface roughness after grit blasting and hardness values (of one of each substrate) were generally near/within the standard deviation. The cast iron and A36 substrates showed R_a values of 5.33 ± 0.50 µm and 5.95 ± 0.57 µm, respectively, and HRA (Rockwell A) numbers of 43.02 ± 1.69 and 46.44 ± 1.63, respectively. Spheroidal (nodular) graphite was distributed throughout the matrix (Figure 23d) with partial nodules observed along machined edges (not shown). However, these relatively large nodules were not observed along the coating-substrate interface, which suggests that nodules were removed during the substrate preparation (i.e., by grit blasting) and/or spray process (i.e., by particle impact). The presence of graphite at the interface (e.g., crushed fragments) may reduce bond strength by decreasing the well-bonded surface area between the copper particles and the matrix of the cast iron.

5.4 OPTIMIZATION OF ANNEALING CONDITIONS

Results from the initial study for general coating development showed that coatings heat treated for 1 h at 300 °C did not quite meet the preliminary ductility requirement (20 % elongation prior to fracture), while coatings heat treated for 1 h at 600 °C displayed small pores not observed in the as-sprayed condition. As a result, a brief optimization of annealing conditions was performed. Planar samples coated with the reference coating system were tested in the as-sprayed condition and after heat treatment for 1 h at 350 °C and 400 °C. All test specimens were produced from 3 mm thick coatings (on A516 grade 70 substrate) except those used for bond strength testing by the modified E8 test, which was produced from a 10 mm thick coating. In order to obtain more experimental data to fulfill NWMO modelling needs, selected mechanical tests were also performed on the coating after heat treatment at 600 °C and on the A516 grade 70 substrate in the as-received state and after heat treatment for 1 h at 350 °C and 600 °C. The coating characterization data are summarized in Table 5 while spray conditions are shown Appendix A.1.

Table 5: Selected characterization results for N_2-sprayed coatings annealed for 1 h at 350 °C, 400 °C, and 600 °C.

Label	T_{anneal}	t_{anneal}	Bond Strength ASTM C633	Bond Strength modified ASTM E8‡	Coating Tensile Strength	Coating Failure Strain	A516 Tensile Strength	A516 Failure Strain
	°C	h	MPa	MPa	MPa	%	MPa	%
As-spray	-	-	61 ± 4*	33.3 ± 6.8	171 ± 14†	0.2 ± 0.0	511 ± 8	24.3 ± 0.2
350 °C	350	1	58 ± 10**	67.0 ± 4.8	198 ± 7	23.2 ± 3.0	508 ± 5	24.6 ± 0.5
400 °C	400	1	-	-	194 ± 11††	25.9 ± 6.6	-	-
600 °C	600	1	13 ± 5***	45.9 ± 5.9	189 ± 10	29.6 ± 5.1	472 ± 4	26.7 ± 0.3

* Epoxy failure (within glue; not interface).
** Epoxy failure (within glue; not interface); 3 of 5 samples used (remaining two showed gaps between the glue and the sample)
*** Cohesive failure (within coating; not interface)
† All five replicates failed outside of gage – strength and elongation values only included for reference.
†† Failure outside of gage for one replicate – average value taken from four other replicates.
‡ Testing by Exova (Cambridge, ON) on 10 mm thick coatings. All other testing was performed on 3 mm thick coatings.

Micrographs of the as-polished coating cross-sections, shown in Figure 26a-c, indicated that coating porosity did not increase significantly after heat treatment at 350 °C (Figure 26b) or 400 °C (Figure 26c), which was consistent with previous observations during general coating development. Instead, any differences in observed porosity were attributable to variations in the as-sprayed coating. Micrographs of the etched samples, shown in Figure 26d-f, revealed that the development of equiaxed grains within deformed particles after heat treatment is due, presumably, to recrystallization. These grains appeared to be more refined than those observed for the as-received powder (Figure 4b). Grain boundaries were not resolved in the as-

sprayed microstructure (Figure 26d) and the deformed particle boundaries were heavily over-etched in order to reveal grain boundaries in the coatings annealed at 350 °C and 400 °C (Figure 26e and f, respectively).

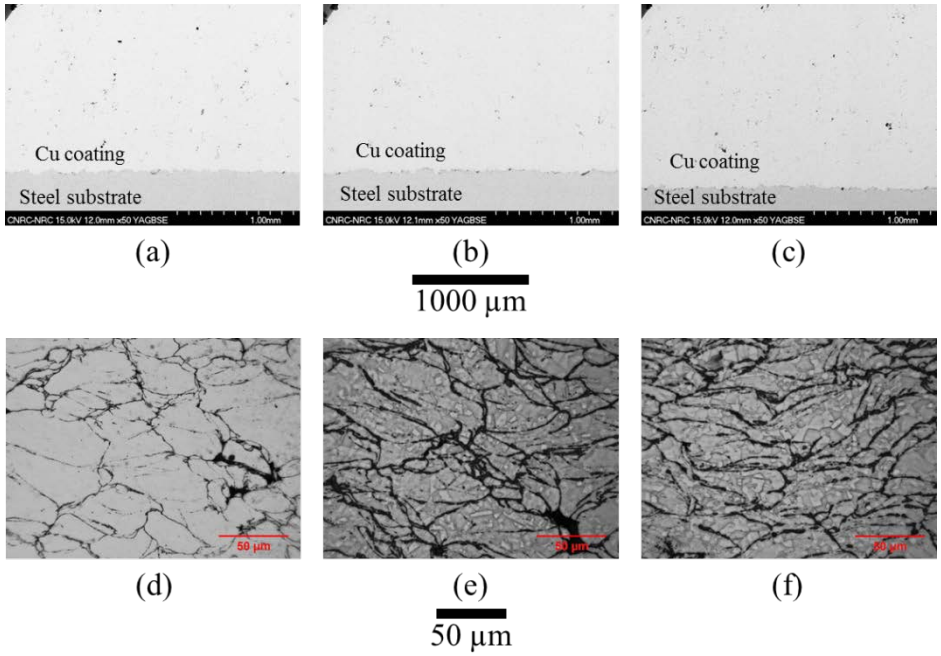


Figure 26: Reference coatings (d_{50} = 42 µm powder): as-polished microstructures for (a) as-sprayed, (b) after 350 °C/1 h anneal, and (c) after 400 °C/1 h anneal; and etched microstructures for (d) as-sprayed, (e) after 350 °C/1 h anneal, and (f) after 400 °C/1 h anneal.

Representative stress-strain curves for the coating-only specimens are shown in Figure 27, while tensile strength and elongation were summarized in Table 5. The as-sprayed coating displayed a tensile strength of 171 ± 14 MPa and strain to failure of 0.2 ± 0.0 %. Heat treatment of coatings for 1 h at 350 °C, 400 °C, and 600 °C produced increases in ductility values to 23.2 ± 3.0 %, 25.9 ± 6.6 %, and 29.6 ± 5.1 %, respectively, as well as minor increases in tensile strength to 198 ± 7 MPa, 194 ± 11 MPa, and 189 ± 10 MPa, respectively. The change in as-sprayed tensile strength for reference parameter coatings compared to that measured in earlier development work (Table 3, section 4.3) can probably be attributed to the changes in geometry (from 165 mm × 140 mm × 3 mm to 152 mm × 152 mm × 38 mm) as well as spray conditions (T_g = 800 °C, feeder rotation rate = 0.7 rpm, and SOD = 25 mm to T_g = 800 °C, SOD = 30 mm, and feeder rotation rate = 2.4 rpm). However, the increase in ductility with annealing is consistent with the earlier results.

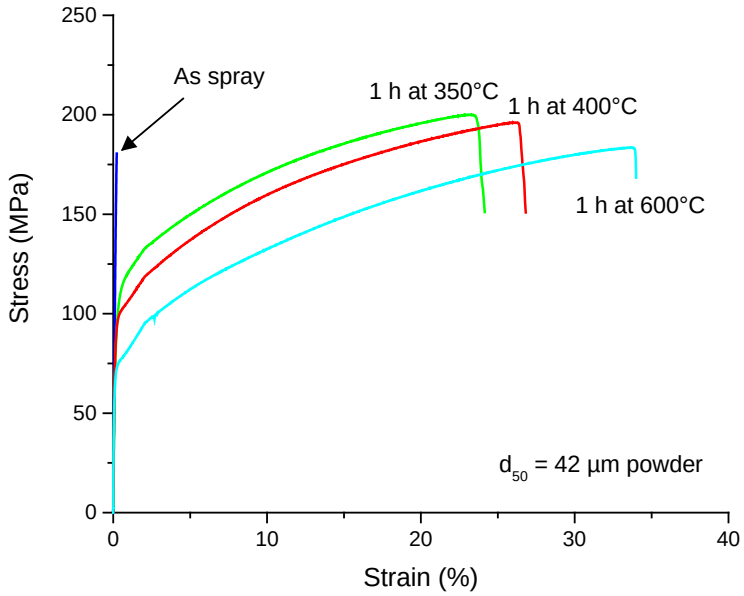


Figure 27: Representative stress-strain curves for reference coating coatings (d_{50} = 42 µm powder) as-sprayed and after anneal for 1 h at 350 °C, 400 °C, and 600 °C.

Representative stress-strain curves for the substrate-only samples (A516 grade 70) are shown in Figure 28. The as-received A516 material displayed a tensile strength of 511 ± 8 MPa and strain to failure of 24.3 ± 0.2 %, which are within material specifications for grade 70 (485-620 MPa and minimum 21% elongation at break). Heat treatment produced no change after samples were annealed at 350 °C (511 ± 5 MPa; 24.6 ± 0.5 %) and a ~10% decrease in tensile strength after they were annealed at 600 °C (472 ± 4 MPa; 26.7 ± 0.3 %).

Additional bend testing and bond strength testing were performed for coatings heat treated at 350 °C and 600 °C. Figure 29 shows representative test samples after bend testing following standard ASTM E290-09. For as-sprayed coatings, early failure with no ductility was observed. For coatings heat treated at 350°C, ductility was improved compared to that of samples in the as-sprayed condition. Outside cracking was observed first, followed by debonding from the steel substrate at bend angles of 90°. Coatings heat treated at 600°C also showed debonding at 90° for four specimens; however, the fifth sample did not debond during the test. The observed behaviour for coatings annealed at 600 °C differed slightly from that observed during general coating development (Figure 15c, section 4.3), which showed no failure for bend angles above 90° in any samples. Although the cause of failure was not isolated (outside of work scope), the failed coatings displayed a bubbled surface appearance after annealing that was not observed during previous testing. This may have indicated that an external variable, introduced during sample preparation (e.g., contamination during machining), had a potentially adverse effect on ductility. There was also a difference in the substrate (material and thickness) from that used during the general coating development.

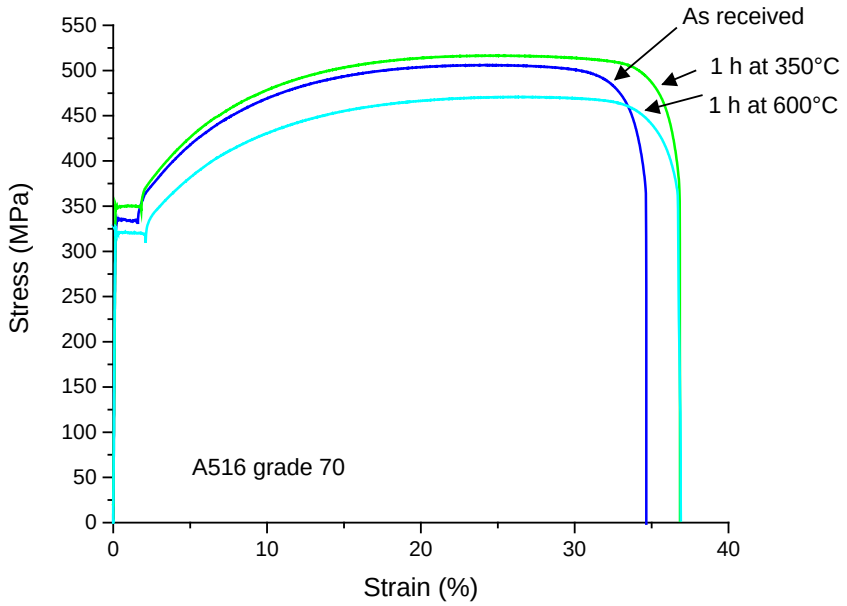


Figure 28: Representative stress-strain curves for A516 grade 70 as-received and after annealing for 1 h at 350 °C and 600 °C.

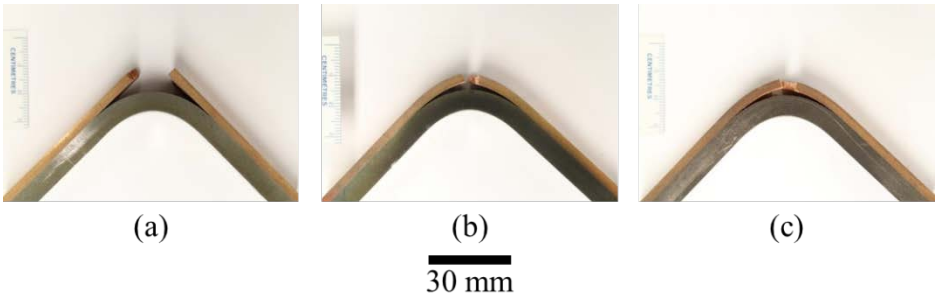


Figure 29: Representative photos after bend testing of reference coatings (d_{50} = 42 µm powder): (a) as-sprayed, (b) after 350 °C/1 h anneal, and (c) after 600 °C/1 h anneal.

Bond strength testing of 3 mm thick coatings with the conventional ASTM C633 (ASTM International 2001) method showed glue failure (i.e., no debonding at the coating-substrate interface) for coatings as-sprayed and after a 350°C anneal (glue failure at 61 ± 4 MPa and 58 ± 10 MPa, respectively). However, a significantly lower bond strength value (13 ± 5 MPa) was obtained for coatings after the 600 °C anneal. The bond strength specimens (600 °C anneal) showed cohesive-type failure (within the coating very close to the substrate interface), which was unexpected, as a coating tensile strength of 189 MPa ± 10 MPa was obtained for coating-only (i.e., cohesive) tensile testing. In addition, bond strength testing during the general coating development (section 4.3) showed an increase in bond strength (glue failure) was achieved

after a 600 °C anneal. As a result, a brief failure analysis was performed for this low bond strength specimen (13 ± 5 MPa after a 600 °C anneal).

Figure 30 shows micrographs of each side of the fracture in cross-section (a, b, e, f) and surface view (c, d, g, h). The cross-sections showed a relatively uniform thickness of coating remaining on the substrate (a, e) and limited evidence of failure defects (e.g., cracks) within the coating in the vicinity of the fracture (a, b, e, f). The uniformity and localisation of the failure, as well as the thickness (~50 µm estimated from a and e) of the remaining coating on the A516 substrate, suggested that the failure occurred between the He-sprayed bond coat and the N_2-sprayed top coat. Although minor dimpled areas (d, h) were observed, the bulk of the fracture surface showed inter-particle fracture (c, g), in other words, debonding of particles, as opposed to material failure within particles (as discussed for Figure 13g-i in section 4.3). The unexpected failure between the bond and top coats may be a one-time outlier due to the bubbled surface formed after the 600 °C anneal (that was noted earlier in the bend testing). However, it should be noted that the procedure for spraying the top coat onto the bond coat is not rigidly defined in terms of time elapsed before the top coat is applied. NRC experience has shown that there is a practical time limit between substrate preparation and coating application before coating properties are affected; this situation may be analogous.

Bond strength testing using the modified ASTM E 8 (ASTM International 2011) test was again performed by the same external contractor (Exova, Cambridge, ON) as in section 5.1 . Results for samples extracted from a 10 mm thick coating indicated an increase from the as-sprayed bond strength (33.3 ± 6.8 MPa) that was obtained after annealing at 350 °C (67.0 ± 4.8 MPa). An increase in bond strength from the as-sprayed condition, although lower in magnitude, was also obtained after annealing at 600 °C (45.9 ± 5.9 MPa). All failures occurred in the copper coating, with no measurable elongation. It should be noted that the as-sprayed bond strength values reported here are much lower than the value of 83 ± 15 MPa reported in earlier testing by Exova (section 5.1). In the earlier testing, all failures occurred at the interface between the coating and the substrate (i.e., indicating bond strength between coating and substrate). For this set of samples, the observed failure within the copper coating itself (above the coating-substrate interface) was an indication that results may not correctly represent the bond strength of the interface. A combination of the low measured strengths for these in-coating failures (compared to coating-only tensile testing shown in Figure 27), observations of possible machining defects, and out-of-gage failures near the fillet area of some samples suggest that these results need to be investigated further.

Overall, the tensile testing and microstructural characterization of coatings heat treated for 1 h at 350-400 °C demonstrated that these coatings possessed acceptable strength and ductility. Although the 400 °C anneal caused the development of more (qualitatively) uniform equiaxed grains, the lower temperature 350 °C anneal may be preferable from a practical standpoint. In addition, testing of the A516 grade 70 substrate as-received and after annealing at 350 °C showed no differences in tensile strength or elongation to failure; this indicates no reduction in substrate mechanical properties due to the coating heat treatment . Further testing is probably warranted to ensure reliability and consistency in the data, particularly if the 600 °C anneal is viewed as a viable option in future practice.

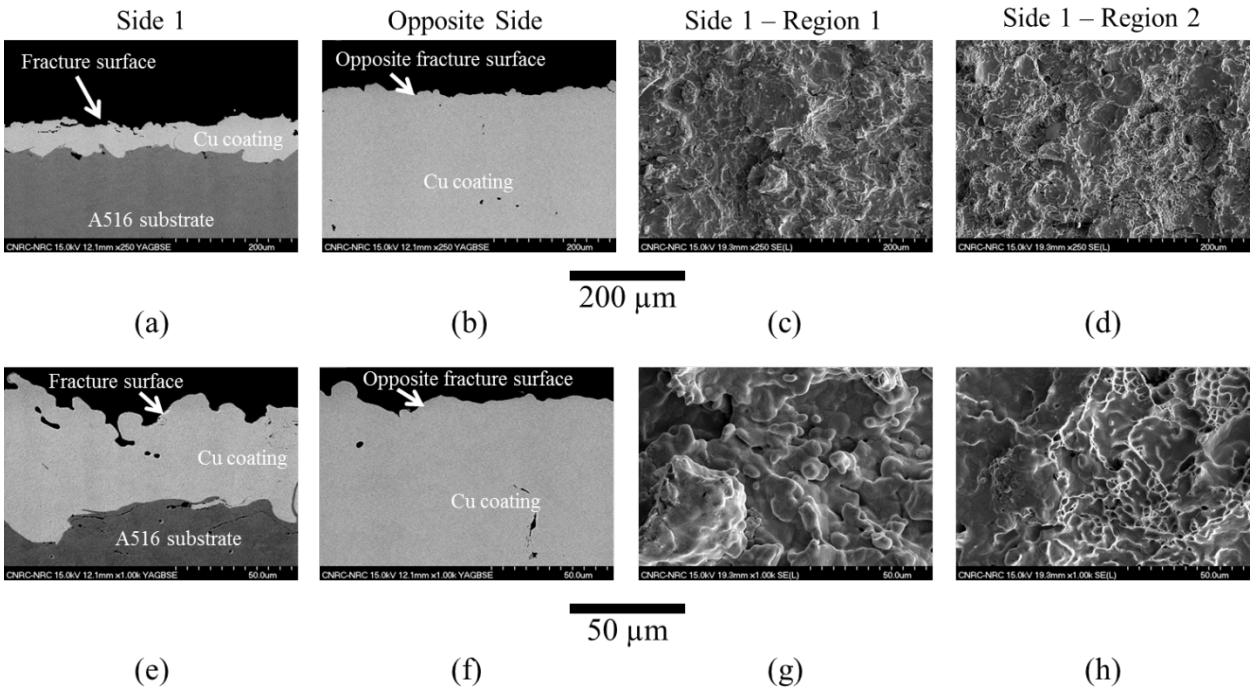


Figure 30: Representative micrographs of low-strength, cohesive failure after 600 °C anneal: cross-section at low magnification of (a) one side of failure and (b) opposite side; fracture surface at low magnification of (c) one side and (d) second region of same side; cross-section at high magnification of (e) one side of failure and (f) opposite side; fracture surface at high magnification of (g) one side and (h) second region of same side.

6. PROTOTYPING

6.1 PROCESS ADJUSTMENTS

In order to scale up from 150 mm × 150 mm planar samples to UFC mock-up assemblies of up to 2.15 m length, the validated coating parameters required several adjustments. Changes in substrate handling and preparation (e.g., lift system, portable grit blast, etc.) and productivity (e.g., increased feed rate) were relatively straightforward to introduce. In comparison, significantly greater effort was needed for the development of a new procedure for reducing He gas consumption. Although performed to accommodate facility He gas storage capability, this modification is also a step forward in process cost optimization.

For the prototyping activities, coating of the first cylindrical pipe segment was performed with the conditions validated for the planar samples (Section 5.1), while all subsequent coatings were produced with the adjusted conditions described here (Section 6.1). Spray conditions for prototyping activities are shown in Appendix A.1. The reference coating process for both N_2 and He gas spray used the same nozzle, which featured a nozzle diameter designed to maximize N_2-spray productivity. Consequently, a nozzle with smaller (throat and exit) diameters optimized for He-spray was employed in order to reduce flow rate (~ 65 % lower) while still maintaining

similar particle velocity (measured with N_2 gas only). A switch to the smaller diameter nozzle (for bond + top coats), with all other conditions kept constant, to produce a 3 mm thick coating on A36 cylinders (25.4 mm Ø × 38.1 mm thick) resulted in a bond strength of 42 ± 5 MPa, which was lower than that obtained on coatings produced with the larger diameter nozzle (i.e., min. 60-70 MPa).

The difference obtained with the two nozzles was attributed to a lower substrate temperature caused by less gas flow through the smaller diameter nozzle. To investigate this hypothesis, the substrate surface temperatures were measured using an infrared camera for simulated (i.e., powder-free) deposition runs. Using the small nozzle resulted in 15-20 °C lower substrate temperatures. Consequently, the substrate temperature was raised using two simulated runs (without powder) prior to actual deposition runs, and the resultant coatings met bond strength requirements, with a value of 61 ± 3 MPa (epoxy failure). Concurrently, it was found that the preheating could be done using a radiant lamp, for a similar bond strength result (58 ± 2 MPa, epoxy failure). Subsequent to the nozzle switch, the powder feed rate was increased from 80 g/min to 250 g/min in order to increase productivity. The increase in powder load did not adversely affect the coating porosity as measured via image analysis (not shown). However, a decrease in adhesion occurred (43 ± 7 MPa), principally due to the higher deposition rate, and not the powder feed rate itself. When the rotation speed of the samples was increased to match the deposition rate obtained at the lower feed rate, the coating adhesion recovered (56 ± 5 MPa).

Coatings for prototyping were applied using the PCS-800 cold spray unit with two large lots of d_{50} = 42 µm powder (lots D and E). However, it was immediately found that the coatings produced using lot E displayed lower adhesion than the others. It was initially unclear if the poorer performance of this lot was due to a different powder surface state and/or a higher proportion of coarse particles in this lot (d_{90} = 62-67 µm for lots A-D and 72 µm for lot E). Both powder sieving and powder heat treatment under H_2 helped to recover adequate coating adhesion, but only powder sieving was actually performed prior to prototyping coating.

6.2 CYLINDRICAL BODY

The reference coating was applied to a ~ 300 mm length of a pipe segment of A106 grade C steel (508 mm x 406 mm x 38 mm) fixed on a turntable, shown in Figure 2e. The compositions of A106 Grade C steel and A516 Gr. 70 steel, shown in Appendix A.2, are similar. Spray conditions are shown in Table 14 of Appendix A.1. The He-sprayed bond coat, N_2-sprayed top coat, and machined surface displayed macro appearances (Figure 31) similar to those obtained in the planar validation (Figure 22). Although not specifically measured or recorded during production, the He-sprayed bond coat thickness was estimated to be ~100-150 µm, based on the planar validation results, while the N_2-sprayed top coat thickness was 3.85 ± 0.20 mm (as-deposited). SEM micrographs of the coating (not shown) in locations at the top, mid-length, and bottom of the coated pipe revealed the coating to be completely dense at all three locations.

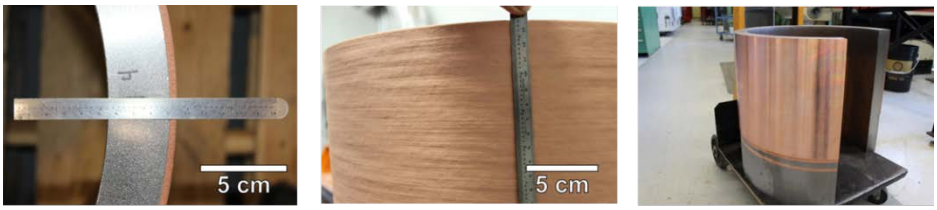


Figure 31: Photos of coating (d_{50} = 42 µm powder) produced on A106 grade C steel: (a) top view as-sprayed, (b) side view as-sprayed, (c) side view after machining.

6.3 HEMISPHERICAL HEAD

Two methods were used to coat the hemispherical heads: via simultaneous rotation of the heads and manipulation of the cold spray gun; and via sequential masking of stationary heads with gun manipulation. Figure 32a illustrates some developmental patterns explored during the former approach, which occasionally led to incomplete or uneven coverage, while Figure 32b illustrates the coating with mask used in the latter method. A view of the latter method is also shown in Figure 2f. Full sized heads were made using both approaches, and spray conditions are shown in Table 14 of Appendix A.1.

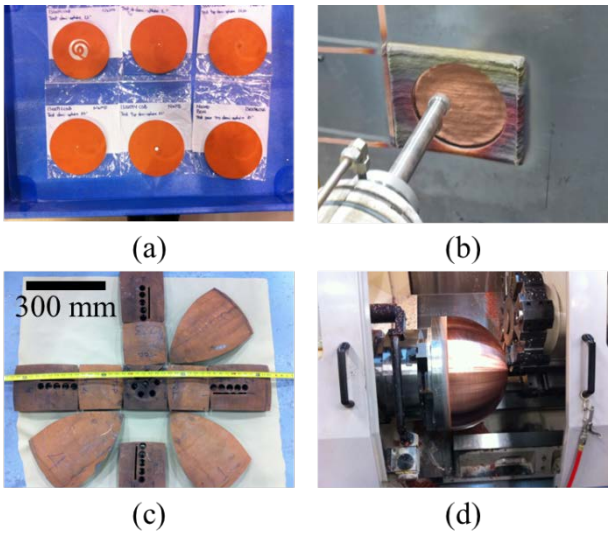


Figure 32: Photos showing coating development for hemispherical head: (a) coated dishes (with geometry matching that of the apex) used in the optimization of a curved spray pattern, (b) apex coated using an XY pattern with masking, (c) coated hemisphere sectioned for characterization, and (d) CNC machining of a coated hemisphere.

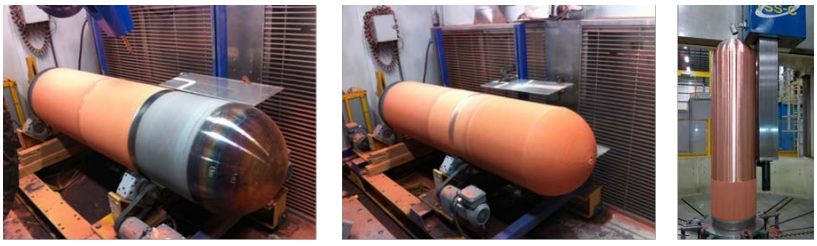
Specimens from the coating on the actual hemispherical head were machined by EDM (Figure 32c) and results showed good coating uniformity, except near the sphere apex. Coating adhesion was estimated following ASTM C 633 (ASTM International 2001) standard guidelines, although it must be noted that a bias was introduced by the curved coating surface (probable

change in stress distribution and difficult alignment of the pull studs with the tensile axis). Coating adhesions between 35 MPa and 55 MPa were achieved; the highest value being obtained at the apex of the sphere. One coated hemispherical head was CNC machined for demonstration purpose (Figure 32d).

6.4 MOCK-UP AND LOWER ASSEMBLY

The coating process for the used fuel container was first demonstrated on one mock-up assembly consisting of the cylindrical body, hemispherical head, and weld transition. This assembly represented a full size hemispherical head and weld transition) with a truncated cylindrical body (560 mm Ø × 620 mm part length). An actual lower assembly consisting of a full size cylindrical shell welded to the lower hemi-spherical head (full part length of 2270 mm) was subsequently coated. The setup for coating the truncated assembly and full-sized lower assembly, shown in Figure 2g and h, respectively, employed a horizontal frame with motorized rollers to rotate the assemblies. Spray conditions are shown in Table 14 of Appendix A.1.

Due to the large assembly sizes, the coatings were applied in sections over multiple work days. This practical issue required the development of restarting procedures to account for surface preparation and blending/joining of the coatings deposited on previous sections. In principle, previously coated sections may undergo slight surface oxidation, which must be removed prior to overspraying; there is also a necessary substrate temperature to achieve satisfactory coatings, as presented in the nozzle selection discussion of Section 6.1. Accordingly, the spray pattern was modified to produce a taper at the edge of each day's section in order to mitigate coating variation at the transition between sections. Prior to spraying, both the overlapping copper region and the new section to coat were grit blasted at the same time. Post deposition microstructural observations of coupons produced under similar conditions did not show any coating variation in overlap regions. Figure 33 shows the full-sized lower assembly after coating of two sections and the entire assembly. Similarly to the hemispherical head, both assemblies were machined following deposition, as shown in Figure 33.



(a) (b) (c)

Figure 33: Full-sized lower assembly (a) after coating of two sections, (b) after coating of entire lower assembly, and (c) after partial machining of lower assembly.

6.5 CLOSURE WELD

The coating process was applied to the two main components of the used fuel container: the lower assembly and the upper hemi-spherical head. These components were subsequently

joined by closure welding using HLAW (hybrid laser arc welding) by Novika (La Pocatière, Quebec). Following weld cap removal, the remaining closure zone area was copper coated. Figure 34 shows the assembled UFC before and after closure zone coating and final machining. . The spray procedure was similar to that used for the cylindrical portion of the lower assembly, with spray conditions shown in Table 14 of Appendix A.1.



(a) (b) (c)

Figure 34: Full-sized leading assembly: (a) close-up of closure weld area after welding and machining, (b) installed with collars on roller frame prior to coating of the closure weld, and (c) after coating and machining of the closure weld.

7. CONCLUSIONS

The successful application of the cold spray coating technology to full-scale, geometrically representative UFC mock-up configurations (carbon steel cylindrical/spherical heads, applicable weld substrates) was demonstrated through activities involving (i) powder selection, (ii) general coating development, (iii) used fuel canister coating optimization, and (iv) prototyping. Reference spraying and annealing conditions were established, and coating quality and properties were validated on different substrate geometries and compositions. Results also indicated that powder manufacturing and robust handling procedures are key considerations for reliability and consistency of coating properties. A clear path to manufacturing copper coatings on UFCs via cold spray deposition was developed, including details on (i) process parameter scale-up adjustment, (ii) spray set up and pattern development, (iii) coating joining procedure, and (iv) coating machining. Ongoing development of the coating process is focused on the weld closure zone, where the process will need to be adapted in order to limit the rotation of filled used fuel containers. The establishment of a clear operating window sufficient for large scale manufacturing is also still required, and will be investigated in ongoing work.

ACKNOWLEDGEMENTS

The following NRC technical officers were involved in experimental testing: J.-F. Alarie, J.-C. Tremblay, J. Sykes, M. Lamontagne, B. Harvey, D. de Lagrave, S. Mercier, C. Hoang, M. Thibodeau, K. Théberge, and R. Rouillier. NWMO thanks Nagra for funding toward this project

REFERENCES

Alkhimov, A. P., S. V. Klinkov and V. F. Kosarev. 2000. Experimental study of deformation and attachment of microparticles to an obstacle upon high-rate impact. Journal of Applied Mechanics and Technical Physics 41, 245-50.

Arabgol, Z., H. Assadi, T. Schmidt, F. Gärtner and T. Klassen. 2014. Analysis of thermal history and residual stress in cold-sprayed coatings. Journal of Thermal Spray Technology 23, 84-90.

Assadi, H., T. Schmidt, H. Richter, J. O. Kliemann, K. Binder, F. Gärtner, T. Klassen and H. Kreye. 2011. On parameter selection in cold spraying. Journal of Thermal Spray Technology 20, 1161-1176.

ASTM International. 2001. ASTM C 633 Standard Test Method for Adhesion or Cohesion Strength of Thermal Spray Coatings. West Conshohocken, USA.

---. 2006. ASTM B 152/B 152M - 06a Standard Specification for Copper Sheet, Strip, Plate, and Rolled Bar. West Conshohocken, USA.

---. 2009a. ASTM E 290 - 09 Standard Test Methods for Bend Testing of Material for Ductility. West Conshohocken, USA.

---. 2009b. ASTM E 8/E 8M - 09 Standard Test Methods for Tension Testing of Metallic Materials. West Conshohocken, USA.

---. 2010. ASTM E384-10 Standard Test Method for Microindentation Hardness of Materials. West Conshohocken, USA.

---. 2011. ASTM E 8 - 11 Standard Test Methods for Tension Testing of Metallic Materials. West Conshohocken, USA.

Calla, E., D. G. McCartney and P. H. Shipway. 2006. Effect of Deposition Conditions on the Properties and Annealing Behavior of Cold-Sprayed Copper. Journal of Thermal Spray Technology 15, 255-262(8).

Caron, R. I., R. G. Barth and D. E. Tyler. 2004. Metallography and Microstructures of Copper and Its Alloys. In *ASM Handbook Volume 9*, 775-788. ASM International. Materials Park, OH.

Choi, H.-J., M. Lee and J. Y. Lee. 2010. Application of a cold spray technique to the fabrication of a copper canister for the geological disposal of CANDU spent fuels. Nuclear Engineering and Design 240, 2714-2720.

Dykhuizen, R. C. and M. F. Smith. 1998. Gas dynamic principles of cold spray. Journal of Thermal Spray Technology 7, 205-12.

Dykhuizen, R. C., M. F. Smith, D. L. Gilmore, R. A. Neiser, X. Jiang and S. Sampath. 1999. Impact of high velocity cold spray particles. Journal of Thermal Spray Technology 8, 559-64.

Gartner, F., T. Stoltenhoff, J. Voyer, H. Kreye, S. Riekehr and M. Kocak. 2006. Mechanical properties of cold-sprayed and thermally sprayed copper coatings. Surface & Coatings Technology 200, 6770-6782.

Gilmore, D. L., R. C. Dykhuizen, R. A. Neiser, T. J. Roemer and M. F. Smith. 1999. Particle velocity and deposition efficiency in the cold spray process. Journal of Thermal Spray Technology 8, 576-82.

Hyun, S. K., K. Murakami and H. Nakajima. 2001. Anisotropic mechanical properties of porous copper fabricated by unidirectional solidification. Materials Science and Engineering: A 299, 241-248.

Jakupi, P., P. G. Keech, I. Barker, Ramamurthy, R. L. Jaklin, D. W. Shoesmith and D. E. Moser. 2015. Characterization of Commercially Cold-Sprayed Copper Coatings and Determination of the Effects of Impacting Copper Powder Velocities. Journal of Nuclear Materials 466, 1-11.

Kim, S. K., M. S. Lee, H. J. Choi, J. W. Choi and T.-W. Kwak. 2009. Progress of a cost optimization for an HLW repository in Korea. Progress in Nuclear Energy 51, 401-408.

Kwong, G. M. 2011. Status of Corrosion Studies for Copper Used Fuel Containers Under Low Salinity Conditions, NWMO TR-2011-14.

Lee, M. S., H. J. Choi, J. W. Choi and H. J. Kim. 2011. Application of cold spray coating technique to an underground disposal copper canister and its corrosion properties. Nuclear Engineering and Technology 43, 557-566.

Maier, K. 1977. Self-Diffusion in Copper at "Low" Temperatures. Physica Status Solidi A 44, 567-576.

McCune, R. C., W. T. Donlon, O. O. Popoola and E. L. Cartwright. 2000. Characterization of copper layers produced by cold gas-dynamic spraying. Journal of Thermal Spray Technology 9, 73-82.

Metal Powder Industries Federation. 1985. MPIF Standard 03 Determination of Flow Rate of Free-Flowing Metal Powders Using the Hall Apparatus. Princeton, USA.

Papyrin, A. 2001. Cold spray technology. Advanced Materials and Processes 159, 49-51.

Sandström, R. and H. C. M. Andersson. 2008. The effect of phosphorus on creep in copper. Journal of Nuclear Materials 372, 66-75.

Sandström, R. and R. Wu. 2013. Influence of phosphorus on the creep ductility of copper. Journal of Nuclear Materials 441, 364-371.

Schmidt, T., H. Assadi, F. GÃ¤rtner, H. Richter, T. Stoltenhoff, H. Kreye and T. Klassen. 2009. From particle acceleration to impact and bonding in cold spraying. Journal of Thermal Spray Technology 18, 794-808.

Schmidt, T., F. Gartner, H. Assadi and H. Kreye. 2006. Development of a generalized parameter window for cold spray deposition. Acta Materialia 54, 729-742.

Stoltenhoff, T., C. Borchers, F. Gartner and H. Kreye. 2006. Microstructures and key properties of cold-sprayed and thermally sprayed copper coatings. Surface and Coatings Technology 200, 4947-4960.

Van-Steenkiste, T. H., J. R. Smith, R. E. Teets, J. J. Moleski, D. W. Gorkiewicz, R. P. Tison, D. R. Marantz, K. A. Kowalsky, W. L. Riggs, P. H. Zajchowski, B. Pilsner, R. C. McCune and K. J. Barnett. 1999. Kinetic spray coatings. Surface and Coatings Technology 111, 62-71.

Wong, W., E. Irissou, P. Vo, M. Sone, F. Bernier, J. G. Legoux, H. Fukanuma and S. Yue. 2013. Cold Spray Forming of Inconel 718. Journal of Thermal Spray Technology 22, 413-421.

Xiong, Y., W. Zhuang and M. Zhang. 2015. Effect of the thickness of cold sprayed aluminium alloy coating on the adhesive bond strength with an aluminium alloy substrate. Surface and Coatings Technology 270, 259-265.

APPENDIX A: PROCEDURES AND ADDITIONAL DATA

CONTENTS

Page

A.1 SUMMARY OF SPRAY CONDITIONS AND CHARACTERIZATION DATA 44
A.2 EXPERIMENTAL PROCEDURES 51
A.3 GENERAL SELECTION OF ANNEALING CONDITIONS – ADDITIONAL EXPERIMENTS 57
A.4 SAMPLE PRODUCTION FOR CORROSION TESTING 62

A.1 SUMMARY OF SPRAY CONDITIONS AND CHARACTERIZATION DATA

A summary of spray conditions and characterization data is shown in Table 6 to Table 14. Note that NRC IDs associated with the labels in Table 6 to Table 14 are shown in Table 15.

Table 6: Spray conditions and coating characterization results for powder selection (section 3).

Label	d_{50}	Gas	P_g	T_g	GTS	Step	SOD	v_p	Thickness	R_a	Porosity	$HV_{0.01}$	Bond Strength
	µm		MPa	°C	mm/s	mm	mm	m/s	mm	µm	%		MPa
P1	42	N_2	2	400	300	1	25	509 ± 67	0.54	9.5 ± 1.6	-	90 ± 10	31 ± 5
P2	42	N_2	3	600	300	1	25	616 ± 78	0.47	8.4 ± 1.2	0.6 ± 0.3	90 ± 11	41 ± 5
P3	42	N_2	4	800	300	1	25	696 ± 91	0.48	7.7 ± 0.9	-	81 ± 7	21 ± 15
P4	20	N_2	2	400	300	1	25	546 ± 115	0.63	8.0 ± 1.2	-	101 ± 17	3 ± 1
P5	20	N_2	3	600	300	1	25	637 ± 127	0.47	6.5 ± 1.4	0.2 ± 0.1	104 ± 13	28 ± 15
P6	20	N_2	4	800	300	1	25	692 ± 137	0.52	5.8 ± 1.0	-	88 ± 13	11 ± 3
P7	29	N_2	2	400	300	1	25	572 ± 49	0.52	7.6 ± 0.8	-	113 ± 6	10 ± 8
P8	29	N_2	3	600	300	1	25	668 ± 66	0.54	6.1 ± 1.0	0.2 ± 0.3	118 ± 6	14 ± 6
P9	29	N_2	4	800	300	1	25	763 ± 72	0.62	5.0 ± 0.6	-	117 ± 13	22 ± 2
P10	23	N_2	2	400	300	1	25	589 ± 74	0.68	7.8 ± 1.4	-	102 ± 7	11 ± 9
P11	23	N_2	3	600	300	1	25	724 ± 81	0.45	5.4 ± 0.5	0.1 ± 0.1	104 ± 10	15 ± 4
P12	23	N_2	4	800	300	1	25	821 ± 91	0.50	4.5 ± 0.5	-	103 ± 4	18 ± 4
P13	49	N_2	2	400	300	1	25	482 ± 71	0.39	9.8 ± 1.4	-	95 ± 13	11 ± 7
P14	49	N_2	3	600	300	1	25	572 ± 70	0.54	9.8 ± 1.5	2.6 ± 0.8	92 ± 10	9 ± 7
P15	49	N_2	4	800	300	1	25	660 ± 80	0.40	8.9 ± 1.8	-	89 ± 6	36 ± 14
P16	26	N_2	2	400	300	1	25	536 ± 89	0.35	8.9 ± 1.5	-	90 ± 7	14 ± 11
P17	26	N_2	3	600	300	1	25	556 ± 111	0.36	7.1 ± 1.0	1.0 ± 0.4	96 ± 7	25 ± 20
P18	26	N_2	4	800	300	1	25	677 ± 104	0.43	6.8 ± 0.7	-	89 ± 4	12 ± 7

Label = coating, d_{50} = powder, P_g = gas pressure, T_g = gas temperature, GTS = gun traverse speed, Step = step size SOD = standoff distance, v_p = particle velocity, Thickness = coating thickness, R_a = surface roughness

Table 7: Spray conditions and coating characterization results for selection of coating parameters (section 4.1).

Label	d_{50}	Gas	P_g	T_g	GTS	Step	SOD	v_p	Thickness	R_a	Porosity	$HV_{0.01}$	Bond Strength
	µm		MPa	°C	mm/s	mm	mm	m/s	mm	µm	%		MPa
G1	42	He	3.5	350	100	2	40	-	0.57	-	0.0 ± 0.1	103 ± 11	27 ± 4
G2	42	N_2	3	600	60	1	25	616	0.46 ± 0.03	8.71 ± 1.52	0.4 ± 0.6	91 ± 3	6 ± 7
G3	42	N_2	5	700	60	1	25	691	-	-	0.0 ± 0.1	78 ± 7	-
G4	42	N_2	5	600	60	1	25	665	0.61 ± 0.01	8.40 ± 1.21	0.1 ± 0.2	89 ± 4	10 ± 5
G5	42	N_2	5	500	60	1	25	619	0.60 ± 0.01	8.73 ± 1.28	0.2 ± 0.3	90 ± 7	8 ± 7
G6	42	N_2	5	400	60	1	25	571	0.71 ± 0.05	9.65 ± 1.42	0.4 ± 0.3	91 ± 3	4 ± 2
G7	42	N_2	5	800	60	1	25	693	0.84 ± 0.05	7.52 ± 0.98	0.0 ± 0.0	62 ± 7	29 ± 10
G8	42	N_2	5	800	1000	1	25	693	0.40 ± 0.02	6.47 ± 0.71	0.0 ± 0.0	63 ± 14	5 ± 0
G9	42	N_2	5	800	1000	1	100	750	0.60 ± 0.03	6.89 ± 1.01	0.1 ± 0.2	75 ± 15	9 ± 1
G10	42	N_2	5	700	1000	1	100	748	0.69 ± 0.03	7.38 ± 0.99	0.0 ± 0.0	87 ± 14	8 ± 1
G11	42	N_2	3	600	60	1	100	616	0.68 ± 0.02	9.57 ± 1.35	0.2 ± 0.3	98 ± 8	3 ± 1
G12	42	N_2	5	800	60	1	100	750	1.00 ± 0.04	7.36 ± 0.93	0.1 ± 0.2	57 ± 12	4 ± 4
G13	42	N_2	5	800	60	1	200	694	-	-	0.2 ± 0.3	-	-
G14	42	N_2	5	600	60	1	100	720	-	-	0.3 ± 0.3	-	-
G15	23	N_2	5	800	60	1	25	-	0.64 ± 0.09	4.57 ± 0.58	0.0 ± 0.0	81 ± 5	22 ± 3
G16	23	N_2	5	800	1000	1	25	-	0.84 ± 0.06	4.36 ± 0.61	0.0 ± 0.0	104 ± 13	13 ± 4
G17	23	N_2	5	800	1000	1	100	-	0.60 ± 0.02	4.11 ± 0.51	0.0 ± 0.1	88 ± 10	20 ± 4
G18	23	N_2	5	700	1000	1	100	-	0.52 ± 0.02	4.44 ± 0.59	0.0 ± 0.0	96 ± 14	13 ± 3

Table 8: Spray conditions and coating characterization results for general selection of annealing conditions (section 4.3).

Label	d_{50}	Gas	P_g	T_g	GTS	Step	SOD	Thickness	$HV_{0.01}$	Bond Strength
	µm		MPa	°C	mm/s	mm	mm	mm		MPa
G19-21	23	N_2	5	800	60	1	25	3.5 – 3.9	81 ± 5	67 ± 7*
G22-24	42	He	3.5	350	100	1.25	40	2.6 – 3.2	103 ± 11	23 ± 6
G25	42	N_2	5	800	60	1	25	2.28 ± 0.12	61 ± 7	46 ± 8

Label = coating, d_{50} = powder, P_g = gas pressure, T_g = gas temperature, GTS = gun traverse speed, Step = step size SOD = standoff distance, v_p = particle velocity, Thickness = coating thickness, R_a = surface roughness

* Epoxy failure (not interface failure)

Table 9: Spray conditions for production of corrosion test coatings used in EBSD analysis (section 4.4).

Label	d_{50}	Gas	P_g	T_g	GTS	Step	Rot (Ø)	SOD	Thickness
-	µm	-	MPa	°C	mm/s	(mm)	rpm (cm)	mm	mm
ACDS	12.5	He	4	300	300	1.25	No rotation	80	2.5
OD1	42	N_2	5	800	16.6	-	1006 (15)	30	3.62 ± 0.70
OD2	42	N_2	5	800	16.6	-	1006 (15)	30	3.28 ± 0.17
OD3	42	N_2	5	800	16.6	-	1006 (15)	30	3.43 ± 0.00
TP1	42	$He/N_2^{\dagger}$	5	800	1	-	238 (15)	30	0.37
TP2	42	$He/N_2^{\dagger}$	5	600	3.7	-	238 (15)	30	3.09 ± 0.09
BK1	42	$He/N_2^{\dagger}$	5	600	500	1	No rotation	30	2.93 ± 0.12

Label = coating, d_{50} = powder, P_g = gas pressure, T_g = gas temperature, GTS = gun traverse speed, setup = setup size, Rot (Ø) = substrate rotation (outer diameter of substrate fixture or part), SOD = standoff distance, Thickness = coating thickness

† He/N_2 = first pass with He-spray and all subsequent passes with N_2-spray

Table 10: Spray conditions and coating characterization results for validation of reference coatings (section 5.1).

Label	d_{50}	Gas	P_g	T_g	GTS	Rot (Ø)	SOD	Thickness	Porosity	Bond Strength
-	µm	-	MPa	°C	mm/s	rpm (cm)	mm	mm	%	MPa
A1	42	He/N_2[†]	5	800	1	63 (15)	30	3.37 ± 0.08	0.1 ± 0.1	68 ± 3
A2	42	N_2	5	800	1	60 (15)	30	Debonded	-	-
A3	42	N_2	5	800	1.9	118 (15)	30	Debonded	0.0 ± 0.1	-
A5	42	N_2	5	800	4	238 (15)	30	Debonded	-	-
A6	42	N_2	5	800	8	238 (15)	30	Debonded	-	-
A7	42	He/N_2[†]	5	600	0.9	56 (15)	30	2.81 ± 0.18	-	55 ± 12
A8	42	He/N_2[†]	5	600	1.1	66 (56)	30	3.08 ± 0.02	0.1 ± 0.2	68 ± 6
R1	42	He/N_2[†]	5	600	1.1	66 (56)	30	3.74 ± 0.03	0.5 ± 0.4	64 ± 5
R2	42	He/N_2[†]	5	600	1.1	66 (56)	30	3.17 ± 0.42	0.0 ± 0.4	61 ± 4
R3	42	He/N_2[†]	5	600	1.1	66 (56)	30	3.36 ± 0.08	-	-
R4	42	He/N_2[†]	5	600	1.1	66 (56)	30	3.37 ± 0.12	-	-
1 plate sprayed over 2 runs (R2+R4) to produce 5 mm thick coating 1 plate sprayed over 3 runs (R2+R3+R4) to produce 10 mm thick coating										

Table 11: Spray conditions and coating characterization results for reference coatings on weld substrates (section 5.2).

Label	d_{50}	Gas	P_g	T_g	GTS	Rot (Ø)	SOD	Thickness	Porosity	Bond Strength
-	µm	-	MPa	°C	mm/s	rpm (cm)	mm	mm	%	MPa
W1	42	He/N_2[†]	5	800	1	63 (15)	30	3.36	0.1 ± 0.1	-
W2	42	N_2	5	800	1	60 (15)	30	Debonded	-	-
W3	42	N_2	5	800	1.9	118 (15)	30	Debonded	-	-
W4	42	N_2	5	800	1	60 (15)	30	Debonded	-	-
W5	42	N_2	5	800	4	238 (15)	30	Debonded	-	-
W6	42	He/N_2[†]	5	600	1.1	66 (56)	30	3.21 ± 0.08	0.3 ± 0.3	61 ± 8

Label = coating, d_{50} = powder, P_g = gas pressure, T_g = gas temperature, GTS = gun traverse speed, Rot (Ø) = substrate rotation (outer diameter of substrate fixture or part), SOD = standoff distance, Thickness = coating thickness

[*] Epoxy failure (not interface failure)

[†] He/N_2 = first pass with He-spray and all subsequent passes with N_2-spray

Table 12: Spray conditions and coating characterization results for reference coatings on cast iron substrates (section 5.3).

Label	d_{50}	Gas	P_g	T_g	GTS	Rot (Ø)	SOD	Thickness	Porosity	Bond Strength
-	µm	-	MPa	°C	mm/s	rpm (cm)	mm	mm	%	MPa
C1	42	He/N_2[†]	5	800	1	63 (15)	30	3.05	0.1 ± 0.1	-
C2	42	N_2	5	800	1	60 (15)	30	Debonded	-	-
C3	42	N_2	5	800	1.9	118 (15)	30	Debonded	-	-
C4	42	He/N_2[†]	5	600	1.1	66 (56)	30	3.23 ± 0.10	0.4 ± 0.5	36 ± 12

Table 13: Spray conditions and coating characterization results for optimization of annealing conditions (section 5.4).

Label	d_{50}	Gas	P_g	T_g	GTS	Rot (Ø)	SOD	Feed[‡]	Thickness
-	µm	-	MPa	°C	mm/s	rpm (cm)	mm	g/min	mm
R1	42	He/N_2[†]	5	600	1.1	66 (56)	30	80	~3.7
R2	42	He/N_2[†]	5	600	1.1	66 (56)	30	80	~3.2
M1	42	N_2	4.5	800	1.1	66 (56)	30	60	~3.3
	42	He	4.9	800	1.1	66 (56)	30	80	
M2	42	He	4.5	800	1.1	66 (56)	30	60	~3.1
	42	N_2	4.9	800	1.1	66 (56)	30	80	
M3	42	He	4.5	800	1.1	66 (56)	30	60	~3.7
	42	N_2	4.9	800	1.1	66 (56)	30	80	
2 plates sprayed over 3 runs (M1+M2+M3) to produce 9.8-9.9 mm thick coatings									

Label = coating, d_{50} = powder, P_g = gas pressure, T_g = gas temperature, GTS = gun traverse speed, Rot (Ø) = substrate rotation (outer diameter of substrate fixture or part), SOD = standoff distance, Thickness = coating thickness

[*] Epoxy failure (not interface failure)

[†] He/N_2 = first pass with He-spray and all subsequent passes with N_2-spray (same spray parameters)

[‡] Approximate feed rate values are stated for reference only.

Table 14: Spray conditions for prototyping (section 6).

Label	d_{50}	Gas	P_g	T_g	GTS	Rot (Ø)	SOD	Feed‡	Comment
-	µm	-	MPa	°C	mm/s	rpm (cm)	mm	g/min	
B1	42	He	5	600	3.7	223 (51)	30	90	Cylindrical body (section 6.2)
	42	N_2	5	600	3.7	223 (51)	30	90	
H1	42	He	5	600	1-3	60 (56)	30	80	Hemisphere #1 (section 6.3)
	42	N_2	5	600	1-3	60 (56)	30	80	
H2	42	He	5	600	1-3	60 (56)	30	80	Hemisphere #2 (section 6.3)
	42	N_2	5	600	1-3	60 (56)	30	80	
H3	42	He	4.9	800	300	0*	30	80	Hemisphere #2 recoat (section 6.3)
	42	N_2	4.9	800	300	0*	30	105	
S1	42	He	4.9	800	0.8-2	60	30	80	Stubby (section 6.4)
	42	N_2	4.9	800	0.8-2	60	30	140	
L1	42	He	5	600	0.8-2	47 (56)	30	80	Lower Assembly (section 6.4)
	42	N_2	4.9	600	0.8-2	47 (56)	30	250	
L2	42	He	5	600	0.8-2	47 (56)	30	80	Lower Assembly recoat portion (section 6.4)
	42	N_2	4.9	600	0.8-2	47 (56)	30	270	
L3	42	He	4.5	800	300	0*	30	80	Lower Assembly recoat tip (section 6.4)
	42	N_2	4.9	800	300	0*	30	130	
WC	42	He	4.5	800	0.6	23.5 (56)	30	150	Weld Closure (section 6.5)
	42	N_2	4.9	800	0.6	23.5 (56)	30	150	

Label = coating, d_{50} = powder, P_g = gas pressure, T_g = gas temperature, GTS = gun traverse speed, Rot = substrate rotation, SOD = standoff distance, Thickness = coating thickness

* X-Y spray pattern without substrate rotation.

‡ Approximate feed rate values are stated for reference only.

Table 15: NRC ID numbers for each coating label.

Label	NRC ID	Label	NRC ID	Label	NRC ID
P1	1203277, 1203281	G13	1206135cs	C1	1301231csB + 1301232csB
P2	1203276, 1203282	G14	1206136cs	C2	1301243csB
P3	1203275, 1203283	G15	1206141cs	C3	1301251csB
P4	1204021, 1204027	G16	1206144cs	C4	1304231csB + 1304232csB
P5	1204022, 1204026	G17	1206142cs	M1	1405211csb + 1405212csb
P6	1204023, 1204025	G18	1206143cs	M2	1405221csb + 1405222csb
P7	12040311, 1204041	G19	1206273cs	M3	1405261csb + 1405262csb
P8	12040312, 1204042	G20	1206274cs	B1	1303221csB + 1303222csB
P9	12040313, 1204043	G21	1207101cs	H1	1310221csb
P10	1204028, 12040211	G22	1207041cs	H2	1310241csb
P11	1204029, 12040212	G23	1207042cs	H3	1406091csb + 1406101csb
P12	12040210, 1204031	G24	1207043cs	S1	1312091csb + 1312102csb
P13	12011625, 1201173	G25	1206275cs	L1	1312131csb + 1312171csb + 1312191csb
P14	12011626, 1201202	A1	1301231csB + 1301232csB	L2	1406191csb + 1406201csb
P15	12011627, 1201201	A2	1301243csB	L3	1409251csb
P16	1201094, 1201103	A3	1301251csB	WC	1411191csb
P17	1201101, 1201104	A5	1301302csB	ACDS	1112021
P18	1201102, 1201105	A6	1302011csB	OD1	1302132csb
G1	1205221cs	A7	1303181csB + 1303182csB	OD2	1302133csb
G2	1205292cs	A8	1303202csB + 1303203csB	OD3	1302134csb
G3	1205293cs	R1	1303211csB + 1303212csB	TP1	1302181csb+1302182csb
G4	1205294cs	R2	1305011csB + 1305012csB	TP2	1303261csb+1303262csb
G5	1205295cs	R3	1305021csB + 1305022csB	BK1	1304041csb+1304042csb
G6	1205296cs	R4	1305071csB + 1305072csB		
G7	1205297cs	W1	1301231csB + 1301232csB		
G8	1206121cs	W2	1301243csB		
G9	1206131cs	W3	1301251csB		
G10	1206132cs	W4	1301301csB		
G11	1206133cs	W5	1301302csB		
G12	1206134cs	W6	1304221csB + 1304222csB		

NRC IDs separated by (,) correspond to metallographic (plate) and pull test (disk) samples
NRC IDs separated by (+) correspond to He bond coat plus N_2 top coat(s)

A.2 EXPERIMENTAL PROCEDURES

A.2.1 Substrates

The substrate materials varied according to the specific tasks, as shown in Table 16.

Table 16: Substrate materials used by task.

Section	Task	Material(s)
3	POWDER SELECTION BASED ON COATING PROPERTIES	1020 rod and plate
4.1	GENERAL SELECTION OF COATING PARAMETERS	1020 rod
4.2	GENERAL REPAIR OF DAMAGED COATINGS	1020 plate
4.3	GENERAL SELECTION OF ANNEALING CONDITIONS	1020 plate
5.1	VALIDATION OF REFERENCE COATING ON PLANAR SUBSTRATES	A36 rod A516 grade 70 plate
5.2	APPLICATION OF REFERENCE COATING TO WELD SAMPLES	welded A516 grade 70 bar*
5.3	APPLICATION OF REFERENCE COATING TO CAST IRON SUBSTRATES	cast iron bar**
5.4	OPTIMIZATION OF ANNEALING CONDITIONS	A516 grade 70 plate
6.1	PROCESS ADJUSTMENTS	A36 and 44W rod
6.2	CYLINDRICAL BODY	A106 grade C pipe
6.3	HEMISPHERICAL HEAD	A516 grade 70
6.4	MOCK-UP AND LOWER ASSEMBLY	A516 grade 70
6.5	CLOSURE WELD	A516 grade 70

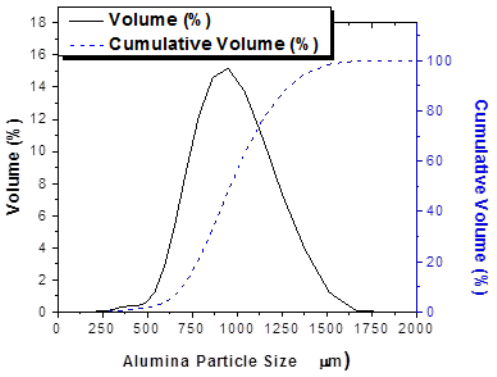
* procured by NWMO through Conestoga college
** supplied by SKB on behalf of NWMO/Nagra

The nominal compositions and yield strengths of A36, A44, and A106 grade C are similar to A516 grade 70 steel, as shown in Table 17.

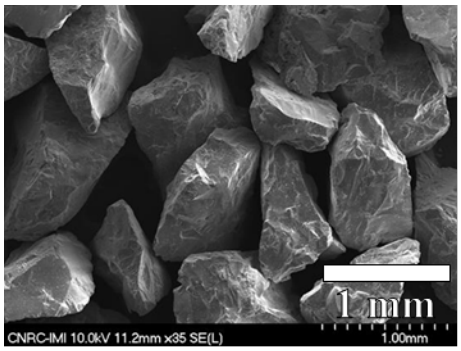
Table 17: Nominal compositions and yield strengths of A36, A516 grade 70, and A106 grade B steels.

ASTM	Composition, wt%						Yield Strength, min MPa (ksi)
	C	Mn	P	S	Si	Cu	
A516 Gr. 70	0.31	0.85-1.20	0.035	0.04	0.15-0.40	-	260 (38)
A36	0.29	0.80-1.20	0.04	0.05	0.15-0.40	0.20	220-250 (32-36)
44W	0.22	0.50-1.50	0.04	0.05	0.40	-	290-300 (42-44)
A106 Gr. C	0.35	0.29-1.06	0.025	0.025	0.10	-	275 (40)
1020	0.20	0.30-0.60	≤0.04	≤0.05	-	-	295 (43)

Substrate dimensions were varied to comply with the requirements of each type of test to be performed and substrate surfaces were machined (i.e., millscale on as-received A516 and A106 was removed). Prior to any copper deposition, the machined surface of a rod or plate substrate was first degreased with alcohol and then manually grit blasted using a Canablast Model M101P with an air pressure of 0.276 MPa (40 psi) and with an approximate blasting distance of 150 mm at 30° to normal direction. The blasting time was adjusted to ensure complete coverage. Due to the insufficient size capacity of the standard Canablast M101P unit, grit blasting of the pipe substrate was performed using a portable Canablast RCM-12/100PX unit. The grit blasting material and size were alumina (Al_2O_3) grit 24 (~975 µm) (Figure 35). In addition, an air gun was used to remove extraneous alumina particles on the grit blasted substrate surface.



(a)



(b)

Figure 35: Alumina grit characteristics: (a) particle size distribution and (b) alumina particle morphology.

A.2.2 Coating Systems

The PCS-1000 and PCS-800 cold spray systems from Plasma Giken Co. (Toshima-ku, Tokyo, Japan) were used, as well as the Kinetiks 4000 cold spray system from Oerlikon Metco (Westbury, NY).

A.2.3 Part Temperature

In some cases, the temperature of the part was measured using an infrared camera FLIR SC620 (Wilsonville, OR, USA).

A.2.4 In-Flight Particle Velocity Measurements

The in-flight particle velocity during cold spraying was measured via the coldspraymeter (coldspraymeter-003, Tecnar, St-Bruno, QC, Canada).

A.2.5 Metallographic Preparation

Powder and coatings were sectioned with a diamond wheel. Sectioned coatings and a small amount of powder were cold vacuum mounted in an epoxy resin, ground and then polished using standard metallographic preparation procedures. The following etchant was used for copper: 5 g Iron (III) chloride, 25 mL HCl, and 70 mL deoinized water. Variations of this etchant (5-25 g $FeCl_3$, 5-50 mL HCl, and 100 mL water) are used for microetching of copper and copper alloys (Caron, Barth and Tyler 2004). A 4% nital etchant (e.g., 4 mL HNO_3 and 96 mL alcohol) was used for the welded steel substrate.

A.2.6 Feedstock Powder Characterization – Size Distribution

The average particle size and the volume-weighted particle size distribution were measured via a laser diffraction particle size analyzer (LS320, Beckman Coulter, Miami, FL, USA).

A.2.7 Feedstock Powder Characterization – Shape Distribution

The feedstock powder shape distribution was assessed through the sphericity index, which was measured on mounted and polished powders with Nikon Eclipse ME600 optical microscope equipped with Clemex Vision analysis software version 3.5.

A.2.8 Feedstock Powder Characterization – Morphology

The as-received feedstock powder morphology was characterized using a field emission gun scanning electron microscope Hitachi S-4700 (FEG-SEM) in secondary electron imaging mode (SEI). Other parameters (working distance, magnification, acceleration voltages) are indicated directly on each individual micrograph. In addition, the as-received feedstock powder was cold vacuum mounted, ground, and then polished for cross-section examinations using the FEG-SEM in backscattered electron imaging mode (BSEI). The etched powder cross-sections were observed using a Nikon Eclipse ME600 optical microscope.

A.2.9 Feedstock Powder Characterization – Flowability

The powder flowability was assessed by measuring the time needed for a specific amount of powder to flow through flowmeter funnels (modified MPIF standard 03).

A.2.10 Chemical Composition Assessment – Feedstock Powder

The oxygen content of the feedstock powder was ,measured in accordance with the LECO method (LECO TCH600, Model 631-300-500).

A.2.11 SEM Characterization of Coatings

Coatings were characterized by microstructural analyses of polished cross-sections (via FEG-SEM BSEI), or by the JEOL JSM-6100 SEM in BSEI.

A.2.12 Optical Characterization of Coatings

Coatings were characterized for their topography using stereo-microscopy (stereoscope Bausch&Lomb stereozoom 7) or confocal microscopy (Sensofar Plμ 2300) when applicable. The coating polished cross-sections were characterised using an optical microscope (Nikon Eclipse ME600).

A.2.13 Coating Porosity Characterization

SEM BSEI and image analysis software (Visilog, St-Aubin, France) were utilized to measure through- thickness coating porosity. Coatings were cross-sectioned, vacuum mounted and polished. For each sample, porosity measurements were conducted using a minimum of ten images at a magnification of 500X. The average value was used as an indicator of the sample's porosity.

A.2.14 Substrate and Coating Roughness Characterizations

Substrate surface roughness (R_a) was characterized, if applicable, using a mechanical stylus profilometer, Mitutoyo Model SJ-201P (Kanagawa, Japan).

A.2.15 Coating Microhardness Characterization

Through-thickness microhardness measurements were performed on cold vacuum mounted and as-polished samples with a Buehler Micromet II Tester according to ASTM standard E384-10 (ASTM International 2010). All tests were achieved under 0.10 N loads for 15 seconds penetration time. For each specimen, a minimum of 12 indentations was performed. The highest and lowest values were removed from the dataset and the average value was calculated from the remaining data.

A.2.16 Coating Adhesion Strength Characterization

As determined by NWMO personnel and contractor (Exova Canada Inc., Cambridge, ON), surface adhesion was measured according to tensile tests based on the ASTM E08-11 standard (ASTM International 2011), with deviations in gage length (5.90 mm) and profile.

Coating adhesion strength tests performed by NRC followed the ASTM C-633-01 standard (ASTM International 2001). The samples were glued to grit blasted (Al_2O_3, grit 24) mild steel cylinders with an epoxy (FM-1000, Cytec Industries, Anaheim, CA) to form assemblies for testing. The epoxy was prepared by heating in an air furnace at 90°C for 3 hours prior to placement in the assembly. To ensure proper adhesion between the glue and the coating and

counter block interfaces, the assemblies were heated in the same furnace at 203°C for 3 hours. The assemblies were air cooled to room temperature. The adhesion strength tests were performed using an Instron 5582 universal testing machine (Burlington, Ontario, Canada) with a dynamic load up to 100 kN at a constant speed of 1.02 mm/min.

A.2.17 Coating Tensile Testing

Tensile test specimens were electric discharge machined (EDM) following Figure 36 and Table 18 specifications based on sub-size specimens for rectangular tension test specimens of ASTM E8/E8M-09 (ASTM International 2009b). These samples were extracted from the cold sprayed coatings with the tensile direction perpendicular to the spray direction. .

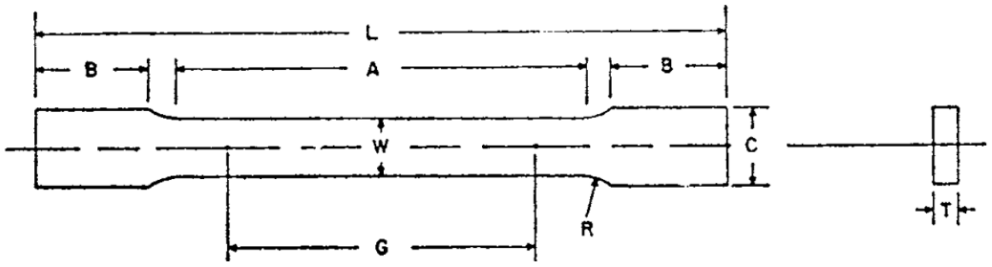


Figure 36: Tensile test specimen schematic (ASTM International 2009b) .

Table 18: Tensile test (sub-size) specimen dimensions.

Section	Dimension mm
G – Gage length	25
W – Width	6
T – Thickness	1
R – Radius of fillet	6
L – Overall length	100
A – Length of reduced section	32
B – Length of grip section	30
C – Width of grip section	10

A.2.18 Coating Bending Testing

Coating bending tests were performed according to ASTM E290-09 standard (ASTM International 2009a). Results described in section 4.3 were obtained using full thickness samples of 19 mm width × 127 mm length × 6.2 mm thickness (overall thickness including coating and substrate). Full thickness samples were not tested when coatings were produced on 38 mm substrates due to the large thickness. Consequently, results described in section 5.4 were obtained using 19 mm width × 127 mm length × 6.35 mm thickness (overall thickness including coating and substrate) samples. The coating thickness for all tests was about 3 mm. This qualitative test provided a way to rapidly evaluate the resistance to cracking during one continuous bend. Specimens were deformed up to 90°, although selected tests were stopped after the first crack was observed or continued to greater bend angles if ductility proved sufficient.

A.2.19 Heat Treatment Procedures

Heat treatment of coated samples was performed in a 10 cm diameter quartz tube furnace with a constant flow of argon.

A.3 GENERAL SELECTION OF ANNEALING CONDITIONS – ADDITIONAL EXPERIMENTS

In addition to the testing performed on N_2-sprayed, d_{50} = 23 µm powder coatings presented in section 4.3, identical mechanical testing was also performed on He-sprayed, d_{50} = 42 µm powder to investigate the differences in properties between N_2 and He spray (section A.1.1). Limited testing with N_2-sprayed, d_{50} = 42 µm powder was also performed to evaluate whether there was a powder-related effect with N_2-spray (section A.1.2). Selected characterization data for N_2 and He-sprayed coatings are summarized in Table 19. Note that the N_2-sprayed coatings were produced at T_g = 800 °C and P_g = 5 MPa, while the He-sprayed coatings were produced at T_g = 350 °C and P_g = 3.5 MPa. Complete spray conditions are shown in Table 8.

Table 19: Selected characterization results for N_2- and He-sprayed coatings annealed for 1 h at 300 °C and 600 °C.

Label	d_{50}	Gas	T_{anneal}	t_{anneal}	$HV_{0.01}$	Bond Strength	Tensile Strength	Failure Strain	Bend Angle
	µm		°C	h		MPa	MPa	%	°
G19-21	23	N_2	As-spray		81 ± 5	67 ± 7*	370 ± 33	0.5 ± 0.2	5 ± 1
G19-21	23	N_2	300	1	52 ± 4	66 ± 6*	245 ± 4	16.3 ± 3.2	52 ± 14
G19-21	23	N_2	600	1	36 ± 3	64 ± 5*	180 ± 2	34.5 ± 2.7	No crack
G22-24	42	He	As-spray		103 ± 11	23 ± 1	214 ± 22	0.3 ± 0.1	6 ± 0
G22-24	42	He	300	1	45 ± 6	32 ± 6	169 ± 6	7.3 ± 1.4	65 ± 10
G22-24	42	He	600	1	36 ± 2	37 ± 7	137 ± 12	6.3 ± 2.8	58 ± 3
G25	42	N_2	600	1	36 ± 2	46 ± 8	194 ± 10	27 ± 5	No crack

Label = coating, d_{50} = powder, T_{anneal} = anneal temperature, t_{anneal} = anneal time, Bend Angle = angle at first observed crack

* Epoxy failure (not interface failure)

A.3.1 Mechanical Properties of He-Sprayed Coatings

The effect of annealing on coating microhardness for He-sprayed coatings, shown in Figure 37 was similar to that of the N_2-sprayed coatings (Figure 12). A large reduction in hardness was obtained after annealing at relatively low temperature (e.g., 36 % decrease at 300 °C for the N_2-sprayed coatings and 40 % decrease at 200 °C for He-sprayed coatings). The high as-sprayed hardness of He-sprayed coatings (103 ± 11 $HV_{0.01}$) relative to the N_2-sprayed coatings (81 ± 5 $HV_{0.01}$) indicated a greater degree of particle deformation and represented a potentially greater driving force for microstructural restoration during annealing. For both N_2- and He-sprayed coatings, another potentially significant hardness decrease was observed at higher temperatures of 500-600 °C. The change in hardness obtained with an increase in annealing time at constant temperature was also relatively minor (i.e., generally less than 10% difference between 1 h and 10 h anneals) compared to the effect of anneal temperature.

The bond strength of He-sprayed coatings was improved after annealing, with values of 23 ± 6 MPa, 32 ± 7 MPa, and 37 ± 7 MPa for as-sprayed, 300 °C annealed, and 600 °C annealed conditions. However, these values were significantly lower than those for the N_2-sprayed coatings, which all failed in the glue at > 60 MPa (section 4.3). In addition, the He-sprayed coatings displayed lower tensile strength and elongation to failure than did N_2-sprayed coatings annealed in the same conditions, as shown in Figure 38. Those differences between coating tensile properties were analyzed through a fracture analysis (below).

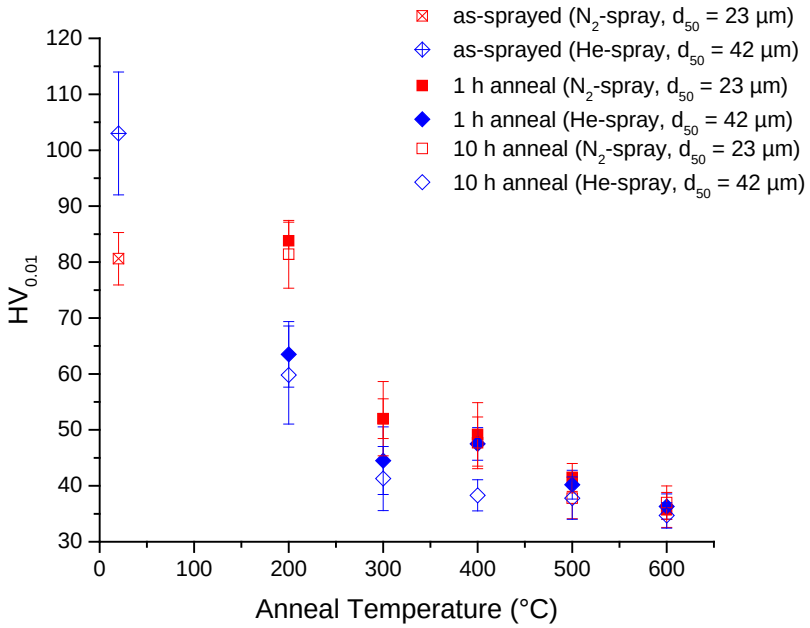


Figure 37: Microhardness as a function of anneal temperature for He-sprayed coatings (d_{50} = 23 µm powder for N_2-spray and d_{50} = 42 µm powder for He-spray).

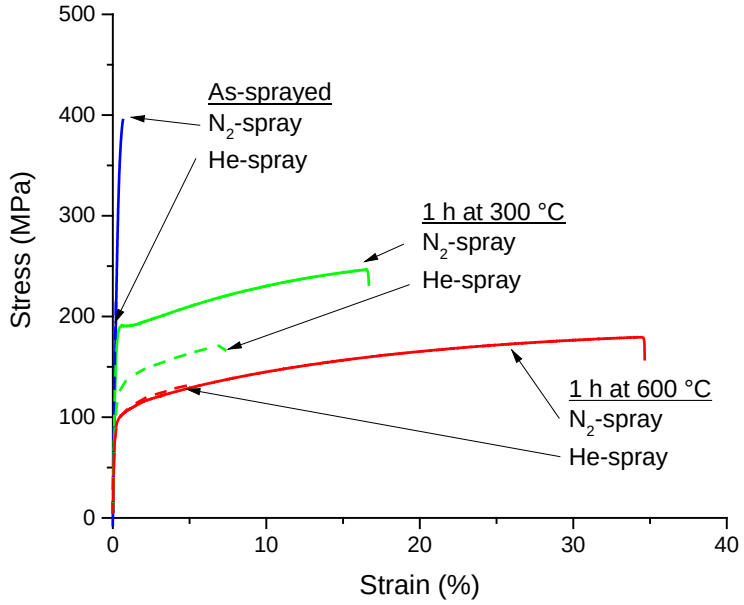


Figure 38: Representative stress-strain curves for He-sprayed and N_2-sprayed coatings (d_{50} = 23 µm powder for N_2-spray and d_{50} = 42 µm powder for He-spray).

Representative fracture surfaces of tensile specimens for coatings in the as-sprayed condition and after being annealed at 600 °C, shown in Figure 39, revealed that fractures appeared to occur along distinct layers in the He-sprayed coatings (c, d), which may have been a cause of low ductility. Due to the thickness and horizontal orientation of the layers, fracture in these coatings probably initiated and propagated along the interfaces between layers of material deposited in sequential passes. Although a definite cause of the weak bonding between layers deposited in different passes was not determined, observations of a color change is a possible indication that oxidation occurred between passes. Due to the 100 % particle deposition obtained with cold spray using helium gas, oxide layers may have become entrapped between the copper layers deposited with each pass; rather than being abraded away by powder on the periphery of the gas jet, a common occurrence during cold spray. For spray with nitrogen, this effect may have been mitigated if particles on the periphery of the gas jet stream produced less than 100 % deposition.

For He-sprayed coatings annealed at 600 °C, the high magnification image (Figure 39h) also displayed a dimpled fracture surface. However, particle boundaries were still observed in these coatings, indicating that fracture was a combination of failure at particle interfaces and within particles. Notably, this powder had only a moderate ductility increase to 6.3 ± 2.8 % strain at failure. However, the N_2-sprayed coating annealed at 600 °C was similar in appearance, indicating that relatively high ductility (27 ± 5 % strain at failure) may still be obtained with this type of fracture surface (i.e., combination of smooth and dimpled surfaces). Consequently, the lower ductility obtained for the He-sprayed coating compared to the N_2-sprayed coating was probably attributable to the additional particle debonding between layers deposited by different passes (i.e., distinct layers observed at low magnification in only the He-sprayed coating (a, c) and not the N_2-sprayed coating (e, g).

Overall, the comparison of N_2-sprayed and He-sprayed coatings produced in the general coating development (section 4) revealed that better mechanical properties coatings can be obtained when using higher gas temperature and pressure with N_2-spray (T_g = 800 °C and P_g = 5 MPa) compared to lower conditions with He-spray (T_g = 350 °C and P_g = 3.5 MPa).

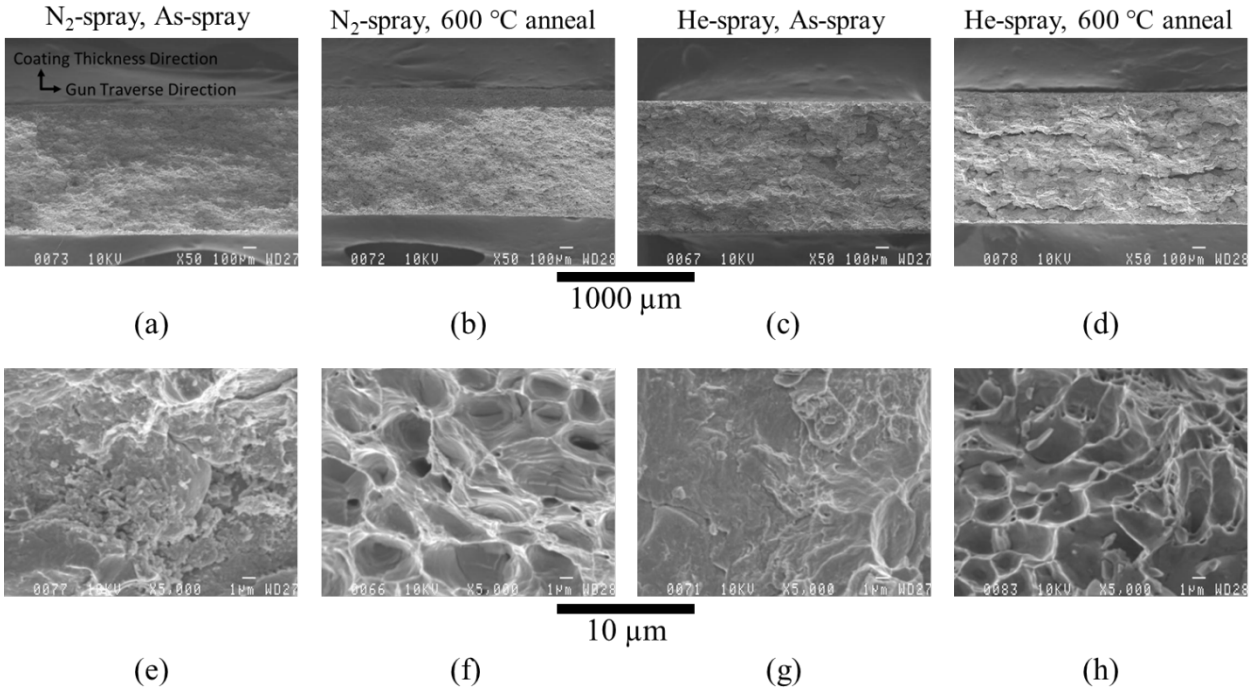


Figure 39: Representative fracture surfaces of tensile specimens for coatings: (a, e) N_2-sprayed, as-sprayed; (b, f) N_2-sprayed and annealed for 1 h at 600 °C; (c, g) He-sprayed, as-sprayed; (d, h) He-sprayed and annealed for 1 h at 600 °C;.

A.3.2 Mechanical Properties of N_2-Sprayed Coatings with Different Powders

The effect of powder on the mechanical properties of the resulting coating was evaluated using the N_2-sprayed coatings produced with d_{50} = 23 µm-powder (sections 4.3 and A1.1), with additional testing on N_2-sprayed coatings produced with the d_{50} = 42 µm powder. The spray conditions for the d_{50} = 42 µm powder are shown in Table 8 and mechanical testing results for coatings annealed for 1 h at 600 °C are shown in Table 19. The bond strength was slightly lower for the coatings with 42 µm powder (46 ± 8 MPa, instead of glue failure at 64 ± 5 MPa); however, results indicated that microhardness, tensile, and bend properties were similar for coatings made from each of the powders. Representative stress-strain curves are shown in Figure 40. Overall, the comparison of the two powders indicated that coatings with relatively similar mechanical properties can be produced with the two different powders, which was consistent with results from the powder selection testing phase (section3.2).

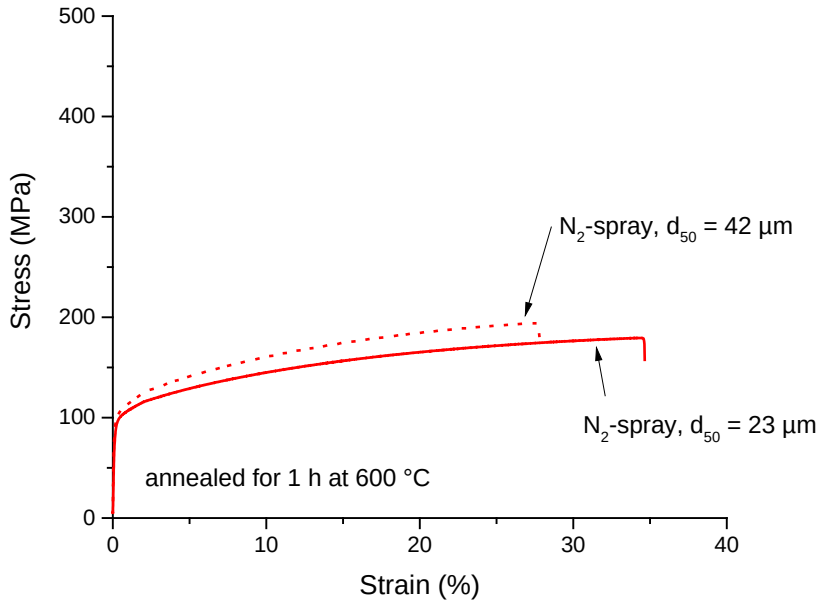


Figure 40: Representative stress-strain curves for N_2-sprayed coatings using d_{50} = 23 µm and d_{50} = 42 µm powders.

A.4 SAMPLE PRODUCTION FOR CORROSION TESTING

The preliminary coatings for corrosion scoping tests were produced on 12.7 X 15.25 X 0.64 cm mild steel plate substrate under the conditions detailed in Table 4 (for EBSD300) and Table 9 (for ADCS) in a helium recovery environment (i.e., containing <20% air atmosphere). The coated plate was sectioned into 51 disks (1.5 cm Ø) by EDM for subsequent testing and/or post-deposition processing, as shown in Figure 41. The production of subsequent corrosion samples (for exposure testing) involved the application of coatings using three different spray setups: outer diameter (OD) coating, top surface (TP1 and TP2) coating, and back face (BK1) coating. A summary of the spray conditions is shown in Table 4 and Table 9 (EBSD600 = TP1 and EBSD800 = TP2), while photos of the production method for the corrosion coating are shown in Figure 42. The OD coating was applied on three solid rod substrates [A36 steel, 9.5 mm Ø x 30.5 mm], as shown in Figure 41a. Each coated rod was then machined into five pieces with a 15.9 mm Ø (3.18 mm coating thickness) and 38.1 mm length, as shown in Figure 41b, for a total of 15 pieces. The top coating (test surface) was applied to the flat faces of OD-coated pieces using a rotating 15.25 cm Ø substrate holder, as shown in (c-f). The surfaces to be coated were degreased and grit blasted prior to spraying. After one face was coated, pieces were reversed in the substrate holder and the opposite faces were then coated. In order to prepare samples for the back face coating, both ends of the 15 pieces were then machined to produce 30 pieces with top and OD coatings on the specified 6.5 mm thick substrate, shown in (f). Back face coatings were applied to 29 of 30 pieces (1 piece with only top and OD coatings was delivered to NWMO) fixed into 3 flat substrate holders, shown in Figure 41g. Note that planar samples for accelerated corrosion testing were produced using the reference coating conditions on planar substrates described in section 5.1 (plates from R1 and R4 in Table 15).

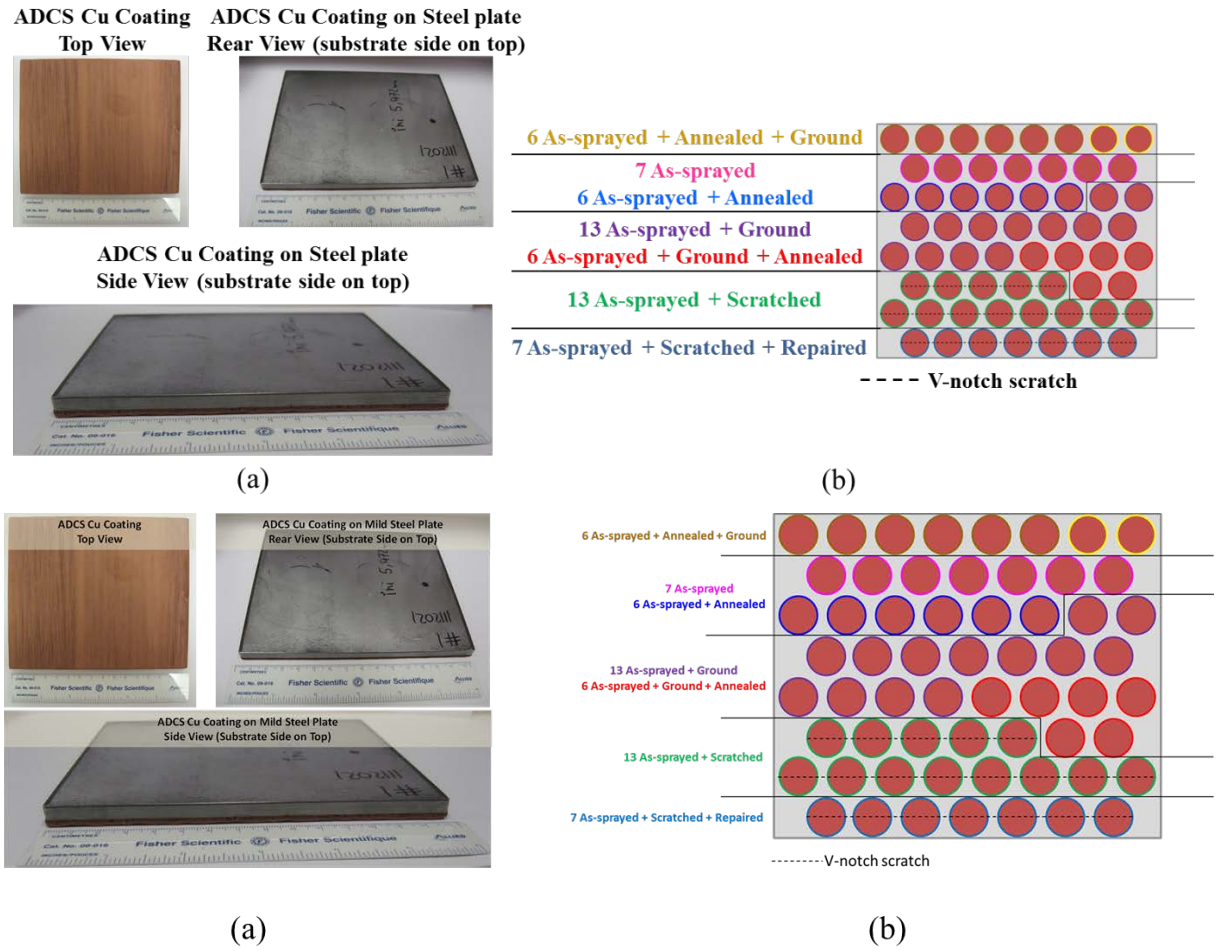


Figure 41: (a) Photograph of ADCS copper coating on mild steel plate for corrosion scoping testing and (b) scratch and sample pattern for testing.

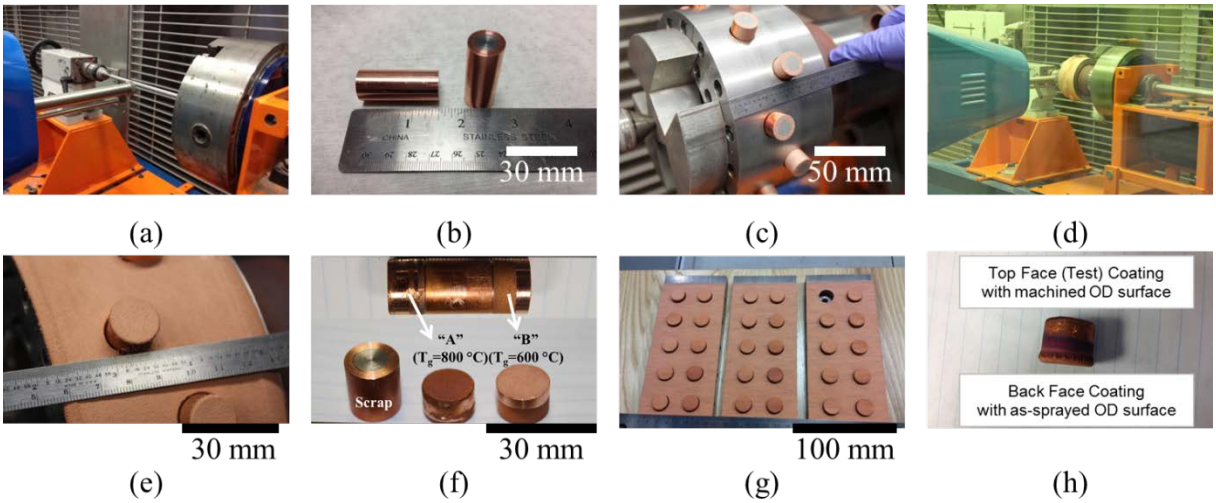


Figure 42: Photos of corrosion sample (exposure testing) production: (a) setup for OD coating, (b) OD coating pieces machined to 9.5 mm Ø x 38.1 mm length, (c) grit blasted pieces fixed into substrate holder, (d) top coating spray with rotating substrate holder and horizontally moving PCS-800 unit, (e) pieces after top coating applied, (f) top coating pieces with 6.4 mm thick substrate, (g) pieces in substrate holder with back face coatings applied, and (h) side view of corrosion sample.